Charmonium studies at forward rapidity with ALICE Muon Spectrometer at the LHC

By

Jhuma Ghosh

PHYS05201504005

Saha Institute of Nuclear Physics, Kolkata

A thesis submitted to the

Board of Studies in Physical Sciences

In partial fulfillment of requirements

For the Degree of

DOCTOR OF PHILOSOPHY

of

HOMI BHABHA NATIONAL INSTITUTE

November, 2020

Recommendations of the Viva Voce Committee

As members of the Viva Voce Committee, we certify that we have read the dissertation prepared by **Jhuma Ghosh** entitled **"Charmonuim studies at forward rapidity with ALICE Muon Spectrometer at the LHC"** and recommend that it may be accepted as fulfilling the dissertation requirement for the Degree of Doctor of Philosophy.

____ Date:

Chair - Prof. Pradip Roy

____ Date: 15/03/2021

Guide/Convener - Prof. Sukalyan Chattapadhyay

____ Date:

Member 1 - Prof. Subhasis Chattopadhyay

____ Date:

Member 2 - Prof. Supratik Majumdar

____ Date:

Member 2 - Prof. Debasis Das

Final approval and acceptance of this dissertation is contingent upon the candidate's submission of the final copies of the dissertation to HBNI.

I hereby certify that I have read this dissertation prepared under my direction and recommend that it may be accepted as fulfilling the dissertation requirement.

Date: 15/03/2021

Kolkata (Guide: Prof. Sukalyan Chattopadhyay)

STATEMENT BY AUTHOR

This dissertation has been submitted in partial fulfillment of requirements for an advanced degree at Homi Bhabha National Institute (HBNI) and is deposited in the Library to be made available to borrowers under rules of the HBNI.

Brief quotations from this dissertation are allowable without special permission, provided that accurate acknowledgement of source is made. Requests for permission for extended quotation from or reproduction of this manuscript in whole or in part may be granted by the Competent Authority of HBNI when in his or her judgment the proposed use of the material is in the interests of scholarship. In all other instances, however, permission must be obtained from the author.

Jhuma Ghosh.

Jhuma Ghosh

DECLARATION

I, hereby declare that the investigation presented in the thesis has been carried out by me. The work is original and has not been submitted earlier as a whole or in part for a degree / diploma at this or any other Institution / University.

Jhuma Ghosh.

Jhuma Ghosh

List of Publications arising from the thesis

Publications in Refereed Journal:

a. Published

1. "Measurement of nuclear effects on $\psi(2S)$ production in p–Pb collisions at $\sqrt{s_{NN}} = 8.16$ TeV"
   S. Acharya *et al.* [ALICE Collaboration], JHEP 07 (2020) 237
   [arXiv:2003.06053 [nucl-ex]].

2. "Studies of J/ψ production at forward rapidity in Pb–Pb collisions at $\sqrt{s_{\rm NN}}$ = 5.02 TeV"
   S. Acharya *et al.* [ALICE Collaboration], JHEP 02 (2020) 041
   [arXiv:1909.03158 [nucl-ex]]

b. Accepted

3. "Centrality dependence of J/ψ and $\psi(2S)$ production and nuclear modification in p–Pb collisions at $\sqrt{s_{NN}} = 8.16$ TeV", Accepted for publication in JHEP [arXiv:2008.04806 [nucl-ex]]

Conference Proceedings:

1. "Suppression of inclusive $\psi(2S)$ production in p-Pb collisions with ALICE at the LHC", Jhuma Ghosh for the ALICE Collaboration, DAE Symposium on Nuclear Physics, Vol 62 (2017), p. 806.

2. “Recent quarkonium measurements in small systems with the ALICE detector at the LHC”, Jhuma Ghosh on behalf of the ALICE collaboration, XXVIIIth International Conference on Ultrarelativistic Nucleus-Nucleus Collisions (Quark Matter 2019), accepted in Nuclear Physics A (article id: 121794).

ALICE Analysis Notes:

1. “Inclusive ψ(2S) production in pp collisions at $\sqrt{s} = 5.02$ TeV”, Jhuma Ghosh, Sukalyan Chattopadhyay, Indranil Das.
   https://alice-notes.web.cern.ch/node/941

2. “Inclusive ψ(2S) production in p-Pb collisions at $\sqrt{s_{NN}} = 8.16$ TeV”, Jhuma Ghosh, Luca Micheletti, Sukalyan Chattopadhyay, Roberta Arnaldi, Indranil Das.
   https://alice-notes.web.cern.ch/node/677

3. “Centrality dependence of the inclusive ψ(2S) production in p–Pb collisions at $\sqrt{s_{NN}} = 8.16$ TeV”, Jhuma Ghosh, Luca Micheletti, Sukalyan Chattopadhyay and Indranil Das.
   https://alice-notes.web.cern.ch/node/723

4. “Differential studies of J/ψ production as a function of rapidity in Pb–Pb collisions at $\sqrt{s_{NN}} = 5.02$ TeV”, Hushnud Hushnud, Jhuma Ghosh, Indranil Das and Sukalyan Chattopadhyay.
   https://alice-notes.web.cern.ch/node/721

5. “Suppression of inclusive ψ(2S) production in Pb–Pb collisions at $\sqrt{s_{\rm NN}} = 5.02$ TeV (2015+2018 data)”, Biswarup Paul, Jhuma Ghosh, Hushnud Hushnud, Kunal Garg, Indranil Das and Sukalyan Chattopadhyay. https://alice-notes.web.cern.ch/node/1088

ALICE Public Notes:

1. “Reference pp cross sections for J/ψ and ψ(2S) studies as a function of centrality in p–Pb collisions at $\sqrt{s_{NN}} = 8.16$ TeV”, ALICE-PUBLIC-2020-007, https://cds.cern.ch/record/2740858

Charmonium studies at forward rapidity with ALICE Muon Spectrometer at the LHC

By

Jhuma Ghosh

PHYS05201504005

Saha Institute of Nuclear Physics, Kolkata

A thesis submitted to the

Board of Studies in Physical Sciences

In partial fulfillment of requirements

For the Degree of

DOCTOR OF PHILOSOPHY

of

HOMI BHABHA NATIONAL INSTITUTE

November, 2020

Recommendations of the Viva Voce Committee

As members of the Viva Voce Committee, we certify that we have read the dissertation prepared by **Jhuma Ghosh** entitled **"Charmonuim studies at forward rapidity with ALICE Muon Spectrometer at the LHC"** and recommend that it may be accepted as fulfilling the dissertation requirement for the Degree of Doctor of Philosophy.

______________________________________ Date:

Chair - Prof. Pradip Roy

______________________________________ Date: 15/03/2021

Guide/Convener - Prof. Sukalyan Chattapadhyay

______________________________________ Date:

Member 1 - Prof. Subhasis Chattopadhyay

______________________________________ Date:

Member 2 - Prof. Supratik Majumdar

______________________________________ Date:

Member 2 - Prof. Debasis Das

Final approval and acceptance of this dissertation is contingent upon the candidate's submission of the final copies of the dissertation to HBNI.

I hereby certify that I have read this dissertation prepared under my direction and recommend that it may be accepted as fulfilling the dissertation requirement.

Date: 15/03/2021

Kolkata (Guide: Prof. Sukalyan Chattopadhyay)

STATEMENT BY AUTHOR

This dissertation has been submitted in partial fulfillment of requirements for an advanced degree at Homi Bhabha National Institute (HBNI) and is deposited in the Library to be made available to borrowers under rules of the HBNI.

Brief quotations from this dissertation are allowable without special permission, provided that accurate acknowledgement of source is made. Requests for permission for extended quotation from or reproduction of this manuscript in whole or in part may be granted by the Competent Authority of HBNI when in his or her judgment the proposed use of the material is in the interests of scholarship. In all other instances, however, permission must be obtained from the author.

Jhuma Ghosh.

Jhuma Ghosh

DECLARATION

I, hereby declare that the investigation presented in the thesis has been carried out by me. The work is original and has not been submitted earlier as a whole or in part for a degree / diploma at this or any other Institution / University.

Jhuma Ghosh.

Jhuma Ghosh

Contents

List of Figures

List of Tables

CHAPTER 7

Summary and Outlook

Summary

This chapter briefly summarizes the results presented in this thesis. The data, collected by the ALICE Muon spectrometer, in pp, p–Pb and Pb–Pb collisions have been analyzed and studied. The pp results have been used to normalize the p–Pb and Pb–Pb results. The results from p–Pb and Pb–Pb data presented in the thesis, help to extend our understanding of the cold and hot nuclear matter effects on the charmonia.

ψ(2S) production in pp collisions

The results have been presented in two parts. Firstly, the cross section of ψ(2S) production as a function of p_{T} and rapidity in pp collisions at 5.02 TeV have been reported. These results are crucial for understanding the QCD processes and production of the charmonia. The first measurement of p_{T} and y differential cross sections at 5.02 TeV, are shown. Secondly the production cross section ratio of ψ(2S) and J/ψ, has been studied to explore the energy dependence. Comparing

with the published ALICE results at 7, 8 and 13 TeV, it is established that this ratio does not show any significant energy dependence.

The inclusive $\psi(2S)$ production cross section, integrated over $0 < p_{\rm T} < 12$ GeV/c and for $2.5 < y < 4$, has been found to be $\sigma_{\psi(2S)} = 0.86 \pm 0.06$ (stat.) $\pm$ 0.10 (syst.) μb. The cross section of $\psi(2S)$ is described well by the NRQCD calculations except for higher $p_{\rm T}$ bins. The NLO calculation based ICEM model, on the other hand overestimates the data at high $p_{\rm T}$.

The ratio of inclusive $\psi(2S)$-to-J/ψ production cross sections integrated over $p_{\rm T}$ and y is found to be 0.15 ± 0.01 (stat.) ± 0.02 (syst.). The calculations based on NRQCD+CGC well reproduce the ratio as a function of $p_{\rm T}$ and y for $p_{\rm T} < 8$ GeV/c. The trend of the $\psi(2S)$ over J/ψ cross-section ratio as a function of $p_{\rm T}$ and y is overestimated by the CEM model in the low $p_{\rm T}$ region.

$\psi(2S)$ production in p–Pb collisions

The results on the inclusive $\psi(2S)$ production at the forward (p-going direction, $2.03 < y_{cms} < 3.53$) and backward (Pb-going direction, $-4.46 < y_{cms} < -2.96$) rapidities in p–Pb collisions at 8.16 TeV, have been presented in chapter 5 of the thesis in the form of production cross sections, the double cross-section ratios with respect to the J/ψ in p–Pb and pp, and the nuclear modification factors $R_{\rm pPb}$. The analysis has been segmented in two parts: 1) $p_{\rm T}$ and y differential cross-section measurement and 2) centrality dependence measurement.

The main conclusion which has been drawn from the above observables is that the initial state effects, which are sufficient to explain J/ψ suppression behavior, cannot describe the $\psi(2S)$ suppression at the backward rapidity where it is found to be significantly suppressed. The final state effects are needed to describe $\psi(2S)$ suppression.

Apart from that, no significant energy dependence or p_{T} dependence is observed in R_{pPb}.

J/ψ and ψ(2S) production in Pb–Pb collisions

The multi-differential J/ψ and single-differential ψ(2S) cross-section measurements are described in chapter 6.

The analysis of J/ψ in Pb–Pb collisions at 5.02 TeV at forward rapidity has been performed to investigate the recombination scenario in heavy-ion collisions. The high statistics of 2015+2018 datasets made it possible to precisely show the effect of recombination which are visible only at low p_{T} in the most central collisions. This effect induces a slope in the R_{AA} vs y plot in that particular bins, confirming the role of in-medium recombination of $c\bar{c}$ pairs.

In the next section, the measurement of R_{AA} of ψ(2S) as a function of p_{T} and centrality, has been presented. The ψ(2S) has been found to be more suppressed compared to J/ψ in semi-central and central collisions.

Outlook

ALICE is preparing for a major upgrade for Run 3 and Run 4 to operate in high luminosity beams.

The introduction of Muon Forward Tracker (MFT) will give the opportunity to study the prompt J/ψ production by separating the contribution to J/ψ cross-section coming from B decay. This has not been possible till date because of the presence of the absorber, which does not allow the displaced vertex analysis. It will be interesting to look at the J/ψ results in different collision systems in the upcoming days and estimate the B-meson production cross-sections at forward rapidities through J/ψ

tagging.

The charged particle multiplicity dependence of J/ψ cross-section in pp collisions, has gained a lot of attentions in the past due to the direct evidence of MultiPartonic Interactions (MPI). A similar study on ψ(2S) will shed light on the role of MPI in ψ(2S) production in pp collisions.

The search for deconfinement in small systems is currently a hot and most debated topic. A reasonable study of charmonium and in particular bottomonium suppression in small systems will require much higher statistics than the present pp data at 13 TeV. Such high statistics is likely to be possible during the high luminosity periods of Run 3 and 4. If such suppression is observed, then present understanding of QGP will be challenged.

The ψ(2S) production as a function of rapidity in p–Pb collisions at $\sqrt{s_{\mathrm{NN}}} = 8.16$ TeV exhibits a slope towards the forward rapidity in contrary to the model predictions and J/ψ observation of flat dependence. The large uncertainties however does not allow any firm conclusion. This regions should be explored in future with higher precision and in more rapidity bins. It may reveal some unknown features of the ψ(2S) production in p–Pb collisions.

The J/ψ flow coefficient v_2 measurement at 20-40% centrality in Pb–Pb collisions at $\sqrt{s_{\mathrm{NN}}} = 5.02$ TeV is still not explained by the theory. The installation of MFT will help to improve the results in the high p_{T} bins for prompt J/ψ. Not only v_2, but higher harmonics like v_3, v_4 will also be interesting observables the Run 3 and 4.

The measurement of ψ(2S) production is more challenging than that of J/ψ, because of a smaller production cross section and even larger suppression in PbPb, giving rise to a very low signal-to-background ratio. Therefore, we expect improvement in the uncertainties in ψ(2S) results in Run 3.

At present, all the states of upsilon(nS) cannot be resolved fully. Better mass reso-

lution of all the resonance states will ensure precision in the results.

We look forward towards Pb–Pb run at the highest achievable energy $\sqrt{s_{\mathrm{NN}}} = 5.5$ TeV. For all those interesting results from ALICE in the upcoming days, we need to wait till 2022.

CHAPTER 7

Summary and Outlook

Summary

This chapter briefly summarizes the results presented in this thesis. The data, collected by the ALICE Muon spectrometer, in pp, p–Pb and Pb–Pb collisions have been analyzed and studied. The pp results have been used to normalize the p–Pb and Pb–Pb results. The results from p–Pb and Pb–Pb data presented in the thesis, help to extend our understanding of the cold and hot nuclear matter effects on the charmonia.

ψ(2S) production in pp collisions

The results have been presented in two parts. Firstly, the cross section of ψ(2S) production as a function of p_{T} and rapidity in pp collisions at 5.02 TeV have been reported. These results are crucial for understanding the QCD processes and production of the charmonia. The first measurement of p_{T} and y differential cross sections at 5.02 TeV, are shown. Secondly the production cross section ratio of ψ(2S) and J/ψ, has been studied to explore the energy dependence. Comparing

with the published ALICE results at 7, 8 and 13 TeV, it is established that this ratio does not show any significant energy dependence.

The inclusive $\psi(2S)$ production cross section, integrated over $0 < p_{T} < 12$ GeV/c and for $2.5 < y < 4$, has been found to be $\sigma_{\psi(2S)} = 0.86 \pm 0.06$ (stat.) $\pm$ 0.10 (syst.) μb. The cross section of $\psi(2S)$ is described well by the NRQCD calculations except for higher p_{T} bins. The NLO calculation based ICEM model, on the other hand overestimates the data at high p_{T}.

The ratio of inclusive $\psi(2S)$-to-J/ψ production cross sections integrated over p_{T} and y is found to be 0.15 ± 0.01 (stat.) ± 0.02 (syst.). The calculations based on NRQCD+CGC well reproduce the ratio as a function of p_{T} and y for $p_{T} < 8$ GeV/c. The trend of the $\psi(2S)$ over J/ψ cross-section ratio as a function of p_{T} and y is overestimated by the CEM model in the low p_{T} region.

$\psi(2S)$ production in p–Pb collisions

The results on the inclusive $\psi(2S)$ production at the forward (p-going direction, $2.03 < y_{cms} < 3.53$) and backward (Pb-going direction, $-4.46 < y_{cms} < -2.96$) rapidities in p–Pb collisions at 8.16 TeV, have been presented in chapter 5 of the thesis in the form of production cross sections, the double cross-section ratios with respect to the J/ψ in p–Pb and pp, and the nuclear modification factors R_{pPb}. The analysis has been segmented in two parts: 1) p_{T} and y differential cross-section measurement and 2) centrality dependence measurement.

The main conclusion which has been drawn from the above observables is that the initial state effects, which are sufficient to explain J/ψ suppression behavior, cannot describe the $\psi(2S)$ suppression at the backward rapidity where it is found to be significantly suppressed. The final state effects are needed to describe $\psi(2S)$ suppression.

Apart from that, no significant energy dependence or p_{T} dependence is observed in R_{pPb}.

J/ψ and ψ(2S) production in Pb–Pb collisions

The multi-differential J/ψ and single-differential ψ(2S) cross-section measurements are described in chapter 6.

The analysis of J/ψ in Pb–Pb collisions at 5.02 TeV at forward rapidity has been performed to investigate the recombination scenario in heavy-ion collisions. The high statistics of 2015+2018 datasets made it possible to precisely show the effect of recombination which are visible only at low p_{T} in the most central collisions. This effect induces a slope in the R_{AA} vs y plot in that particular bins, confirming the role of in-medium recombination of $c\bar{c}$ pairs.

In the next section, the measurement of R_{AA} of ψ(2S) as a function of p_{T} and centrality, has been presented. The ψ(2S) has been found to be more suppressed compared to J/ψ in semi-central and central collisions.

Outlook

ALICE is preparing for a major upgrade for Run 3 and Run 4 to operate in high luminosity beams.

The introduction of Muon Forward Tracker (MFT) will give the opportunity to study the prompt J/ψ production by separating the contribution to J/ψ cross-section coming from B decay. This has not been possible till date because of the presence of the absorber, which does not allow the displaced vertex analysis. It will be interesting to look at the J/ψ results in different collision systems in the upcoming days and estimate the B-meson production cross-sections at forward rapidities through J/ψ

tagging.

The charged particle multiplicity dependence of J/ψ cross-section in pp collisions, has gained a lot of attentions in the past due to the direct evidence of MultiPartonic Interactions (MPI). A similar study on ψ(2S) will shed light on the role of MPI in ψ(2S) production in pp collisions.

The search for deconfinement in small systems is currently a hot and most debated topic. A reasonable study of charmonium and in particular bottomonium suppression in small systems will require much higher statistics than the present pp data at 13 TeV. Such high statistics is likely to be possible during the high luminosity periods of Run 3 and 4. If such suppression is observed, then present understanding of QGP will be challenged.

The ψ(2S) production as a function of rapidity in p–Pb collisions at $\sqrt{s_{\mathrm{NN}}} = 8.16$ TeV exhibits a slope towards the forward rapidity in contrary to the model predictions and J/ψ observation of flat dependence. The large uncertainties however does not allow any firm conclusion. This regions should be explored in future with higher precision and in more rapidity bins. It may reveal some unknown features of the ψ(2S) production in p–Pb collisions.

The J/ψ flow coefficient v_2 measurement at 20-40% centrality in Pb–Pb collisions at $\sqrt{s_{\mathrm{NN}}} = 5.02$ TeV is still not explained by the theory. The installation of MFT will help to improve the results in the high p_{T} bins for prompt J/ψ. Not only v_2, but higher harmonics like v_3, v_4 will also be interesting observables the Run 3 and 4.

The measurement of ψ(2S) production is more challenging than that of J/ψ, because of a smaller production cross section and even larger suppression in PbPb, giving rise to a very low signal-to-background ratio. Therefore, we expect improvement in the uncertainties in ψ(2S) results in Run 3.

At present, all the states of upsilon(nS) cannot be resolved fully. Better mass reso-

lution of all the resonance states will ensure precision in the results.

We look forward towards Pb–Pb run at the highest achievable energy $\sqrt{s_{\mathrm{NN}}} = 5.5$ TeV. For all those interesting results from ALICE in the upcoming days, we need to wait till 2022.

CHAPTER 1

Introduction

The story of 'charmonium suppression' started around thirty five years ago, with the results from NA38 experiment at CERN SPS. The term 'suppression' was first proposed by NA38 collaboration in 1996 [1], where they found the nuclear matter effect. This paper showed that the centrality dependence of ψ(2S) over J/ψ ratio got diminished in Pb–Pb collisions from S+U. We know that the local energy density increases in Pb–Pb collisions. So this observation demanded a theory which would explain a similar centrality dependence of both the resonances at high energy density. Clearly this observation drew attention of the scientists and another publication came out in 2000 by NA50 collaboration [2]. This paper reported the abnormal enhancement of open charm production in nucleus-nucleus collisions and its increase with centrality. Till then no single theory was able to describe all the charmonium results of NA38 and NA50 experiments simultaneously and the surprise continued.

The next result that physicists were waiting for was on J/ψ production in Pb–Pb collisions, which was published in 2001 ([3]). It showed step-wise J/ψ suppression pattern with no saturation for the most central collisions. The models of J/ψ suppression based on the absorption of the meson by interactions with the surrounding hadronic matter failed to explain the steepness of the slope (departure from the ordinary nuclear absorption scenario). It can be concluded that the J/ψ suppression pattern observed in the NA50 data provided significant evidence for deconfinement of quarks and gluons in Pb–Pb collisions. It became necessary to extend the study for other charmonium states in systems other than Pb–Pb collisions.

In 2004 [4], the dependence of the nuclear absorption, on the nucleus size had been studied by means of studying J/ψ and ψ(2S) production cross-sections for p-A systems. Comparing the two results, the nuclear absorption was found to be stronger for the ψ(2S) than for the J/ψ. The study of the p–A system grabbed the attention for two reasons: it helps (a) to build an idea on how the heavy quarkonia are produced, testing the Non-Relativistic Quantum ChromoDynamics (NRQCD), Color Evaporation Model (CEM), Color Singlet (CS) approaches; (b) to properly interpret the suppression pattern in AA collisions, the determination of nuclear absorption in p–A collisions became crucial. It was found that ψ(2S) was strongly suppressed at the most negative Feynman variable x_{F} bin. Qualitatively this observation was compatible with the fact that ψ(2S) had a lower breakup threshold [5].

The next important results came after a gap of three years. Till then the formation of a bound state by means of the evolution of a $c\bar{c}$ pair originated from gluon fusion at early stages of collision, was not described by the existing theories. So, it became crucial to test the theoretical models tuned for Pb-Pb collisions, on different collision systems. In 2007 NA60 experiment published the results on J/ψ suppression in centrality bins for In-In collisions. The anomalous J/ψ suppression was found towards more central events. The J/ψ suppression results in Au-Au collisions from PHENIX also became available. The new results from NA60, most accurate at that time, took the challenge one step ahead for the theoreticians. The theoretical calculations failed to quantitatively reproduce the J/ψ suppression pattern observed in In-In collisions. Thus, SPS and RHIC experiments created the path on which ALICE started its journey.

ALICE at the LHC, made it possible to probe low p_{T} region, thereby reaching small values of Bjorken-x ($x < 10^{-5}$) and corresponding squared momentum transfer Q^2 ($= m^2_{\mathrm{J}/\psi}$). The observation [13] showed that central value given by FONLL, underestimated the p_{T} differential open charm cross sections. The results on the dependence of charm production cross sections on the collision energy at central rapidity, established a good match with the pQCD predictions [14].

During the year 2012, the first ALICE result on heavy-flavour decay muons in heavy ion collisions got published. As mentioned earlier the heavy quarks are sensitive to the presence of deconfined phase of matter, the QGP. At LHC the initial energy density is so high that it creates perfect environment for abundant heavy quark production. Thus this publication played a crucial role in searching for the QGP in heavy-ion collisions. It reported that the muons from heavy flavors decay showed strong suppression, which increased with centrality.

The first study of inclusive J/ψ production in Pb–Pb collisions at $\sqrt{s_{\mathrm{NN}}} = 2.76$ TeV at forward rapidity [21] showed higher nuclear modification factor (R_{AA}) values in central collision compared to what was observed at PHENIX. This could be a hint of recombination of unpaired charm quark and anti-quark pair giving rise to low-p_{T} J/ψ. For this reason a centrality and p_{T} dependent study was carried out [22], which supported the theory of recombination in the deconfined partonic medium. As the charm density in the medium increases with the increase of collision energy, the probability of recombination also increases. This observation opened a new domain of study, which has been pursued in more details in this thesis.

The following year, the first p–Pb results at $\sqrt{s_{\mathrm{NN}}} = 5.02$ TeV were published [15] which was needed to calibrate and disentangle the initial/final state effects present in the heavy-ion collisions. The previously available results from Tevatron [16], HERA [17], SPS [18, 19] and RHIC [20], highlighted a suppression of J/ψ yield with increase of Feynman-x ($x_{\mathrm{F}} = 2p_{\mathrm{L}}/\sqrt{s}$, p_{L} being the longitudinal momentum). Also the suppression tended to increase with $\sqrt{s}$ for fixed x_{F} and the existing theoretical models could not provide a quantitative explanation. At this stage, the p–Pb results at the LHC, became very important as the data allowed the access to Bjorken-$x \backsim 10^{-5}$, which was unexplored before. Besides, it was also crucial for interpretation of the Pb–Pb results. This paper reported that there is no strong variation of the nuclear modification factors, especially at backward rapidity. This observation contradicted with the theoretical model calculations (including coherent energy loss), which suggested a steeper dependence on rapidity.

This interesting findings demanded similar study for weakly bound ψ(2S). The first inclusive ψ(2S) measurement in p–Pb collisions at $\sqrt{s_{\mathrm{NN}}} = 5.02$ TeV at forward rapidity [23] showed a larger suppression of ψ(2S) compared to that of J/ψ at both the rapidity ranges. The final state effects, like interaction with cold nuclear matter was employed to explain this behavior. But there is an inconsistency, as in the forward rapidity, the crossing time of the quark pair is less. Thus it does not get enough time for interaction with the cold nuclear matter. No p_{T} dependence was reported due to inadequate statistics.

The results presented in this thesis extends our knowledge on the phenomenon of 'charmonium suppression'.

Bibliography

[1] M.C. Abreu et al. (NA50 Coll.), Nuclear Physics A610 (1996) 404c-417c.

[2] M.C. Abreu et al. (NA50 Coll.), Eur. Phys. J. C 14, 443455 (2000).

[3] Francesco Prino (NA50 Coll.), arXiv:hep-ex/0101052v1.

[4] B. Alessandro et al. (NA50 Coll.), Eur. Phys. J. C 33, 3140 (2004).

[5] D. Kharzeev and H. Satz, Phys. Lett. B 356, 365 (1995).

[6] D. Acosta et al. [CDF Coll.], Phys. Rev. Lett. 91 (2003) 241804.

[7] B.A. Kniehl et al., Phys. Rev. Lett. 96 (2006) 012001.

[8] A. Adare et al. [PHENIX Coll.], Phys. Rev. Lett. 97 (2006) 252002.

[9] B.I. Abelev et al. [STAR Coll.], Phys. Rev. Lett. 98 (2007) 192301; W. Xie et al. [STAR Coll.], PoS(DIS2010)182 (2010).

[10] D. Acosta et al. [CDF Coll.], Phys. Rev. D71 (2005) 032001.

[11] M. Cacciari et al., JHEP 0407 (2004) 033.

[12] B.A. Kniehl et al., Phys. Rev. D77 (2008) 014011.

[13] B. Abelev et al. [ALICE Coll.], JHEP 01 (2012) 128.

[14] B. Abelev et al. [ALICE Coll.], JHEP 1207 (2012) 191.

[15] B. Abelev et al. [ALICE Coll.], JHEP 02 (2014) 073.

[16] M.J. Leitch et al. (E866 Collaboration), Phys. Rev. Lett. 84(2000) 3256.

[17] I. Abt et al. (HERA-B Collaboration), Eur. Phys. J. C 60(2009) 525.

[18] B. Alessandro et al. (NA50 Collaboration), Eur. Phys. J. C48(2006) 329.

[19] R. Arnaldi et al. (NA60 Collaboration), Phys. Lett. B706 (2012) 263.

[20] A. Adare et al. (PHENIX Collaboration), Phys. Rev. C 87(2013) 034904.

[21] B. Abelev et al. [ALICE Coll.], Phys. Rev. Lett. 109 (2012) 112301.

[22] B. Abelev et al. [ALICE Coll.], Phys. Lett. B734 (2014).

[23] B. Abelev et al. [ALICE Coll.], JHEP 12 (2014) 073.

CHAPTER 2

Theory

The quarkonia (bound state of quark-antiquark pairs like $c\bar{c}$, $b\bar{b}$) decay electromagnetically to opposite sign lepton pairs of definite mass. Although quarkonium cannot be detected directly, it is easy to locate the peak around its mass in the dilepton invariant mass continuum. For this reason, it can be used as a probe to investigate the matter produced relativistic collisions. Even after 46 years of discovery of J/ψ by Brookhaven National Laboratory [1] and Stanford Linear Accelerator Center [2], it is guiding us to find the secret of the universe. But how did it start? It was not before 1986, when Matsui and Satz [3] predicted suppression of charmonium in the deconfined medium by means of color screening. The suppression was quantified using the reference of nucleon-nucleon collisions. The suppression confirms that a part of the produced quarkonia is depleted in the medium produced in the heavy-ion collisions.

Standard Model of elementary particles

The biography of particles known as the Standard Model, has successfully accommodated all the particles interacting via electromagnetic, strong and weak forces.

The 21^{st} century Standard Model has traveled through many roads, beginning with unification of electromagnetic and weak forces in 1960s to the present day structure. Its framework is guided by the gauge symmetry of the $\mathrm{SU}(3)_C\mathrm{x}\mathrm{SU}(2)_L\mathrm{x}\mathrm{U}(1)_Y$ group. $\mathrm{SU}(3)_C$ belongs to the symmetry group of strong interaction, while $\mathrm{SU}(2)_L$ and $\mathrm{U}(1)_Y$ corresponds to the weak and electromagnetic interactions respectively. Fig. 2.1 summarises the basic constituents of the Standard Model. Based on the spin, the elementary particles are categorized into two classes: fermions for the particles with fractional spin and bosons as particles with integer spin numbers.

The fermions are further classified into three generations of quarks and leptons following a mass hierarchy from lower to higher. The leptons participate in electromagnetic and weak interaction, but not strong interaction. The most stable charged lepton is electron, differing in mass and finite lifetime from other leptons such as muon, taon. The charged leptons have their neutral partner called neutrino and each of them has their anti particle with the same property but different quantum number. The gluons, quanta of the strong field, are massless. The challenge for experimental investigation of quarks is that they do not exist as isolated. The most elementary quark systems that are found include baryons (made of three quarks) and mesons (made of a quark and an antiquark). But there are also exotic hadrons made of more than three quarks. In 2003, Belle collaboration claimed the discovery

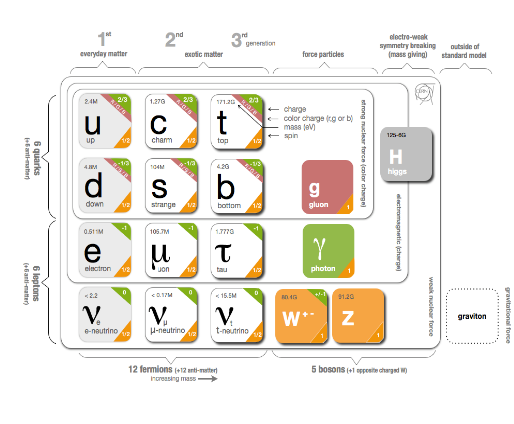

Figure 2.1: The constituents of Standard Model at a glance [4]

of a tetraquark state X(3872) [5]. In 2015, LHCb collaboration at CERN claimed to have found an exotic structures which they referred as pentaquark-charmonium states [6]. Later in 2019, LHCb confirmed discovery of narrow pentaquark states $P_c(4312)^+$ and $P_c(4450)^+$ [7]. Recently LHCb collaboration has reported to observe an exotic particle made up of four charm quarks X(6900) [8]. W^{+-} and Z bosons act as the mediator in weak interactions in the same way as photons play the role for electromagnetic interactions. The electromagnetic and the weak interaction are unified in the standard model through electroweak symmetry [9–11].

One cannot write a mass term for the particles in the standard model, respecting both the Lorentz and gauge symmetries, unless there is a mechanism known as Higgs mechanism. The $SU(2)_L x U(1)_Y$ symmetry is spontaneously broken into $U(1)_{EM}$ in the Higgs mechanism and as a result of it, the three gauge bosons W+- and Z get masses from the gauge invariant kinetic terms of the Higgs field and the fermions (namely quarks and charged leptons) get masses from the Yukawa term. About forty years after the prediction of Higgs mechanism, CMS and ATLAS collaboration at CERN discovered the Higgs boson [12, 13].

Quantum ChromoDynamics (QCD)

In the late sixties, it was believed that the perturbation method in Quantum field theory cannot be applied to describe strong interaction of colored quarks and gluons, even if it was proved to be successful in explaining the Quantum ElectroDynamics. So, a new formulation independent of the perturbative approach evolved, which is known as Quantum ChromoDynamics (QCD). The mathematical foundation derives from the $SU(3)_c$ gauge symmetry. The essential properties of this theory are:

- Quarks carry both the electric and color charges, which are red, green and blue and their anticolors.

- Exchange of color is mediated via eight bicolored gluons which can interact among themselves too.
- The interaction strength is described in terms of the strong coupling constant α_s.

The two important features of QCD are asymptotic freedom and chiral symmetry breaking.

Asymptotic freedom

As a result of quantum fluctuations, the vacuum is viewed as a polarising medium. It means when a quark propagates it emits gluons, which can further annihilate into quark-antiquark pairs. Thus a test charge will see a quark surrounded by a cloud of color charges. This is called the color screening effect. But unlike QED, strong interaction has an additional feature which makes the behavior of the force different. As the colored gluons can interact with other gluons (non-abelian interaction), the force increases with increase of the distance from the quark. This kind of vacuum polarisation gives rise to the anti-screening effect, which is stronger than screening effect (Fig.2.2).

As shown in Fig.2.3, the coupling constant α_s decreases when the inter-partonic distance is small (high energy limit). In this situation, the quark behaves as quasi-free. This is called asymptotic freedom. Conversely, at large distances the α_s value increases, which leads to the confinement of quarks into color neutral states.

Chiral symmetry breaking

QCD lagrangian exhibit chiral symmetry for zero quark mass ($m_q \approx 0$), i.e. the lagrangian is invariant when the left handed and right handed parts are rotated independently. In that case, the interactions between quarks with different chiralities are absent. This symmetry is expressed in terms of chiral condensate written as:

$\langle\bar{\psi}\psi\rangle = \langle\bar{\psi_L}\psi_R + \bar{\psi_R}\psi_L\rangle \neq 0$, where ψ_L and ψ_R are left and right hand quark fields respectively. During spontaneous symmetry breaking, the Higgs field gets a vev (as the potential has nonzero minima, as shown in right panel of Fig.2.4), resulting in mass terms of all the particles including quarks. This in turns breaks the chiral symmetry. However at high energy limit, the Higgs potential has its minima at 0, as shown in left panel of Fig.2.4, hence the chiral symmetry is restored. This phenomena is a signature of QCD phase transition.

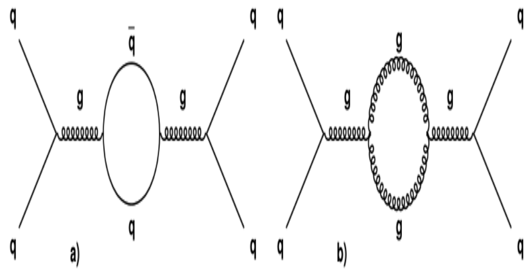

Figure 2.2: Vacuum polarisation in QCD: a)screening and b)anti-screening effect [14].

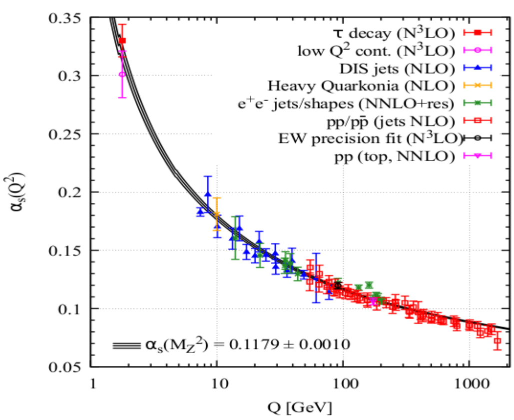

Figure 2.3: The variation of α_s with the energy scale Q [15].

QCD phase diagram and Quark-Gluon Plasma(QGP)

Fig. 2.5 illustrates the phase diagram of QCD, as a function of net baryon density (μ_B) and temperature. At low temperature and low baryon density, i.e. at the left bottom region of the plot, quarks are confined to make hadrons. Moving towards the right of the plot, i.e. at high density and low temperature, a degenerate gas of neutrons are formed, which exists in the neutron star. The interior of the neutron star is believed to be made of dense neutron rich matter due to strong gravitational pull. The Neutron star Interior Composition Explorer (NICER) is aiming to in-

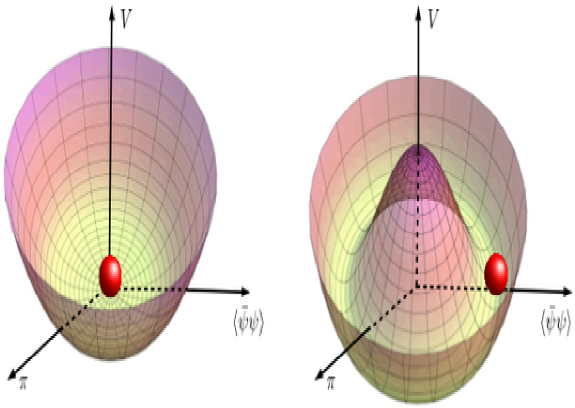

Figure 2.4: A pictorial representation of the chiral symmetry breaking scenario [17].

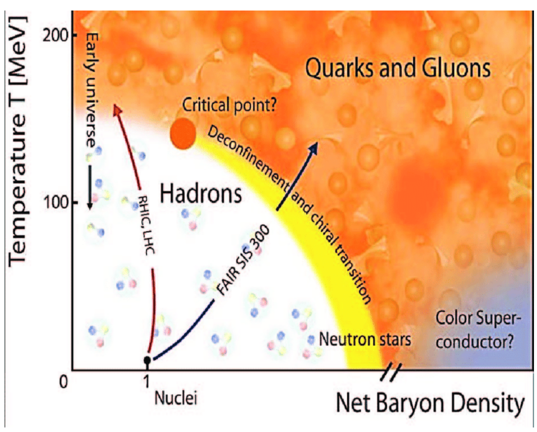

Figure 2.5: A pictorial representation of the phase diagram of QCD [18].

vestigate further about the neutron star especially the massive one with a mass of 2.4 times the solar mass. Although the equation of state of the interior matter is not yet known, but the relations between the mass and radii suggest the following possibilities- i) individual neutrons dissolve into soup of quarks and gluons, ii) a phase transition to 'Bose Condensate' of pions and kaons may take place, iii) phase transition to more exotic matter such as hyperons may also occur [19]. For even higher density ($\mu_{\mathrm{B}} \to \infty$) the matter becomes color superconductor forming color Cooper pairs.

A theory of possible existence of deconfined quarks and glouns were proposed, with the discovery of asymptotic freedom. At high energy (or temperature) and high baryon density, the strength of the strong interaction between quarks weakens, thus leading to a deconfined state of quarks and gluons, known as Quark-Gluon Plasma (QGP) [20, 21]. It is believed that after few micro seconds of Big Bang, the universe passed through the QGP phase, from which all the nuclear matter were formed afterwards. Since the transition from normal hadronic matter to deconfined quark is a non-perturbative process, the conventional perturbative QCD approaches are no longer applicable. A new approach which is used to solve this problem is application of Lattice QCD (lQCD). In lQCD, non-perturbative QCD calculations are done numerically on a discrete grid of space time points. The calculations attain continuum QCD in the limit of infinitely small lattice spacings. Undoubtedly, this approach suffers from computational limitation, as numerical calculations get complicated with increasingly small lattice spacing. The corresponding equation of state for the phase transition from hadronic matter to QGP has been obtained from Lattice QCD calculations at finite temperature. The transition temperature is found to be around 180-200 MeV [22] with the required energy density as 1 GeV/fm^3 [23] at $\mu_B = 0$. The results also show that the QGP properties deviate from the ideal gas behavior and indicate that the deconfined and chiral phase transition occur at the same temperature interval.

As u,d and s quark masses do not vanish, the transition from hadronic matter to deconfined one is not a phase transition, rather it is a smooth crossover [23]. Near the critical point at $\mu_B \backsim 0.72$ MeV, the transition seems to become second order [24, 25], while beyond this point, the transition is of a first order.

Although the complete diagram is still not established, the model predictions need to be experimentally verified. Thus, different experiments are engaged in exploring different regions of the diagram.

Search for QGP in heavy-ion collisions

LHC at CERN and RHIC at BNL are aimed to explore the low baryon and the high temperature region of the QCD phase diagram through the ultra-relativistic heavy-ion collisions.

The energy density produced can be indirectly estimated from the charge particle produced per unit rapidity range using: $\epsilon = \frac{\langle m_T \rangle}{\tau_f A}\frac{dN}{dy}$, where $\langle m_T \rangle$ $(=\sqrt{E^2 - p_z^2})$ is the mean transverse mass of the produced charge particle, τ_f is the formation time of the charged particle, A is the overlapping area of the two colliding nuclei and dN is the charge particle multiplicity in the given rapidity range dy [26]. It can be seen that the energy density diverges for $\tau_f \to 0$. So this formula is applicable with the two conditions: i) a finite formation time must be defined, ii) crossing time should be small compared to the formation time.

A schematic view of the colliding medium is shown in Fig.2.6. During the collision, multiple interactions among the participating nucleons give rise to an out-of-equilibrium system of partons, provided the nuclei crossing time is much smaller than the characteristic time of the strong interaction (τ_{strong}) i.e. $\tau_{cross} \ll \tau_{strong} \approx 1/\Lambda_{\mathrm{QCD}} \sim 1\mathrm{fm/c}$, where Λ_{QCD} is the QCD scale parameter. If the energy density achieved by the system crosses the critical energy density (1GeV/fm^3), then QGP formation is expected. The dynamical evolution of such a system is an important tool to study as it decides the fate of the final state particles. Bjorken provided a complete picture of this kind of system [27].

Space-time evolution of matter in heavy-ion collisions

The evolution of the conceived system is accounted in the Landau hydrodynamical model [28]. Few assumptions made for simplification are:

- The characteristic time of the strong interaction (τ_{strong}) should be greater than the nuclei crossing time, which means that the partons are created after the nuclei have crossed each other. In ultra-relativistic heavy-ion collisions, the crossing time is expressed as $\tau_{\mathrm{cross}} = 2\mathrm{R}/\gamma$, where R is the nuclei radius and γ is the Lorentz factor in the center-of-mass system. The condition $\tau_{cross} \ll \tau_{strong}$ is satisfied only if $\gamma > 12$, considering the center-of-mass energies per nucleon

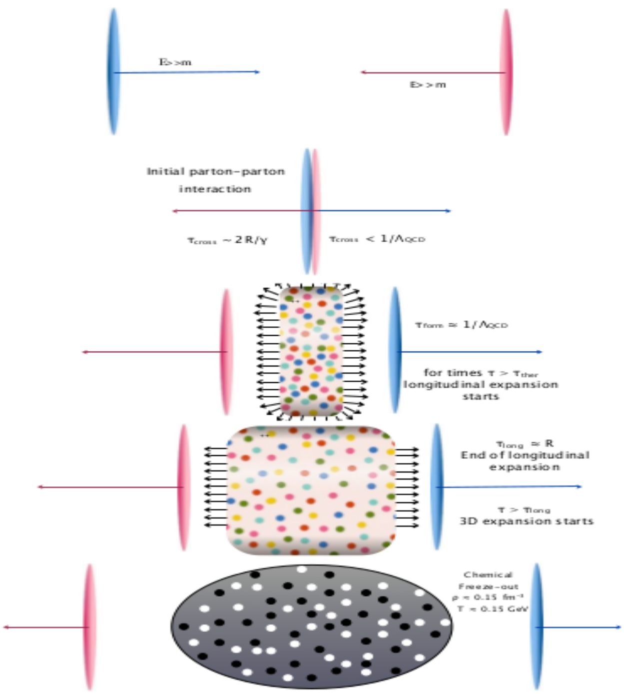

Figure 2.6: A pictorial representation of the relativistic heavy ion collision [14].

above $s_{\rm NN} > 25$ GeV [14].

- The particle production distribution follows a plateau near mid-rapidity. This leads to a symmetry of the system along rapidity, thus simplifying the calculations involving the hydrodynamic equations.

The Bjorken scenario is described below.

Pre-equilibrium ($0 < \tau < 1$ fm/c): The time at which collision of the nuclei occurs is considered as $\tau = 0$. Just after the collision, the partons go through multiple interactions among themselves giving rise to a medium of pre-equilibrium phase. The hard processes with high momentum transfer take place within partons. For example, formation of heavy $q\bar{q}$ pair occurs for gluon fusion at this phase.

QGP formation and hydrodynamic expansion ($1 < \tau < 10$ fm/c): At this phase, the QGP is formed, provided the energy density of the system is sufficiently high. The lifetime of the QGP is decided by the energy density reached in the collision, which is few fm/ c in case of LHC. A pressure gradient due to the difference in density with the surrounding vacuum favours the system to expand.

Mixed state ($10 < \tau < 20$ fm/c): Once the expansion starts, the system gradually cools down. As a result, when the temperature goes below the critical temperature, after about 10^{-23} sec, the hadronization of quarks and gluons gets initiated.

Hadronic gas phase ($\tau \geq 20$ fm/c): Once the hadronization is accomplished, the system is described by an expanding gas of hadrons.

Freeze-out ($\sim$ 50-60 fm/c): This can be viewed in two steps:

- Chemical freeze-out : As the kinetic energy of the created particles becomes too low for inelastic collision, the abundances of hadrons and their ratios become fixed.

- Kinetic freeze-out : When the system further expands, the elastic collisions between hadrons also stops. So the kinematics get fixed at this stage and the hadrons are received by the detector.

The above scenario is illustrated in Fig.2.7.

Different probes to study the QGP in collider experiment

The QGP phase has a very short lifetime. It lasts for a very small time and then subsequent cooling of the system makes the hadron to appear on the detector. Thus, QGP cannot be studied directly, rather we depend on some indirect probes based on the final products to investigate it. Few important probes for QGP are listed here [30].

A probe can deliver a signal for QGP provided its property changes appreciably depending on the formation of QGP phase. As there is no single unequivocal identification probe for QGP, the best way to identify QGP is to rely on several signatures of deconfinement. They are as follows:

Dilepton production in QGP: A quark and anti-quark pair can produce a virtual photon, which further decays to a lepton and anti-lepton pair. This lepton pair propagate through the medium before reaching the detector, as they only interact

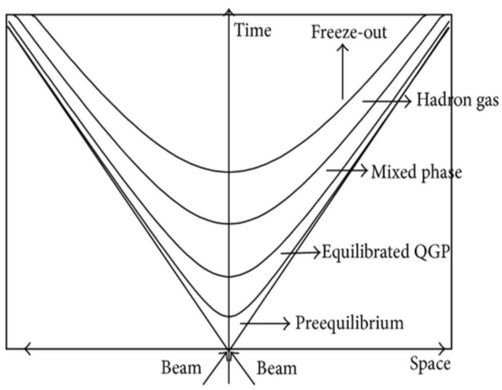

Figure 2.7: Space-time evolution of the matter formed in heavy-ion collisions [29]

electro-magnetically. Due to the fact that the leptons have large mean free path, they are less likely to undergo further collisions making it a reliable diagnostic tool for the thermodynamical state of the medium.

Photon production in QGP: Analogous to the process mentioned above, the properties of the QGP can be studied directly from the emitted photon from the annihilation of a quark-antiquark pair. A gluon can also interact with the quark to create high energy photon associated with a quark.

As photon does not interact strongly, it can also be detected before encountering with too many collisions. It carries the information about the momentum distributions of the quarks and gluons inside plasma, thereby accounting for the thermodynamic state of the system at the time of its birth.

The Hanbury-Brown-Twiss (HBT) effect: When identical particles meet at different space-time coordinates or energy momentum points, an interference occurs due to difference in intensities. Detection of two photons in coincidence in two detectors shows a correlation along the transverse distance of the detectors depending on the angular diameter of the source. This space-time or energy-momentum correlation observed in high energy collisions is called the HBT effect.

The intensity interferrometry is applied for two identical pions detected at coincidence. The momentum correlation of the pions is related back to the phase space distribution function of the chaotic source through its Fourier transform. In this way, this method provides information about distribution of matter during late stages of the collision adding one more dimension to the QGP search.

Strangeness enhancement: In nuclear matter, generally there are small number of valance strange quarks. This number, determined by the dynamical state, usually differs in case of quark gluon plasma. In this medium, due to the interactions between quarks and gluons their momentum distribution changes and the strangeness content may get enhanced due to the chemical non-equilibrium. Thus enhancement in the strangeness can be regarded as a signature of QGP. However, strangeness enhancement does not necessarily mean QGP formation. The Statistical Hadronisation Model (SHM) can describe this phenomena as well. This model is an extension of the Fermi model of hadron production based on the hypothesis that the strong interactions saturate the quantum particle production matrix elements. Therefore, the yield of particles is controlled primarily by the accessible phase space, and not by reaction strength.. The relative yield of hadron resonances are measured to test the statistical hadronisation hypothesis.

Jet Quenching: Energetic partons, which later emerge as hadronic jets, lose energy while passing through the QGP either by elastic collisions or by gluon radiation. Generally at high energy, radiation dominates. Collisional energy loss becomes significant when it comes to intermediate energy partons or heavy quarks. Thus modification in jet profile may be a sign of QGP.

Quarkonia suppression in QGP: Quarkonium is a bound state of quark and anti-quark pair. Our main interest revolves around this state throughout this thesis.

An effect analogous to charge screening in electrodynamics, is seen in strong interaction as well. The color charge gets screened in presence of abundant quarks and gluons in the neighbourhood. This is called Debye color screening, because of which the bonding between a quark and anti-quark pair gets weakened. Also in presence of the plasma, the string potential between them breaks. Thus quarkonium inside QGP will dissociate leading to suppression in the yield in nucleus-nucleus collisions.

Apart from the above, there are other global observables which provide information about the initial energy density, parameters defining collision geometry and dynamics of expansion. The impact parameter of the collision, number of participating nucleons can be determined from the study of charged particle multiplicity [31,32]. Besides, the initial energy density can be estimated from the transverse energy and charged particle multiplicity [33]. The particle spectra and azimuthal anisotropies allow us to estimate the pressure gradient of the expanding medium [34,35].

Charmonium states

The charmonium is bound state of a charm quark and charm antiquark. Due to its high mass, charm quark is expected to be produced predominantly in the early stages of ultra-relativistic nucleon-nucleon collisions. As discussed in the last section, the charmonium can serve as an useful probe to study the QGP.

Table 2.1: Spectroscopic notation and properties of charmonium.

Meson	$n^{2S+1}L_J$	Parity	Mass (MeV)	Width (MeV)
η_c(1S)	1^1S_0	-1	2981.0 ± 1.1	29.7 ± 1.0
J/ψ(1S)	1^3S_1	-1	3096.916 ± 0.011	0.0929 ± 0.0028
χ_{c0}(1P)	1^3P_0	+1	3414.75 ± 0.31	10.4 ± 0.6
χ_{c1}(1P)	1^3P_1	+1	3510.66 ± 0.07	0.86 ± 0.05
h_c(1P)	1^1P_1	+1	3525.41 ± 0.06	< 1
χ_{c2}(1P)	1^3P_2	+1	3556.20 ± 0.09	1.98 ± 0.11
η_c(2S)	2^1S_0	-1	3638.9 ± 1.3	10 ± 4
ψ(2S)	2^3S_1	-1	3686.109 ± 0.034	0.304 ± 0.009

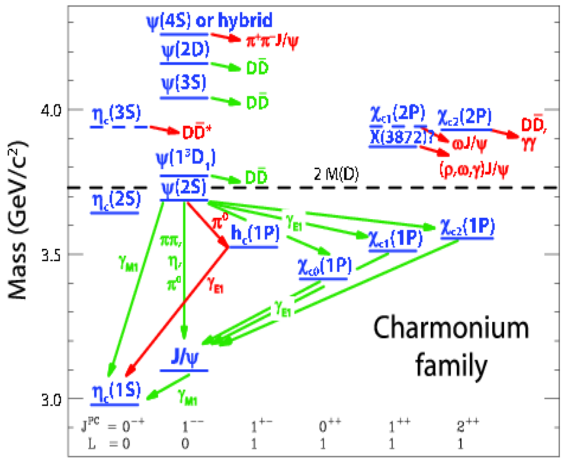

Figure 2.8: The spectroscopy of the charmonium family [36]. n, S, L and J are the principal quantum number, spin angular momentum, orbital angular momentum and total angular momentum of the charmonium.

The characteristics of the various charmonium states are summerized in Table 2.1. Several charmonium states and their decay paths are shown in Fig.2.8. Both J/ψ and ψ(2S) decay into a di-lepton pair. The higher mass states can also decay into the J/ψ through the feed down effect. As a result, J/ψ can be produced either from the direct hadronization of a c and $\bar{\text{c}}$ pair or be a decay product of ψ(2S), χ_c. In hadronic collisions, about 91% of the inclusive J/ψ's are produced in this way (prompt production), of which 60% are from direct production, 30% from χ_c and 10% come from ψ(2S) decays [37–39]. Rest 9% of the inclusive J/ψ production comes from B meson decay [40].

Theoretical models for charmonium production

The production of a c$\bar{\text{c}}$ pair in the colliding medium involves energy scales where perturbative QCD is applicable ($2\mathrm{m_q} \gg \Lambda_{\mathrm{QCD}}$). Example for a leading order production is shown in Fig.2.9.

But, the evolution of the c$\bar{\text{c}}$ pair into the charmonium state involves energy scale of the order of the binding energy $m_c v^2$ (where v is the velocity of the charm quark

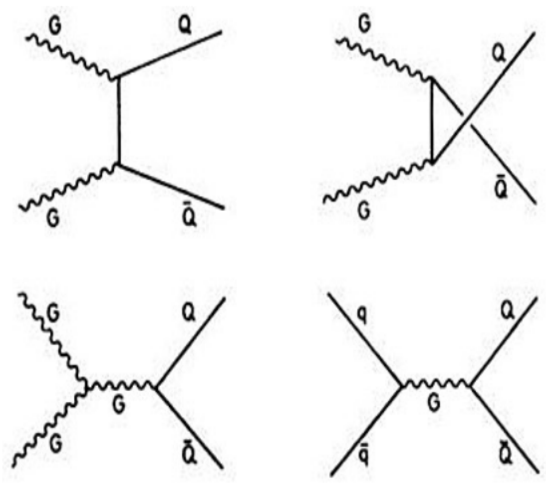

Figure 2.9: Heavy-quark production processes in QCD (Leading order). [41]

as viewed from the charmonium rest frame) which can no longer be described by perturbative QCD. Generally, a $c\bar{c}$ pair is assumed to be produced in 8 color states with a net color charge (color-octet state) and 1 state without color charge (color-singlet state). For hadronisation to take place, the net charge of the pair must be zero. This neutralization of the color charge takes place through interaction with the neighbouring color fields. Following three models have applied to describe this scenario.

Color Evaporation Model (CEM)

This phenomenological model assumes that the hadronisation is uncorrelated from the $c\bar{c}$ pair [42]. The pair exchanges soft gluons with the collision-induced color fields, which breaks the correlation. This concept supports the name "color evaporation". Next, the cross section of a given charmonium state is obtained by multiplying the $c\bar{c}$ cross section with a phenomenological factor which is related to the probability that the pair hadronises into this state ($\mathrm{F}_{\mathrm{quarkonium}}$). $\mathrm{F}_{\mathrm{quarkonium}}$ is an experiment driven number. Mathematically one can write,

$$\sigma_{quarkonium} = F_{quarkonium} \int_{2m_Q}^{2m_M} \frac{d\sigma_{q\bar{q}}}{dm_{q\bar{q}}} dm_{q\bar{q}}. \tag{2.1}$$

Due to its limitation in explaining the p_{T} dependence, it has been upgraded to 'Improved Color Evaporation Model' (ICEM).

Color Singlet Model (CSM)

This is the oldest model which describes the charmonia production [43–47]. The model considers the production of resonance to be completely correlated to the pair production. Therefore, the quark pair must be produced in a color-singlet state with the same quantum numbers as the final bound state. The non-perturbative factor of the quarkonium cross section is then taken in proportion to the bound states wave function or its derivative, which is estimated from the data.

Color Octet Model (COM)

The foundation of the Color-Octet Model (COM) [48] is on the basis of a QCD effective theory called Non-Relativistic Quantum ChromoDynamics (NRQCD) [49]. Using NRQCD it separates the short-distance factors, which take into account the pair creation, from the long-distance matrix elements, which take care the transition to the bound state. The calculations involve summations of all terms running over all possible quantum numbers of the quark pair. In each term, the short distance coefficients are nothing but the perturbatively estimated production rates of the quark pair in the corresponding state n (color, spin and angular momentum), while the long-distance matrix elements basically give the probability of a heavy quark pair in the state n to form the bound state. The long-distance matrix elements are obtained fitting the cross-sections data.

Cold Nuclear Matter (CNM) Efects

The name cold matter suggests that these effects can be found in proton-nucleus collisions, where no presence of QGP is expected. They can both way modify the quarkonium yields, either by suppression or enhancement. Cold nuclear matter effects act in heavy-ion collision as well. To correctly quantify the QGP effect in heavy-ion collisions, cold nuclear matter should be properly disentangled. That is why the study of the cold nuclear matter is extremely important. The CNM effects can be categorised in two classes based on the time frame it takes place: initial and final state effects.

Initial-state effects

Initial state effects act on the partons before the hard scattering takes place. They include nuclear shadowing, anti-shadowing, gluon saturation, parton energy loss and Cronin effect.

Nuclear Shadowing

The information regarding the parton content inside nucleon is stored in the Parton Distribution Functions (PDF). The PDF's ($f_i(x, Q^2)$) depict the probability density of finding a parton 'i' inside the nucleon, with fractional momentum 'x' at energy scale Q^2. The cross section of a hadronic process can be split into a partonic cross section (which is quantified using perturbation) and the PDFs that represent those hadronic bound states. The universal property of PDFs is that, they are independent of type of the process. This feature gives us the freedom to calculate it from particular process and apply it to calculate cross section for any given process. The PDF is applicable in making theoretical predictions for any hadronic process.

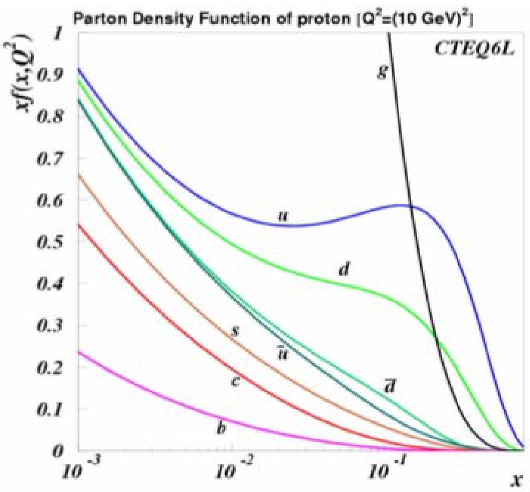

Figure 2.10: The Parton Distribution Functions for $Q^2 = 10$ GeV/c^2 from CTEQ collaboration [50]

An example of PDF (roughly the energy scale relevant for J/ψ production) is shown in Fig. 2.10. These PDF's are calculated taking data from Deep Inelastic Scattering (DIS) experiments and Drell-Yan (DY) production. The larger uncertainty on the gluon distribution is due to the indirect probe from both DIS and DY. The gluon distribution mostly dominates the hard scattering processes at RHIC and LHC.

It has been found that the PDF's calculated from the nuclear DIS experiments [51] get modified for protons which are bound in a nucleus. Due to this, the nuclear parton distribution functions (nPDF's) need to replace the free PDF's.

The modification of the PDF is generally expressed in terms of ratio:

$$R_i^A(x, Q^2) = \frac{f_i^A(x, Q^2)}{f_i(x, Q^2)}, \tag{2.2}$$

where $f_i(x, Q^2)$ is the free nucleon PDF for parton i, $f_i^A(x, Q^2)$ is PDF for the same flavored parton i of a nucleon, but bound in a nucleus A.
An approximate evolution of this ratio is shown in Fig.2.11. From this figure, $R_i^A(x, Q^2)$ can be split into four regions along the x scale.

Shadowing ($x \leq 0.03$, $R_i^A(x, Q^2) < 1$) Clearly, the number of partons, especially of the gluons, decreases in this region, compared to the free proton case. It is assumed that the gluons in low-x get fused into a single high-x gluon, because of the greater density of gluons present in the nucleus, causing deficiency in the low-x region.

Anti-Shadowing (0.03 $\leq x \leq 0.3$, $R_i^A(x, Q^2) > 1$) The same fact is responsible for causing deficit in low-x region and enhancement in this higher x region.

EMC Region (0.3 $\leq x \leq 0.7$, $R_i^A(x, Q^2) < 1$) Tne reason for this observation is yet not ascertained.

Fermi motion ($x > 0.7$, $R_i^A(x, Q^2) \gg 1$) As the name mentions the ratio increases because of Fermi-motion of the nucleons.

We will refer all the four kinds of modifications of PDF's as shadowing in later chapters. As LHC can explore the very low-x region, shadowing will mostly dominate.

Gluon saturation

From the Fig.2.10, at lower values of the x, the density of the gluons starts dominating over that of the quarks. After reaching sufficiently higher energy scale, known as the saturation scale, the individual gluons start overlapping and can no longer be resolved. The number of gluons get saturated at this stage. This energy scale or in

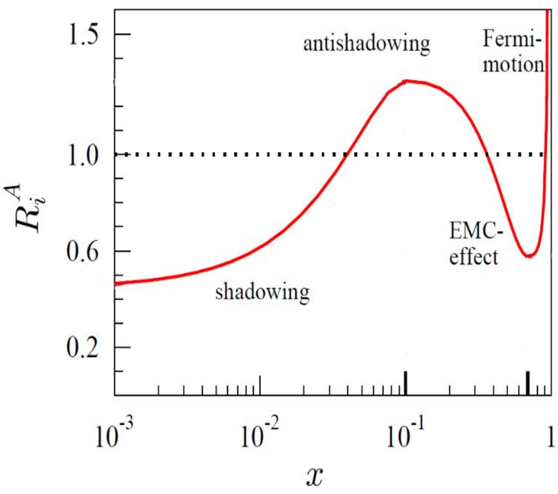

Figure 2.11: A schematic example of the modification of the PDF in nuclei [52].

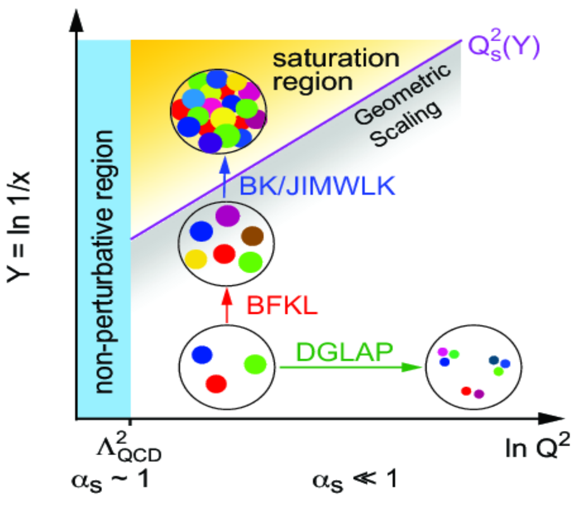

Figure 2.12: A schematic representation of the gluon saturation [53].

other words, Q^2 dependence is shown in Fig. 2.12. The saturation line separates the dilute (DGLAP) regime from the saturation region. The QCD evolution equation for parton densities referred to as DGLAP, are named after Dokshitzer, Gribov, Lipatov, Altarelli and Parisi [54]. Although the Deep Inelastic Scattering (DIS) data are well described by the fits based on the DGLAP evolution equation, there are hints of novel physics events that may exist at very small values of x. Alternatively the parton evolution can be described analyzing the Regge limit in QCD, where the energy of the interaction is assumed to be large s$\rightarrow \infty$, or in the case of the DIS process, when $x \rightarrow 0$, while the scale Q^2 is perturbative but fixed. In this limit the cross section is dominated by the exchange of the so-called hard Pomeron which is the solution to the famous BFKL evolution equation which is useful in describing the fast growth of gluons. The two main differences between DGLAP and BFKL evolution equations are that in the latter the solution shows the power like behaviour, $x^{-\lambda}$ at small values of x and the transverse momenta in the gluon cascade are not ordered [55]. So the solution is dependent on the transverse momenta of the exchanged gluons. To explain the evolution when it approaches the saturation region, Jalilian-Marian-Iancu-McLerran-Weigert-Leonidov-Kovner (JIMWLK) equation is used. It considers the nonlinear correction of the strong field with Wilson renormalization group approach. However, JIMWLK is a complex partial derivative functional equation and it is hard for one to solve. Another nonlinear evolution equation is BK equation, in which the correction due to the resuming of the fan diagrams (two Pomerons merge into one Pomeron) are added to the standard BFKL evolution process [56].

At an energy scale far beyond the Λ_{QCD}, the coupling behaves as weak and it demands of an effective field theory called the Color Glass Condensate (CGC) [57,58]. But CGC framework suffers from the limitation of its applicability through the saturation scale Q_s. However at the LHC energies, CGC has a broader range of rapidity and p_{T} coverage.

If viewed from other perspective, it will not be surprising to consider shadowing and gluon saturation as the same phenomena. They both represent modifications of PDF's. The only difference is that in case of the gluon saturation, this is caused due to coherent interactions of gluons above a particular energy scale, whereas the shadowing considers the nucleus to be a collection of bound nucleons and parametrizes this way.

Coherent parton energy loss

An incoming parton may undergo elastic scattering and thereby lose energy by gluon radiation while traversing the nucleus. This phenomenon occur before the hard scattering process. As a result, the incoming partons momenta get decreased, which is reflected as a shift in the parton distribution if seen compared to pp collisions. Thus the hadron productions are suppressed in p-A collisions.

In general,the energy loss models are standing on the basis of few assumptions and approximations [59]:

- The partons produced in a hard collision may experience several gluon splittings

- Different approaches have been followed to model the medium. For example, few theorists have considered it as a collection of static scattering centres [60].

- Additionally numerous approximations on the parton and gluon kinematics are adopted in all the calculations.

Cronin effect

In p-A collisions, an incoming parton can scatter multiple times inside the nucleus. Due to this multiple scattering, its transverse momentum (p_{T}) spectra get modified with respect to pp collisions. This effect is called Cronin effect.

Final-state effects

The following effects take place post scattering. That is why they fall under final-state effects.

Nuclear absorption

The interactions like multiple scattering between the pre-resonant quark, anti-quark pair with the surrounding nuclear matter can lead to the dissociation of the state. As a result, a suppression of the quarkonium yields may be observed. There are definite ways to treat this case. Generally, nuclear absorption depends on the amount of nuclear matter traversed by the pair. Now the crossing time decreases with increase of collision energy. Therefore the relationship between the crossing time and the pair formation can be extended to a dependence with the collision energy. Apart from the collision energy, nuclear absorption depends on the type of beams and the collision centrality. In experimental data, it can be shown as a function of a parameter 'L' which is defined as the mean path length of the pre-resonant $q\bar{q}$ pair inside the nuclear medium.

Comovers absorption

The suppression of quarkonium can be caused due to comovers such as hadrons like pions and kaons or partons. In this interaction, the charmonium get transformed into pair of D, $\bar{\text{D}}$ mesons leading to a deficit in the charmonium yield.

Hot Matter Effects

The Debye Color screening and the regeneration/recombination are the hot matter effects. They are briefly discussed below.

Debye Color Screening

To understand this effect let us consider a quark of charge 'q' at the origin and another anti-quark of opposite charge '-q' at a distance r. The color potential as viewed by the anti-quark is phenomenologically represented by the Coloumb-like potential,

$$V_0(r) = q/4\pi r \tag{2.3}$$

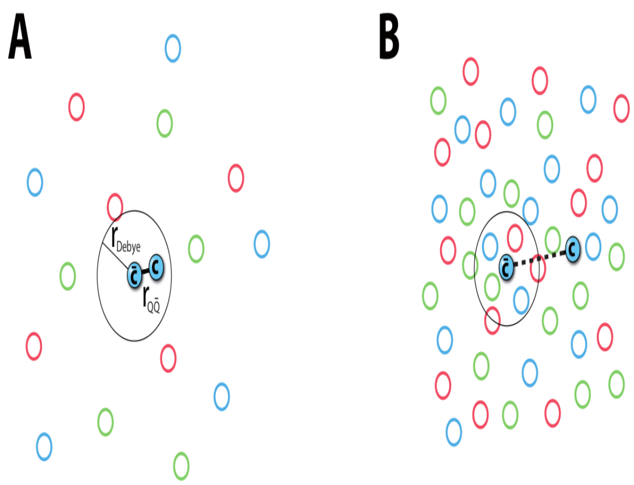

Figure 2.13: The Debye screening in two cases: (A) Debye radius is larger than the binding radius of the quarkonium state, (B) Debye radius becomes much smaller than their binding radius [52].

In addition to the above, there is a linear potential acting on them in proportion to their separation.

$$V_{lin} = kr \tag{2.4}$$

where k is the string constant. Thus the total potential energy can be written as:

$$H_{pot} = \frac{q(-q)}{4\pi r} + kr. \tag{2.5}$$

So, the total energy of such system will be,

$$H = \frac{p^2}{2\mu} - \frac{q^2}{4\pi r} + kr, \tag{2.6}$$

where $\mu = m_q/2$ is the reduced mass of the q$\bar{\text{q}}$ system.

If a quarkonium is placed inside QGP. Two effects occur:

Firstly, the string constant k is temperature dependent quantity. Deconfinement occurs at the disappearance of k. This is another reason as why the temperature required to be high for deconfinement to happen.

Secondly, in presence of the quark matter in the surrounding medium, the densities of quarks, antiquarks get rearranged. Consequently the Coulomb potential gets modified due to color screening. The new potential takes a form of Yukawa short range interaction.

$$V(r) = \frac{q}{4\pi}\frac{e^{-r/\lambda_D}}{r}, \tag{2.7}$$

where λ_D is the Debye screening radius. Beyond this radius the attraction between the constituent quark, antiquark is negligible and the potential value drops exponentially with distance. Moreover, λ_D is inversely proportional to the temperature of the system. Thus at sufficiently high temperature, its magnitude becomes so small that it becomes impossible to bind the quark and antiquark together.

Due to the simultaneous influence of these two effects, the quarkonia may no longer be confined to bound states. They dissociate into free quark, antiquark pair. Another fact which makes the quarkonium, a clean QGP signature is that, they are formed through initial hard scattering and carry the full information of the evolution. We will discuss details of the charmonium state in the next section.

Regeneration/Recombination

Unlike the other effects discussed so far, it is one effect, sometimes called as coalescence, which can enhance the quarkonia yields. In ultra-relativistic heavy-ion collisions, where a large number of $c\bar{c}$ pairs are created per collision (Fig.2.14) and there is a fair chance of two uncorrelated c and $\bar{c}$ forming a bound state. Thus, this effect is expected to be significant for the charmonium family. The sketch drawn in the panel in Fig.2.14, is inspired by a statistical model [61, 62] which assumes for simplicity, that all hadrons including the quarkonia are produced simultaneously during the chemical freeze-out. This model predicts that the charmonium yields are proportional to the square of the number of $c\bar{c}$ pairs. With the increase of this

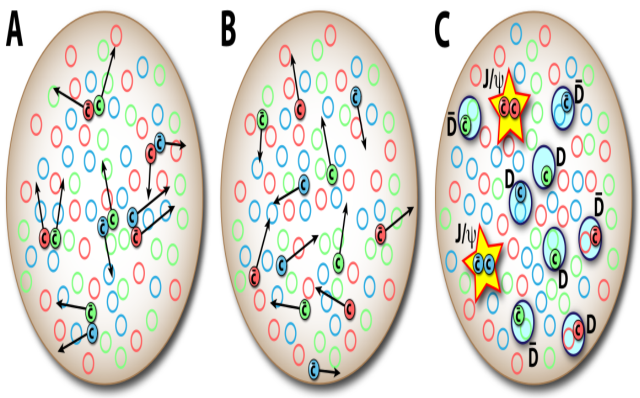

Figure 2.14: The pictorial representation showing the recombination of uncorrelated $c\bar{c}$ pair forming bound state, in three steps [52].

number at LHC, this effect becomes more dominant. So, at LHC energies, it is interesting to look for the recombination effects which will be dominant in $0 < p_{\mathrm{T}} < 4$ GeV/c region.

Bibliography

[1] J. J. Aubert et al., Phys. Rev. Lett. 33 (1974) 1404.

[2] J. E. Augustin et al., Phys. Rev. Lett. 33 (1974) 1406.

[3] T. Matsui and H. Satz, Phys. Lett. B 178 (1986) 416.

[4] http://united-states.cern/physics/standard-model-and-beyond.

[5] S.K. Choi et al. (Belle Collaboration), Phys. Rev. Lett. 91 (2003) 262001.

[6] R. Aaij et al. (LHCb Collaboration), Phys. Rev. Lett. 115 (2015) 072001.

[7] R. Aaij et al. (LHCb Collaboration), Phys. Rev. Lett. 122 (2019) 222001.

[8] R. Aaij et al. (LHCb Collaboration), arXiv:2006.16957, Science Bulletin 65 (2020) 1983.

[9] P. W. Higgs, Phys. Rev. Lett. 13 (1964) 9.

[10] P. W. Higgs, Physics Letters 12 (1964) 2.

[11] P. W. Higgs, Phys. Rev. 145 (1966) 4.

[12] G Aad et al. (ATLAS Collaboration), Phys. Lett. B 716 (2012) 1.

[13] S.Chatrchyan et al. (CMS Collaboration), Phys. Lett. B 716 (2012) 30.

[14] G. Martinez, arXiv:1304.1452.

[15] Particle Data Group 2019.

[16] PhD thesis, Javier Martin Blanco, https://cds.cern.ch/record/2197816/files/CERN-THESIS-2016-070.pdf.

[17] https://www.quora.com/What-is-an-intuitive-explanation-of-chiral-symmetry-breaking, date: 13.01.2021.

[18] H. Reinhardt et al., EPJ Web of Conferences 126, 01002 (2016).

[19] https://www.usra.edu/sites/default/files/discipline/past_highlights/pdf/2017%20USRA%20Developments%20in%20Space%20Research%20Neutron.pdf, 13.01.2021.

[20] J. C. Collins and M. J. Perry, Phys. Rev. Lett. 34 (1975) 21.

[21] R. Pasechnik et al., Phys. Lett. B 59 (1975) 1.

[22] A. Bazavov et al., Phys. Rev. D 80, 2009.

[23] F.Karsch, E.Laermann, arXiv:hep-lat/0305025.

[24] JHEP, vol. 03, p. 014, 2002.

[25] Phys. Lett., vol. B568, pp. 7377, 2003.

[26] K. Adcox et al. (PHENIX Collaboration), arXiv:nucl-ex/0410003v3.

[27] J. D. Bjorken, Phys. Rev. D, vol. 27, no. 1, 1983.

[28] C. Y. Wong, EPJ Web Conf., vol. 7, p. 01006, 2010.

[29] S. K. Tiwari et al., Advances in High Energy Physics June 2013.

[30] ”Introduction to High Energy Heavy-Ion Collisions” book by C.Y. Wong.

[31] B. Abelev et al., Phys. Rev., vol. C88, no. 4, p. 044909, 2013.

[32] J. Adam et al., Phys. Rev., vol. C91, no. 6, p. 064905, 2015.

[33] J. D. Bjorken, Phys. Rev. D, vol. 27, no. 1, pp. 140151, 1983.

[34] U. W. Heinz, Nucl. Phys., vol. A721, pp. 3039, 2003.

[35] R. Snellings, J. Phys., vol. G41, no. 12, p. 124007, 2014.

[36] K. Zhu, arXiv:1212.2169, 2012.

[37] Y. Lemoigne et al., Physics Letters B, vol. 113, no. 6.

[38] L. Antoniazzi et al., Phys. Rev. D, vol. 46, no. 11.

[39] L. Antoniazzi et al., Phys. Rev. Lett., vol. 70, 1993.

[40] R. Aaij et al., Eur. Phys. J., vol. C71, 2011.

[41] https://www.bnl.gov/rhic/news/050807/story1.asp.

[42] H. Fritzsch, Physics Letters B, vol. 67, no. 2, 1977.

[43] M. Einhorn and S. Ellis, Phys. Rev. D, vol. 12, no. 7, 1975.

[44] S. D. Ellis, M. B. Einhorn, and C. Quigg, Phys. Rev. Lett., vol. 36, no. 21, 1976.

[45] C. E. Carlson and R. Suaya, Phys. Rev. D, vol. 14, no. 11, 1976.

[46] E. L. Berger and D. Jones, Phys. Rev. D, vol. 23, no. 7, 1981.

[47] R. Baier and R. Rckl, Zeitschrift fAEr Physik C Particles and Fields, vol. 19, no. 3, 1983.

[48] G. T. Bodwin, E. Braaten, and G. P. Lepage, Phys. Rev. D, vol. 51, no. 3, 1995.

[49] W. Caswell and G. Lepage, Physics Letters B, vol. 167, no. 4, 1986.

[50] J. Pumplin et al., JHEP 0207, 012 (2002).

[51] J.J. Aubert et al., Phys. Lett. B 123, 275 (1983).

[52] PhD thesis, Biswarup Paul, https://cds.cern.ch/record/2063730/files/CERN-THESIS-2015-184.pdf.

[53] https://cds.cern.ch/record/1503432/plots.

[54] http://www.scholarpedia.org/article/QCD_evolution_equations_for_parton_densities, date 13.01.2021.

[55] Deak, M., Kutak, K., Li, W. et al., Eur. Phys. J. C 79, 647 (2019).

[56] X. Wang et al., arXiv:2009.13325v1 [hep-ph]

[57] L.V. Gribov, E.M. Levin, and M.G. Ryskin., Phys. Rept. 100, (1983).

[58] Alfred H. Mueller and Jian-wei Qiu., Nucl. Phys. B268, 427 (1986).

[59] N. Armesto et al., Phys. Rev., vol. C86, 2012.

[60] R. Baier, Y. L. Dokshitzer, A. H. Mueller, S. Peigne, and D. Schiff, Nucl. Phys., vol. B483, 1997.

[61] P. Braun-Munzinger et al., arXiv:0901.2500.

[62] A. Andronic et al., Phys. Lett. B 571 , 36 (2003).

CHAPTER 3

Data taking with ALICE detector

This chapter will focus on the ALICE detector and the different stages of data taking.

CERN houses the Large Hadron Collider (LHC), world's largest and most powerful particle accelerator (Fig. 3.1) [1–3], built to accelerate particles to increasingly high energies. It is giant ring of 27-kilometres with superconducting magnets and a number of accelerating structures to boost the energy of the particles along their path. Two high-energy particle beams move in opposite directions in separate ultrahigh vacuum beam pipes. These beams are made to collide at four points: ATLAS, CMS, ALICE and LHCb.

ALICE (A Large Ion Collider Experiment) was designed to explore the QCD phase diagram. It is the only dedicated detector to study the heavy-ion collisions and investigate the QGP [4, 5]. The central barrel contains an Inner Tracking System (ITS) consisting six planes of high-resolution silicon pixel (SPD), drift (SDD), and strip (SSD) detectors, as viewed from the beam pipe. Next to the ITS, there is a cylindrical Time-Projection Chamber (TPC), followed by three particle identification arrays of Time-of-Flight (TOF), Ring Imaging Cherenkov (HMPID) and Transition Radiation (TRD) detectors. In addition to that, there are two electromagnetic calorimeters installed, called PHoton Spectrometer (PHOS) and Electro-Magnetic Calorimeter (EMCal). Among these detectors, only ITS, TPC, TOF and TRD cover the full azimuth. The Muon Spectrometer (MS) is placed at the forward angle (2 deg-9 deg) for the detection of muons. It includes a front absorber, a large dipole magnet, ten planes of tracking and four planes of trigger chambers.

Apart from the above there are few smaller detectors installed to augment the experimental observations, namely Zero Degree Calorimeter (ZDC), Photon Multiplicity Detector (PMD), Forward Multiplicity Detector (FMD), TZERO (T0), VZERO (V0) which provide the global event characterization and triggering. In case of data taking with cosmic rays, an array of scintillators (ACORDE) was placed on top of the L3 magnet is built for trigger purpose.

Design features

The detector designs have been chosen to meet the required physics motivation and performance graph. Plotting the invariant mass spectra after taking a sample of data gives an idea about the alignment and correct resolution of the detector.

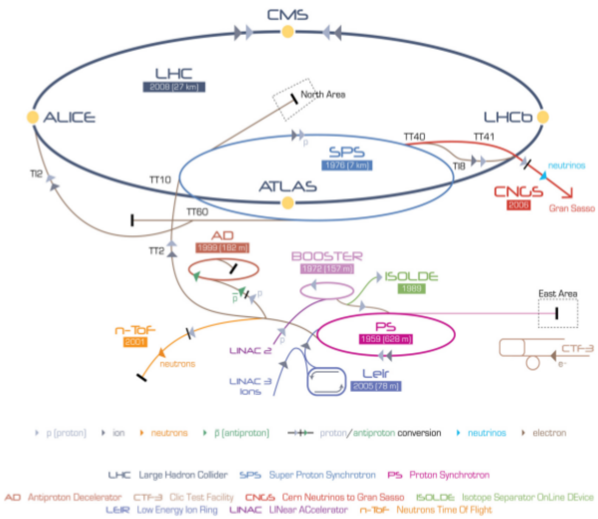

Figure 3.1: Schematic diagram of the accelerator complex of CERN.

The biggest challenge for any detector design in ALICE is the high particle multiplicity in Pb–Pb collisions. Keeping in mind the huge particle flux and maximum energy density at the mid rapidity, the detector acceptance has been made sufficient to cover the particle decays at low momentum as well as jet fragmentation. Some analyses require several thousand reconstructed particles per event. The detector is so designed that a fast triggering is delivered to the concerned detector. To detect rare signals selective triggers are also applied wherever desired (jets, high $p_{\rm T}$ electrons, muons, photons).

A schematic diagram of ALICE detectors is shown in Fig. 3.2. This thesis is based on the analysis done using the data from the forward muon spectrometer. The other detectors involved in the analysis are: (i) Silicon Pixel Detector (SPD) i.e. the innermost detector of Inner Tracking System (ITS); (ii) the two V0 scintillator hodoscopes; (iii) the Zero Degree Calorimeter (ZDC). More emphasis will be put on describing these detectors in the upcoming sections.

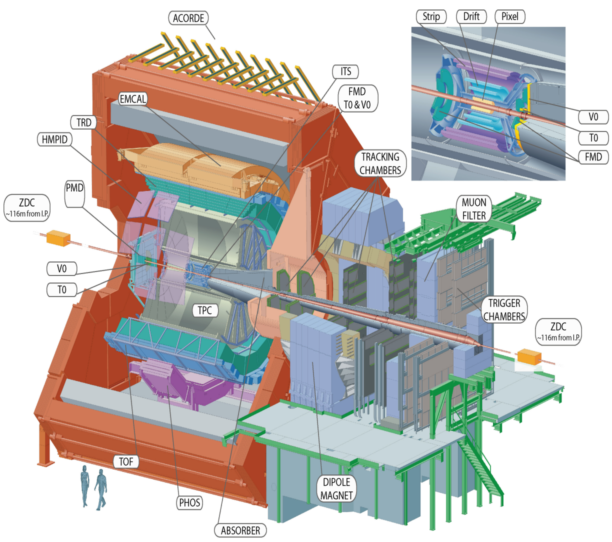

Figure 3.2: A schematic diagram of the ALICE detectors.

Central Barrel Detectors

The central barrel detectors cover an acceptance range of $0.9 < \eta < 0.9$. Their applications vary starting from vertex reconstruction with a resolution better than 100 μm, identification of particles with momentum below 200 MeV/c, to study of the matter produced in the central region. The schematic pictures of different central barrel detectors are shown in Fig. 3.2 and Fig. 3.3.

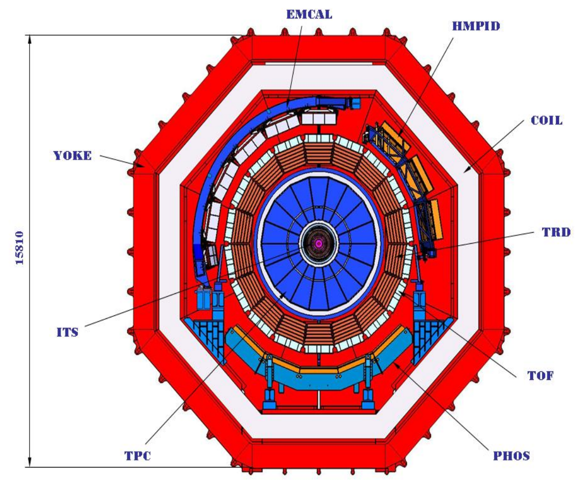

Figure 3.3: The front view of the central barrel detectors.

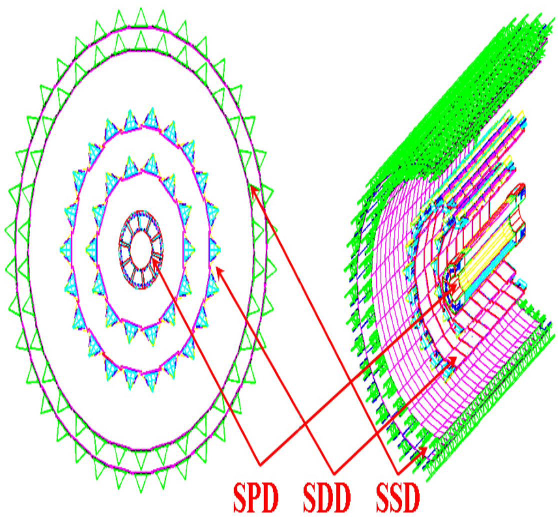

Figure 3.4: The layout of the Inner Tracking System (ITS).

- **Inner Tracking System (ITS), [6]**: To meet the requirement of efficient track finding and high impact-parameter resolution, the number, position and granularity of the tracking layers are optimized. It is made of six layers of silicon detectors based on the requirement of segmentation and schematically shown in Fig.3.4.

  Silicon Pixel Detector (SPD): Being the closest detector to the interaction point, it experiences the highest particle multiplicity during the collision. For that reason, it is constructed in the form of 50 μm x 50 μm pixels. The radius of the innermost SPD layers is so chosen that it provides support to the beam pipe restricting any movement. It has the capacity to handle 80 particles per cm^2 at a rate about 1 kHz. The SPD layers determine the primary vertex position and help in the estimation of the impact parameter of the secondary tracks.

  Silicon Drift Detector (SDD): The intermediate two layers of ITS are made in the form of drifts with the target particle density up to 7 cm^{-2}. For the particle identification, four energy deposits samples are needed, out of which two are given out by the SDD.

  Silicon Strip Detector (SSD): The outermost two layers of the ITS provide matching of tracks from the TPC to the ITS. They are essential for a two dimensional measurement of the track position. In addition they provide energy deposits (dE/dx) information which is crucial for identification of low-momentum particles. The system is designed with minimum material budget so that the low momentum particle will be minimally affected by multiple scattering.

- Time Projection Chamber (TPC, [7]): It also provides the vital information about the particles like transverse momentum and particle identification with corresponding multiplicity, and accurate vertex determination, together with the other central barrel detectors.

- Transition Radiation Detector (TRD, [8]): It mainly provides electron identification in the central barrel for momentum greater than 1 GeV/c.

- Time of Flight (TOF, [9]): It identifies particle in the intermediate momentum range.

  The detectors mentioned above cover the full azimuth. There are few detectors that cover partial azimuth.

- PHOton Spectrometer (PHOS, $|\eta| < 0.12$, [10]): It is aimed to test the thermal and dynamical properties of the initial stage of the collision obtained through low p_{T} direct photon measurements and jet quenching from the measurement of high-p_{T} pion and photon jet correlations.

- Electromagnetic Calorimeter (EMCAL, $|\eta| < 0.7$, [11]): It enables the possibility of unbiased L0 trigger for high energy jets, improves jet energy resolution. This calorimeter enables ALICE to study high momentum photons, neutral hadrons and electrons.

- High-Momentum Particle Identification Detector (HMPID, [12]): As the name indicates, this detector is useful for particle identification for momentum above 1 GeV/c. It is even beyond the momentum interval achievable by energy-loss (in ITS and TPC) and time-of-flight detection (in TOF).

- ALICE Cosmic Ray Detector (ACORDE, $-1.3 < \eta < 1.3$, [13]): It is an array of plastic scintillators located on the upper surface of the L3 magnet. It serves both the detection and trigger purpose. Firstly, it provides a signal for the commissioning, calibration and alignment of some detectors. Secondly, it detects, together with the TPC, TRD and TOF, the single atmospheric muons as well as multiple-muon events.

Forward Detectors

The ALICE forward detectors mainly play a role in estimation of the particle multiplicity and the centrality estimation. The following detectors fall in this category:

- Forward Multiplicity Detector (FMD, $-3.4 < \eta < -1.7, 1.7 < \eta < 5.0$, [14]): As the name indicates, this detector is involved in the estimation of charged-particle multiplicity.

- VZERO detector ($2.8 < \eta < 5.1$ for V0A, $-3.7\eta < -1.7$ for V0C [14]): The V0 detector is a small angle detector which consists of two arrays of scintillators, called V0A and V0C, located asymmetrically on either side of the interaction point. It performs the following actions.

  - it provides the L0 (zeroth level) trigger for ALICE.

  - it provides Multiplicity Trigger (MT), semi-Central Trigger (CT1) and Central Trigger (CT2) in Pb-Pb collisions, which roughly gives estimation on centrality.

  - it measures the charged particle multiplicity, thus resulting in a centrality indicator.

  - it participates in estimation of the luminosity.

  - it helps to rectify the false signals from the muon trigger.

- TZERO Detector (T0, [14]): The T0 detector produces a start time (T0) for the TOF detector. This timing signal corresponds to the real time of the collision (plus a fixed time delay) and is independent of the position of the vertex.

- Photon Multiplicity Detector (PMD, $2.3 \leq \eta \leq 3.7$, [15]): PMD is built to measure the multiplicity and spatial distribution of photons.

- Zero Degree Calorimeter (ZDC, [16]): The ZDC consists of two electromagnetic calorimeters (ZEM) which are placed, on either sides of the LHC beam pipe. Each ZEM consists of two distinct detectors: one for spectator neutrons (ZN), located between the beam pipes and another for spectator protons (ZP), is installed externally to the outgoing beam pipe on the side of positive particles deflection.

  The geometry of the A-A collisions leads to the number of participant nucleons in a collision. To estimate this number, one has to measure the energy carried by the non-interacting (spectator) nucleons in the forward direction (parallel to the beam axis). This is achieved with the help of ZDC. If all the spectators are detected, then the number of participant nucleons in PbPb collisions at 5.02 TeV, can be obtained using: $\mathrm{E_{ZDC}(TeV)} = 5.02.\mathrm{N_{spectators}}$ and $\mathrm{N_{participants}} = \mathrm{A\text{-}N_{spectators}}$. But practically it is difficult to estimate $\mathrm{N_{participants}}$, as all the spectators are not detected.

The Muon Spectrometer ($-4.0 < \eta < -2.5$)

The aim of the Muon Spectrometer is to scan the whole vector meson resonance spectra through their dimuon ($\mu^+\mu^-$) decay channel in pp, pA and AA collisions [17]. In addition to vector mesons like ρ, ϕ, its interest also extends to the study of bosons like Z, W^{+-} and open flavours such as D, B mesons. It can detect muons in their dimuon rapidity range $2.5 < y < 4$ and go as low as $p_{\mathrm{T}} = 0$.

The Muon Spectrometer has the following components:

- Dipole Magnet
- Front Absorber
- Tracking Stations

- Trigger Stations
- Muon Wall
- Beam Shield

Dipole Magnet

To measure the p_{T} of the incoming particle, the tracks need to be bent in a magnetic field.

To fulfill this task, a Dipole magnet is installed about 10 m away from the IP to provide horizontal magnetic field perpendicular to the beam direction (z axis). It also houses the third Muon Tracking station. It covers the pseudorapidity range $2.5 < \eta < 4$. The general idea of the magnet is based on a window-frame return yoke, made of low-carbon steel sheets. It is the world's largest warm dipole magnet of 850 tons (dimension 5 m $\times$ 7 m $\times$ 9m) [18] which provides a nominal field of 0.7 T and a field integral of 3 Tm along the beam axis. An additional space of 10 cm to 15 cm is provided radially to house the support frames of the Muon Trackers inside

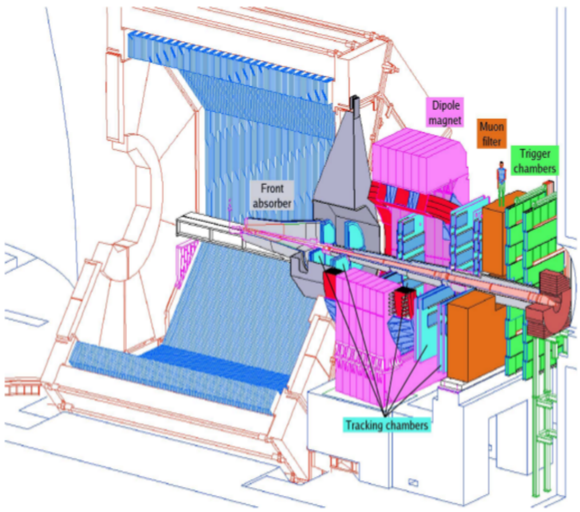

Figure 3.5: The layout of the ALICE Muon Spectrometer.

the magnet. The magnet is also used as a support for the front absorber, the beam shield and the Front Absorber Support Structure (FASS), inside which the first two tracking stations are housed.

Front Absorber

The 4.13 m long front absorber is placed inside the solenoid magnet, at a distance 90 cm from the IP. It is made out of carbon, concrete and steel in a conical shape corresponding to 10 radiation lengths, as shown in Fig 3.6.

The main purpose for building this absorber is to reduce the forward flux of primary hadrons from nucleus-nucleus collisions by at least two orders of magnitude thereby decreasing the muon background by limiting the free path for muons, which originate from pion, kaon decay. Most of the low energetic electrons which are produced inside the absorber, get absorbed by a tungsten cover of 100 mm thickness at the back end. An additional ring of 100 mm of tungsten act as a shield against particles emerging from the beam pipe. Three layers of polyethylene are installed at the end of the absorber in order to stop slow neutrons.

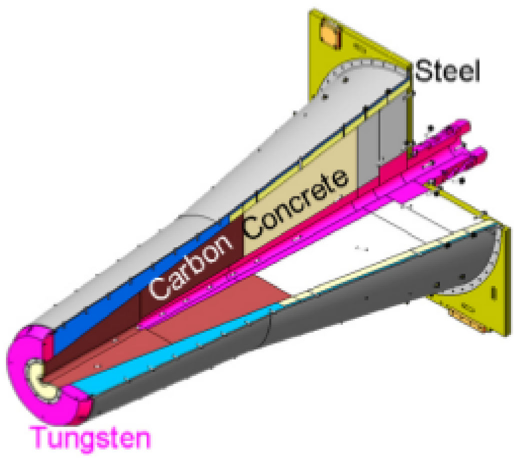

Figure 3.6: The layout of the Front Absorber of ALICE.

Muon tracking chambers

The 10 m long tracking length starts from about 5 m from the IP. Along this length, five tracking stations each containing two tracking chambers are placed. The third station is housed inside the dipole magnet with two other stations on either side of the dipole magnet (Fig. 3.5 and Fig.3.7). The second tracking station, shown on the left side of Fig.3.7, is indigenously constructed in India. The tracking detectors cover a sensitive area of about 100 m^2. In Pb-Pb collisions, muon trackers experience a huge flux of particles which reaches upto a few hundred in central collisions, with a maximum hit density around 5x10^2 cm^{-2}. The tracking chambers are so designed that they can withstand such particle density in the forward direction at the same time provide a spatial resolution of about 100 μm in order to distinguish different resonance states with 95% efficiency. This requirement of good tracking resolution at huge particle flux is achieved by the Cathode Pad Chambers (CPC). The tracking detectors are built in the form of segmented Cathode with anode wires in between the separation between the anodes and cathode planes is 2.5 mm, which is also the anode wire pitch. The detectors are operated with gas mixture of Ar+CO_2

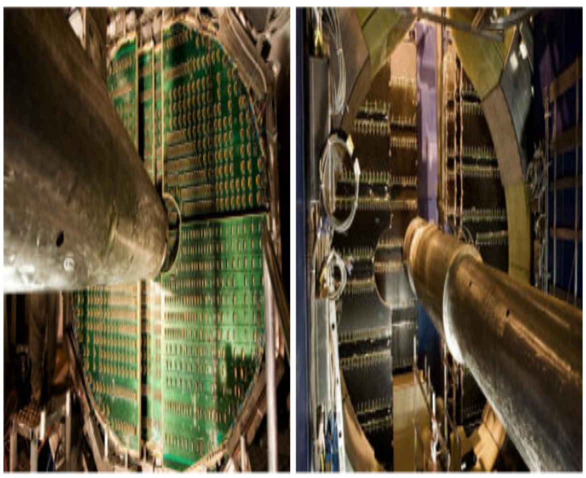

Figure 3.7: The 2^{nd} and 3^{rd} tracking stations of Muon Spectrometer.

in 80%+20% proportion. The choice of this gas mixture gives the detector low efficiency for neutral particles, small Lorentz angle for good spatial resolution and minimizes the detector ageing problem. The applied high voltage on the anode wires is 1650 V.

As shown Fig.3.8, the cathode planes are segmented into definite number of sensitive pads, which are used to determine the position of particle traversing the detector. To know the two-dimesional coordinates of the hit precisely, two informations are needed: hit coordinates in the bending and the non bending planes. The local granularity of the trackers is decided on the basis of their distance from the IP or the expected hit density, i.e. chambers in the 4th station have longer pads compared to that in the 3rd station. The issue of overlapping charge clusters is circumnavigated by shifting the pads on the two cathods relative to each other by half width.

The particle multiplicity not only depends on the distance from the IP, but also on the distance from the beam pipe as well. In order to keep the number of overlapping clusters to be below 1%, the pad occupancy should be less than 5%. To satisfy this condition pads of smaller widths are necessary. For example, pads as small as 4.2 x 6.3 mm^2 are needed in the first station for the region near the beam pipe, where

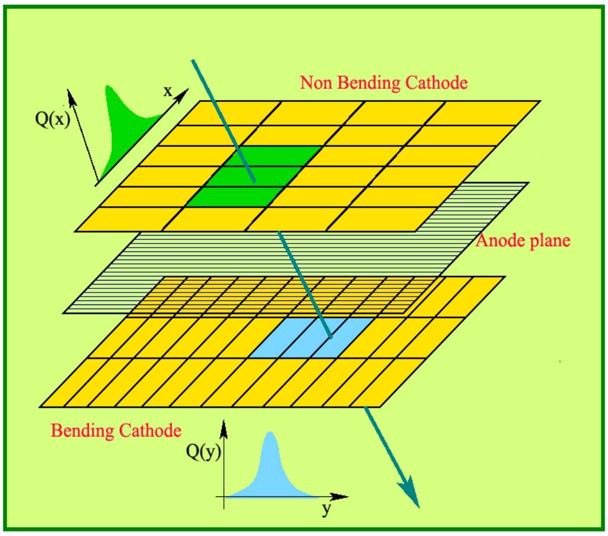

Figure 3.8: The basic working principle of a cathode pad chamber.

highest charged particle multiplicity is expected. Since the hit density decreases with the distance from the beam axis, larger pads are sufficient for the use at larger radii.

The charged particle passing through the active gas volume, ionizes the medium along its trajectory. Due to the high electric field, an avalanche generated by the primary electrons (about 80 in number), which moves towards the closest anode wire. The image charge is induced on both the cathode, which leads to a charge cluster involving three or more pads. The relative values of the induced charges and the absolute positions of the pads in a charge cluster, give the required position of the charged particle inside the detector.

In order to minimize multiple scattering of the muons, the frames of the detectors are made of composite materials with the radiation length below 3%. The sizes of the chambers are gradually increased to maintain the solid angle from the first station to the fifth. The first two stations are built in quadrant structure. Geometry of the other stations are chosen as slat architecture with maximum size as 40 x 280 cm^2.

Muon Wall

The Muon Wall is made of $5.6 \times 5.6 \times 1.23$ m cast iron, located at 15 m from the IP. It is placed in the gap between the tracking station 5 and the trigger station 1. Its job is to reduce the background on the trigger stations by absorbing the pions, hadrons and low momentum muons (from pions and kaons decay) that escape the absorber. Together with the front absorber, the muon wall prevents muons with momentum less than 4 GeV/c from reaching the trigger station thereby enhancing the trigger chamber performance. The picture of muon wall and the dipole magnet is shown in Fig.3.9.

Trigger Stations

The main goal of the muon trigger system is to select unlike sign muon pairs originating from the decay of quarkonia resonances and single muons coming from heavy flavors. In addition to that, like sign muon pairs are selected for generating the combinatorial background for analysis.

In central Pb–Pb collisions, about eight low-p_{T} muons per event from pion and kaon decays are expected to be detected. They contribute to the background in the data, making it difficult to distinguish signal from the background. To reduce this unwanted background to an acceptable level, a low p_{T} cut on the detection of muons that are not accompanied by the high p_{T} ones, is necessary. This requirement is fulfilled by applying a low p_{T} threshold at the trigger level on each muon. Two programmable cuts on high and low p_{T} ranging from 0.5 to 2 GeV/c, are applied in parallel by the trigger electronics so as not to lose signal efficiency. The p_{T} selection is done using a position-sensitive trigger detector with spatial resolution better than 1 cm. Six trigger signals, depending on the combination of types of muons, are sent to the ALICE Central Trigger Processor (CTP), within less than 800 ns after

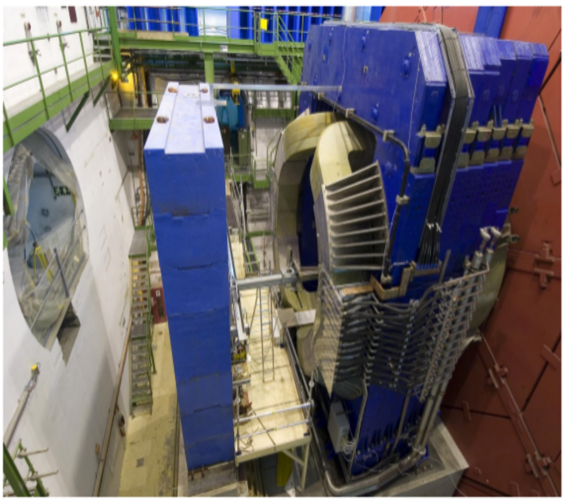

Figure 3.9: A photograph of the Muon Wall (left) and dipole magnet (right).

interaction, at 40 MHz frequency.

The trigger system has two stations each containing two Resistive Plate Chamber (RPC) planes operating in streamer mode (for hit rates less than 50 Hz/cm^2), located behind the muon filter about 16 m and 17 m, from the IP.

The main purposes served by RPC are, fast time response and good time resolution with about 98% efficiency at low background.

The schematic design of a RPC is shown in Fig. 3.10. The gas is allowed to flow through the gap between resistive electrode plates. The high voltage is applied to the plate using a conducting layer coating on their surfaces. The constant distance between the resistive plates (the electrodes) is maintained by plastic spacers placed inside the gap. The RPC is operated at the atmospheric pressure and at a voltage of 4-5 kV/mm. When an ionizing particle crosses the gap between the plates, the electrons create a discharge on the anode, which in turn, gets absorbed by the organic+electronegative gas mixture (Ar + $C_2H_2F_4$ + isobuthane + SF_6 in a ratio 49:40:7:1, decides the spatial resolution). The duration of the discharge (about 10 ns) is much less than the relaxation time of the electrodes. Thus, they behave as an

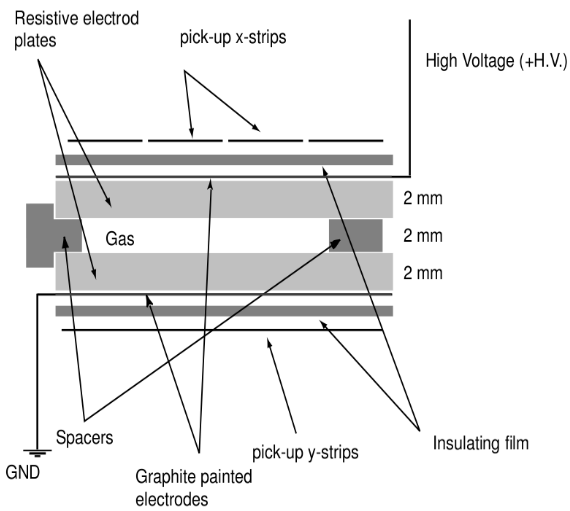

Figure 3.10: The basic layout of a Resistive Plate Chamber.

insulator during the full discharge. The insulated conductive strips placed on the electrodes help to pick up the signal using induction method.

Beam Shield

The front absorber cannot to stop the small angle or secondary particles that emit from the beam pipe. To absorb them, a beam shield made of high atomic number, W-Pb mixture implanted in a 4 cm thick stainless steel cover, is positioned. It surrounds the beam pipe along the Muon Spectrometer following 178° acceptance line up to a maximum radius of 30 cm.

Detector Readout

The read-out electronics of muon spectrometer is based on the principle of an analog multiplexed measurement of induced charges on the pads. A 16-channel chip named MANAS, which works as a charge preamplifier, filter. This ASIC has been designed at SINP and fabricated by the Semiconductor Laboratory (unit of ISR Chandigarh). The muon tracker uses 65,000 MANAS chips to read out 1.1 million pads. The channels of four MANAS chips are connected to two 12-bit ADCs which are read out by the MARC chip. The data is stored after zero suppression. This circuit is mounted on front-end board, named MANU. Total 16,816 of such MANU cards are assembled on the chamber of the second tracking station to read the 1,076,224 pads. MANUs (26) are connected (via PATCH bus) to the translator board from which data transmission to the Concentrator ReadOut Cluster Unit System (CROCUS) takes place. Each chamber is readout by two CROCUS. Thus, a total number of 20 CROCUS in 10 chambers, concentrates data from the chambers and sends them to the DAQ, where the front-end electronics, calibration, dispatch of triggers are controlled. The data link which connecting the top most CROCUS to the DAQ is called Detector Data Link (DDL). This scheme is shown in Fig.3.11.

To identify the bunch crossing, the trigger detector reaction timing should be fast. To achieve a good time resolution (1-2 ns), dual-threshold front-end discriminators are used in the RPCs. The signals from the discriminators are propagated to the trigger electronics i.e. the local trigger cards, where the coordinates estimated in the first and second stations are compared for the rough evaluation of the muon p_{T} . The decision time of the trigger electronics is usually about 600-700 ns.

Online Control System

The successful data acquisition is ensured by several Online Control Systems of ALICE. They are discussed below briefly.

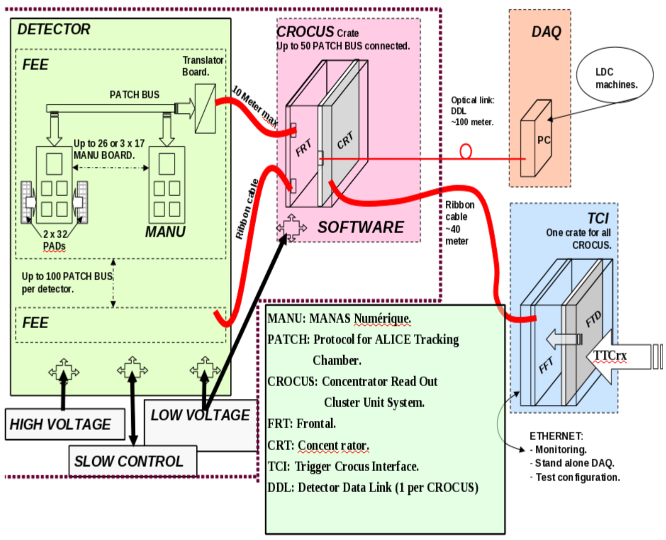

Figure 3.11: A schematic view of the detector readout scheme of ALICE.

Experiment Control System (ECS)

The Experiment Control System (ECS) [19] is at the top level of the online control system which integrates the functions of the online systems for all the detectors of ALICE and within every user defined partition. ECS permits independent, synchronous activities on part of the experiment by different operators. ECS receives status information from the online systems and issues commands to them via interfaces based on Finite State Machines (FSM). The interfaces between the ECS and other components of the online systems include access control mechanisms that manage the rights granted to the ECS. For example, the online systems can either be controlled by the ECS or be operated as independent systems. In the later case the online systems only send status information to the ECS, but do not follow commands from it.

Detector Control System (DCS)

The ALICE Detector Control System (DCS) [20] bears the responsibility of controlling the detector parameters during data taking. By this system, the DCS operator checks the status of the detectors, any error that can affect the data taking and recovers failures so as not to lose the efficiency during data acquisition. The flexible and modular design of DCS enables one to cope with the large variety of different subsystems and equipments at ease. Its main job is to configure, monitor and control all the equipments of the experiment.

Central Trigger Processor (CTP)

The main job of the Central Trigger Processor (CTP) [21] is to collect and process the trigger signals from the detectors participating in data acquisition. Depending on the DAQ (Data Acquisition) bandwidth and the physics requirements events are selected and the corresponding data taking rates are downscaled. The ALICE trigger manages the detectors which become 'busy' for different time intervals after a valid trigger and performs a trigger selection optimized for different running conditions. The fastest trigger signal, called Level 0 (L0), arrives 1.2 μs following one collision. As a result, the inputs from the fast detectors, such as the SPD, V0, T0 and the Muon Trigger are fed to the L0 trigger.

The selection of a certain class of events is performed using logical AND and OR combination of detectors at three states - asserted, not relevant and negated.

Comparatively slower detectors participate in a Level 1 trigger signal (L1) that is sent after 6.5 μs. Other events of given types in a time interval before and after the collision under investigation can also be looked up with the help of a past-future protection circuit connected to the ALICE trigger system.

Finally the last level called Level 2 (L2), is dispatched after 88 μs waiting for the past-future protection. This trigger is used by the TPC.

All the data are stored in the raw data stream. Dedicated scalars are there for all the inputs and for each trigger class that store the number of events passing each of the three stages of trigger (L0, L1, L2).

Data Acquisition System (DAQ)

The ALICE Data AcQusition system (DAQ) [20] is capable of handling large interaction rate and huge data volume (1.25 GB/s). It also manages different clusters of detectors with different trigger rates. The trigger is sent to the front-end readout electronics (FERO) of the participating detectors on receiving decision from the CTP to acquire a specific event. These data are then directed to the Detector Data Link (DDL4) and supplied to a farm of computers, called Local Data Concentrators (LDC). The LDCs create the event chunks from the front-end electronics into sub-events. The sub-events are then injected to the Global Data Collectors (GDC) through an event building network where all the sub-events from various LDCs are collected, ultimately generating the whole event and sending it to the storage.

Data Quality Monitoring (DQM)

The final stage of online control system includes Data Quality Monitoring (DQM). The data that is being recorded must be checked continuously to ensure high quality data taking. In order to do this job, DQM collects the data samples, analyse them itself using user defined algorithms and shows the result in visual form. It uses a platform called AMORE (Automatic MOnitoRing Environment), where the event data are monitored and plots are generated in real time. The DQM shifters can view the monitoring elements and detect potential issues. Other features are also added such as the integration with the offline analysis and reconstruction framework, the interface with the electronic logbook that keeps account for the monitoring results.

Offline Framework

The offline framework is built on a software named AliRoot [23]. It allows the user to fulfill several purposes like simulation, reconstruction, detector alignment, calibration, visualization and data analysis.

The AliRoot architecture is based on the ROOT [24] framework made in a commutable structure as shown in Fig.3.12. This framework is developed on the Object Oriented paradigm, written in C++. The STEER module administers steering, run management, interface classes and base classes. For running simulation and reconstruction, the detector codes are divided into independent modules with specific syntax. The feature of linking with the external Monte Carlo modules for event generation and particle transport through the detector geometry add flexibility to the AliRoot.

- Simulation: The main simulation class is the AliSimulation. In the interface, event generators like PYTHIA [25], HIJING [26] and detector geometry are utilized. As per the requirement, users have the freedom to force the particles to be generated and to decay in a given acceptance range. This feature speeds up the simulation processes and tunes their kinematic parameterizations (namely y and p_{T}) which give the phase space of the particles.

- Particle Transport: The AliRoot provides different Monte Carlo packages (like GEANT3 [27], GEANT4 [28] and FLUKA [29]) which simulate the detector response. The complete geometries of ALICE detectors have been constructed in these packages. The magnetic field maps of the solenoid and the warm dipole magnets are also incorporated in the simulation. To deviate from the ideal geometry, different detector conditions like real time pedestals, noisy or

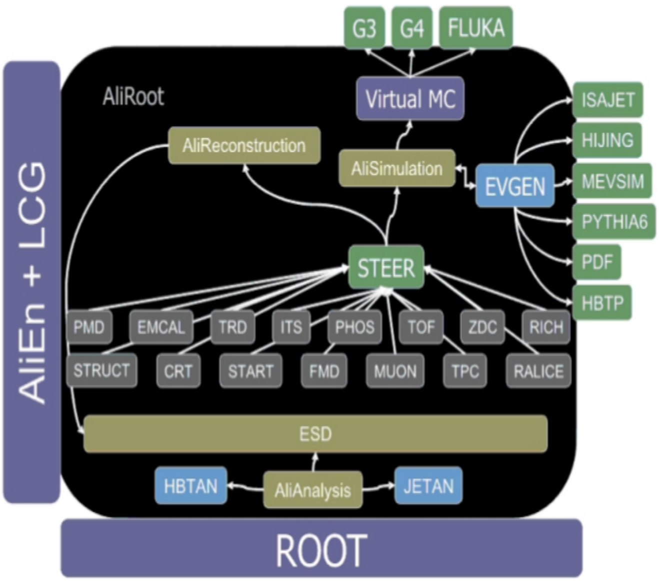

Figure 3.12: The Offline analysis blocks of ALICE.

dead channels and HV trips can be incorporated by taking inputs from the Offine Conditions Data Base objects (OCDB).

- Reconstruction: Once the particle is transported, next comes the reconstruction phase (for both the real data and Monte Carlo simulations). This step makes use of the class AliReconstruction. Calling this class, one can reconstruct both the primary and secondary vertices, tracks and identify particles. Finally the output is written in the form of Event Summary Data (ESD), i.e. a ROOT file which includes all the information relevant for physics analyses [23, 24]. Specific processes such as the offine realignment of the tracking chambers can also be applied during the reconstruction. The ESD files are further passed through filter for more specific analysis and then kept in the Analysis Object Data (AOD) output files which are even smaller in size and can be easily accessible for the users.

  For the analysis presented in this thesis, the Muon Analysis Oriented Data (Muon AOD) files, that summarize all necessary information specific for physics with the Muon Spectrometer, have been used.

The GRID

The world wide computing facility, Grid [30] at CERN made it possible to share the enormous amount of data produced by the LHC experiments with the world. The ALICE computing framework appertains to the program organized by the Worldwide LHC Computing Grid (WLCG). This framework is based on the MONARC [31] model, with hierarchical levels named as Tiers. The raw data are stored at the 0^{th} level of the large computing center at CERN, the Tier-0. The data are then cloned in zonal large computing centers, called Tier-1 which also take part in the reconstruction and the storage of Monte Carlo data. The local computing centers, i.e. the resources of the participating institutes, are called the Tier-2. The two lower levels of this framework are the Tier-3 and Tier-4. They are local computing clusters of University and user's workstations. The interconnections between all these different Tiers are made possible by the Grid Middleware. ALICE has developed a set of Middleware services named AliEn [32]. Through the AliEn User Interface (the MonALISA [33] repository for ALICE), the user is allowed to interact with the Grid (after authentication). The user can access and save files as in a Unix like system, send his analysis tasks (jobs) and monitor their execution in real time with the knowledge of cluster where those files are stored.

The data analysis presented in this thesis has been carried out at Saha Institute of Nuclear Physics using this grid infra-structure.

Data taking

ALICE has taken data in pp, p–Pb and Pb–Pb collisions. In this thesis, analysis of the data in pp, Pb–Pb collisions at centre of mass energy 5.02 TeV and p–Pb collisions at centre of mass energy 8.16 TeV will be discussed.

Once the installation was finished, the positions of the trackers were measured with a precession better than a millimetre using the principle of photogeometry [34]. This alignment is checked time to time, when no data taking goes on. This is done by operating the detectors without magnetic field before start of the data taking and the data is highly affected by the alignment quality. In absence of the magnetic field the tracks are straight, which are used to modify the alignment file offline with the help of Millepede algorithm [35]. The residual misalignment is estimated for each detection element. All these modifications are then propagated to the muon track reconstruction stage.

But, during the data taking when magnetic fields are switched on, these positions get modified. Geometry Monitoring System (GMS), an integrated optical monitoring system made of 460 optical sensors, is installed to keep track of these displacements. In the Fig.3.13, GMS can be seen located on the corners of each Muon Tracking chamber.

This system keeps account of the relative position of two chambers within each station as well as between the different stations, together with the absolute displacement of the entire Muon Spectrometer with respect to the ALICE detectors with about 20 μm a resolution. The alignment can also be checked indirectly with the help of analysis class operating on the online tracks. It uses the idea that improvement in mass resolution implies better alignment.

Track reconstruction

Kalman Filter

The technique for charged-track reconstruction involves pattern recognition for locating the track and once located, fitting the tracks. The charged particles produce

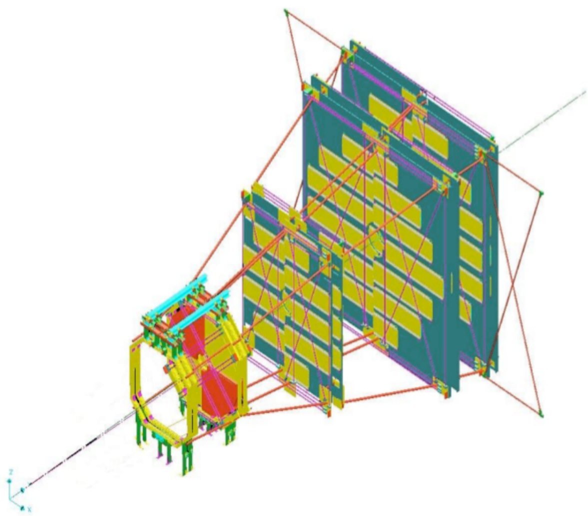

Figure 3.13: The Geometry Monitoring System setup. The optical lines are represented by the red lines.

hits while passing through the chambers. The reconstructed hits are viewed as emerging pattern of tracks which fulfill the condition of at least one hit in each tracking station. The pattern recognition and the track fitting are simultaneously performed using Kalman filter [36, 37]. It employs a set of mathematical equations which gives computational (recursive) solution of the least-squares method.

The algorithm begin with the initial parameters and covariance matrices of track candidates called 'seeds'. Then each track is propagated to some intermediate point. The new covariance matrix is calculated using the Jacobian matrix of the transformation, which is nothing but the matrix of derivatives of new parameters from the propagated track with respect to current parameters.

While extrapolating the point, if a new seed is found within a certain window around it, then the vector of its local measured parameters and covariance matrix are added to the track, and the previously obtained vector of parameters, covariance matrix are updated along with the χ^2 value of the track fitting.

For muon spectrometer, a Kalman track seed is created for all track segments found in the last two stations. The tracks are specified with in terms of the parmeters such as $(y, x, \alpha, \beta, q/p)$, where y and x are the coordinate in bending and non-bending plane respectively, α is the track angle in the bending plane with respect to beam direction, β is the angle made by the track with the bending plane, q and p represent the charge and momentum of the track, respectively.

Once a seed is located, it is followed to the station 1 from station 5 unless it is lost in a station i.e. no hits detected for it as per the procedure. First the track is propagated from the present z-position to a hit with the nearest z -coordinate. Then within a certain window around the transverse track position another hit is searched with the given z-coordinate. This will result in either of the two possibilities. Either one can consider the hit with the lowest χ^2 contribution as belonging to the track or alternatively, one can use a track branching which select all the hits inside the acceptance window. The latter gives better result as proved from the effciency and mass resolution tests. As the magnetic field is usually non-uniform, the Runge-Kutta algorithm has to be used for propagating the track parameters. In order to include the effect of the track chamber material a multiple scattering term is added to the track covariance matrix for each chamber passed.

After propagation to the chamber 1 all tracks are collected depending on their quality, which is defined by:

$$Quality = N_{hits} + \frac{\chi^2_{max} - \chi^2}{\chi^2_{max} + 1} \tag{3.1}$$

The maximum acceptable χ^2 is set to χ^2_{max}. In the next step, tracks having partial share of hits with another track with better quality is removed.

Tracking Efficiency estimation of Muon Spectrometer

The data collected by a muon chamber are limited by the acceptance and efficiency of the detector. So, the data must be corrected with proper acceptance times efficiency (A$\times\epsilon$) of the detector to estimate the cross section of the process of interest. As the determination of the A$\times\epsilon$ is done from Monte Carlo, it is necessary to ensure that the data and experimental conditions during the data taking is properly incorporated in the simulation.

In this chapter, we will discuss the studies of tracking efficiency of Muon Spectrometer carried out for the data collected in pp collisions at $\sqrt{s}$ =13 TeV in 2016, which has been carried out as the Service Task by me for ALICE.

As stated before, the tracking algorithm looks for only one cluster per station in stations 1, 2 and 3 and three clusters in stations 4 and 5. Now, if we assume that the efficiency of one chamber is independent of the others, then the redundancy between the chambers in the stations can be exploited to measure the efficiency of a specific chamber.

For better understanding, a sketch of the arrangement of stations and the possible responses from a station to a track are shown in Fig. 3.14. There are four possibilities: a given track may have a cluster in both the chambers (N_{ij}), a cluster either in chamber i or j (N_{i0} and N_{0j}), or the track does not satisfy the tracking conditions so it is not reconstructed (N_{00}). Combining all the possibilities, the total number of tracks crossing the station (N_{tot}) will be-

$$N_{tot} = N_{ij} + N_{i0} + N_{0j} + N_{00}, \tag{3.2}$$

with the assumption that the efficiency of chamber i (ϵ_{Chi}) is independent of the efficiency of chamber j (for $\epsilon_{Chj \neq i}$). N_{ij}, N_{i0} and N_{0j} can be determined from:

$$N_{ij} = \epsilon_{Chi}.\epsilon_{Chj}.N_{tot} \tag{3.3}$$

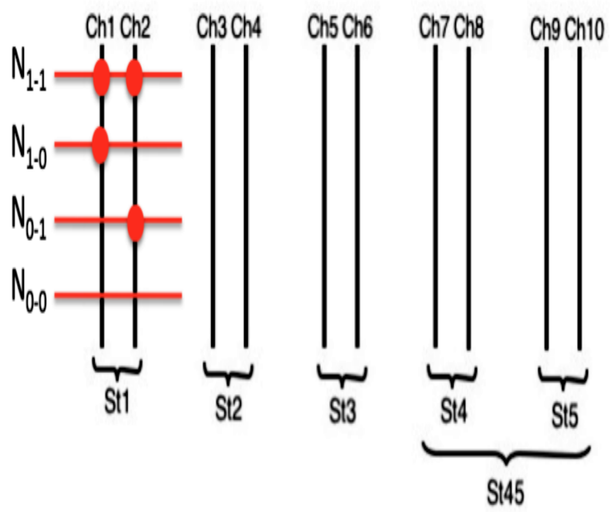

Figure 3.14: The arrangement of the chambers into stations and the probable responses of one station to a track.

$$N_{i0} = \epsilon_{Chi}.(1 - \epsilon_{Chj}).N_{tot} \tag{3.4}$$

$$N_{0j} = \epsilon_{Chj}.(1 - \epsilon_{Chi}).N_{tot} \tag{3.5}$$

But N_{0-0} cannot be expressed in this way, as it is never measured. So the total number of tracks remain unknown. If the chamber has non-zero efficiency, then these equations can be combined to give ϵ_{Chi} and ϵ_{Chj}.

$$\epsilon_{Chi} = \frac{N_{i-j}}{N_{i-j} + N_{0-j}} \tag{3.6}$$

$$\epsilon_{Chj} = \frac{N_{i-j}}{N_{i-j} + N_{i-0}} \tag{3.7}$$

For the first three stations the chamber efficiency can be determined from the reconstructed tracks for which the other chamber has sent response. The same method can be repeated to calculate the efficiency for the last four chambers using the tracks for which the other three chambers have sent responses.

This procedure can be applied locally as well to determine the efficiency of a certain area of a chamber, like a particular Detection Element (DE), Bus Patch (BP), PCB or MANU. These subregions in the chambers are highlighted in Fig. 3.15. The convention of numbering of the DE is: DE number = Chamber number + DE number in the chamber. The calculation of DE inside the chamber begins from the right hand side of the chamber and follws anti-clockwise direction. The individual chamber efficiencies are then combined to determine the efficiency of each station. In case of the stations 1, 2 and 3, the efficiency is defined as the probability for a muon to be detected by at least one of the two chambers:

$$\epsilon_{St4-5} = \prod_{i=7}^{i=10} \epsilon_{Chi} + \sum_{i=7}^{i=10} \left((1 - \epsilon_{Chi}) \prod_{j=7, j \neq i}^{j=10} \epsilon_{Chj} \right) \tag{3.8}$$

At last the tracking efficiency for single muons can be determined from,

$$\epsilon_{tracking} = \epsilon_{St1}.\epsilon_{St2}.\epsilon_{St3}.\epsilon_{St4-5}. \tag{3.9}$$

Tracking efficiency systematics studies for the pp data

In this section the studies performed by me on the data in pp collisions at 13 TeV as a part of the service task for ALICE, will be discussed. In addition, the efficiency as a function of the run number will also be presented.

The first step of this method is to estimate single muon tracking efficiency in data from the reconstructed tracks. Then the results so obtained, are compared to those

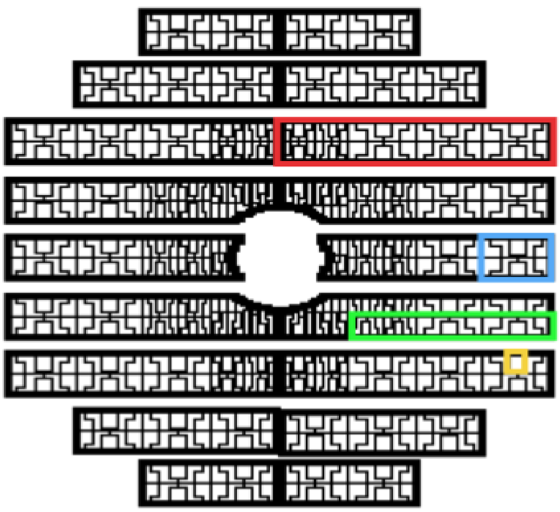

Figure 3.15: Visualization of different substructures for chamber 6: DE (red), PCB (blue), BP (green) and MANU (yellow).

in MC.

Efficiency calculation in real data

As a starting point, the overall single muon tracking efficiency, $\epsilon_{tracking}$, is examined on a run by run basis, If any issue is found, then the source of the issue is searched by looking at the individual chamber efficiency.

The efficiency as a function of run number is then studied for each DE of faulty chambers, if found in the previous step. The overall efficiency is not affected if there are efficient DEs in front of the dead ones because of the redundancy of the detection planes in the stations. Thus the problem will not be that serious in those cases.

The tracking efficiency varies between different parts of the detector and the efficiency measurements are an average over the acceptance region. Therefore, the MC must be tuned on the corresponding data to reproduce the distribution of muons across the chambers, giving similar weights to different parts, to make comparable efficiency measurements.

Comparison data-MC efficiency results

In this section comparison is shown between the results obtained from real data with the ones from Monte Carlo (MC) simulation. It is important that the two data samples are not too different, otherwise the tracking estimation cannot be relied on and we will have to go back to the tuning stage again. Usually the efficiency is found to be variable along the period. The variation of the efficiency as a function of ϕ and y may denote the existence of low efficient regions in the detector, while the p_{T} dependence turns out to be quite flat. The shape of the measured tracking efficiency in data is more or less well reproduced by the simulation. They are also checked by applying different kinematic cuts.

Finally the evaluation of the systematic uncertainty on tracking efficiency consists of evaluating the difference from tracking efficiency computed from the tuned MC and from the data. The comparison plots of results from MC and data together with the efficiency plot is shown in Fig. 3.16, 3.18, 3.17 and 3.19.

From the comparison plots versus p_{T}, y and phi, we can estimate the systematics to $\sim 0.5\%$ at single muon level, thus $\sim 1\%$ for dimuon.

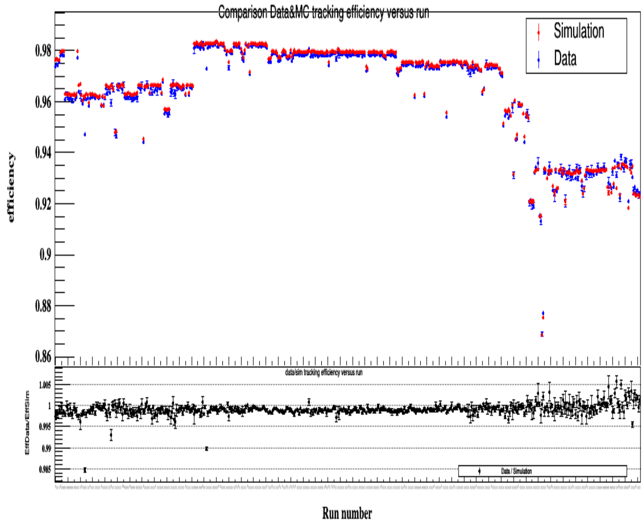

Figure 3.16: The tracking efficiency as a function of run number.

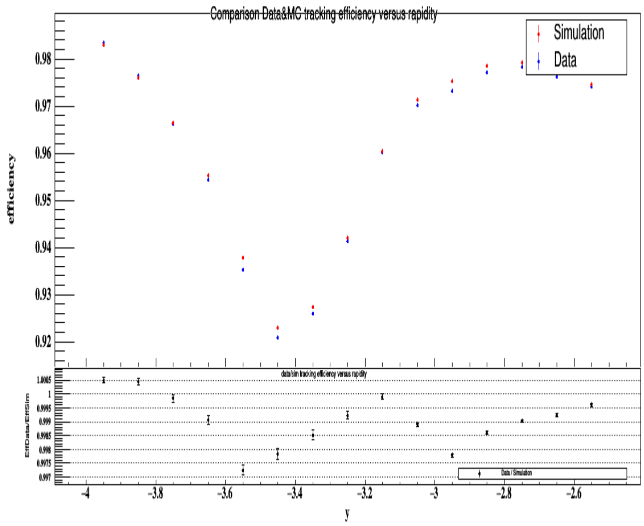

Figure 3.17: The tracking efficiency as a function of rapidity.

Data Processing

As a first step, the Event Summary Data (ESD) are generated with the help of standard re-alignment process (Pass1) which considers specific sets of data previously recorded in absence of the magnetic field. The tracks are reconstructed and their positions with respect to the clusters produced by the pads hit by incoming particles are determined. The track parameters must be tuned to ensure that the

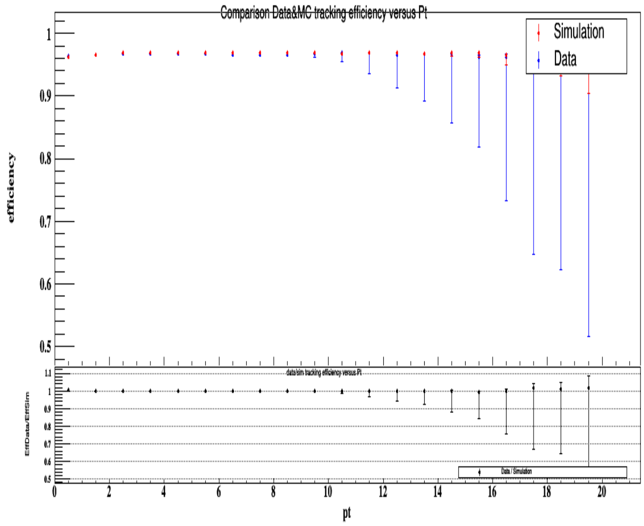

Figure 3.18: The tracking efficiency as a function of p_{T}.

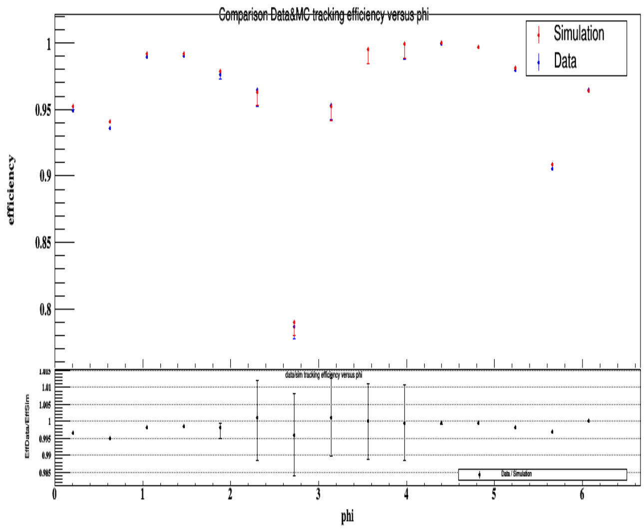

Figure 3.19: The tracking efficiency as a function of azimuthal angle.

position differences observed between tracks and clusters are minimized. The raw data reconstruction is further revised to improve the quality necessary for analysis.

In most of the cases, a second even third ESD production (Pass2, Pass3) are made with a much more efficient alignment procedure incorporating also other modifications that are done later.

Trigger definitions

Minimum Bias (MB) trigger

As per the convention, the minimum bias (MB) trigger for ALICE (CINT7) is defined by the coincidence between the two V0 detectors (V0-A and V0-C) together with the passage of the two colliding beams. It has high triggering efficiency ($> 98\%$) for hadronic interaction. The cross section of the MB trigger, calculated through a van der Meer (vdM) scan [6], is important for the determination of the integrated luminosity.

p_{T} trigger threshold

The p_{T} trigger threshold is defined as the value where the trigger efficiency for single muon comes out to be 50%.

Dimuon trigger

The unlike sign (like sign) dimuon trigger is defined as the coincidence of the MB trigger with the detection of two opposite-sign (same-sign) muon triggers with one p_{T} greater than the low p_{T} trigger threshold.

For the analyses discussed in this thesis, we have used unlike sign dimuon triggered (CMUL7 trigger) events.

Track selections

In order to improve the purity of the muon tracks and reduce the background as much as possible, the following selection criteria are applied in the analysis task:

- Both muon tracks reconstructed by the tracking chambers should be above the low p_{T} threshold (0.5 GeV/c) of the trigger stations. This condition rejects light hadrons which escape from the front absorber. It also removes a part of the low-p_{T} muons coming mainly from pion and kaon decays.

- the tracks must be in the pseudo-rapidity range -4 $< \eta <$ -2.5. This condition is imposed to reject the particles induced by beam-gas interactions those occur at the edges of the detector.

- The dimuon rapidity should lie in the range: 2.5 $< y <$ 4.0.

- the transverse radius of the track, at the end of the absorber (R_{abs}), must be within the range 17.6 $<$ $\mathrm{R_{abs}}$ $<$ 89.5 cm. When the tracks cross the high density material close to the beam pipe, it may suffer from multiple Coulomb scatterings. This selection criteria significantly reject these tracks thereby improving the mass resolution.

  To ensure that the tracks point to the interaction vertex, another condition is sometimes applied for PbPb or pPb collisions. This condition check whether the tracks momentum (p) times the distance of the extrapolated track to the transverse plane containing the vertex (DCA: Distance of Closest Approach) (known as $p\times$ DCA), lies below an acceptable value. This will help in reducing the amount of fake tracks contaminating the muon sample which contributes to the combinatorial background.

Future ALICE Upgrade Program

ALICE is planning for data taking > 10 nb^{-1} of Pb–Pb collisions with luminosity reach upto $6 \times 10^{27} cm^{-2} s^{-1}$ at a collision rate about 50 kHz during run3 period. The data will be either Minimum Bias or self-triggered. Thus event rate will be 100 times higher than the current statistics. So, the ALICE detectors together with the readout electronics need upgrade.

In the upgrade plan, following tasks are enlisted.

- Replacement of the present sillicon tracker
- Upgrade other sub-detectors to be capable of reading 50 kHz Pb–Pb collisions, 200 kHz pp and p–Pb collisions
- New implementation of the online system
- installation of GEM based readout detectors in TPC
- Upgrade of the CTP to maintain high trigger rate
- Installation of new detector called Muon Forward Tracker (MFT) for better resolution of the high mass resonances
- Replacement of the readout electronics of the Muon Spectrometer

Bibliography

[1] O. S. Bruning, P. Collier, P. Lebrun, S. Myers, R. Ostojic, J. Poole, and P. Proudlock, “LHC Design Report Vol.1: The LHC Main Ring,” CERN-2004-003-V1, 2004.

[2] O. S. Brning, P. Collier, P. Lebrun, S. Myers, R. Ostojic, J. Poole, and P. Proudlock, “LHC Design Report Vol.1: The LHC Infrastructure and General Services,” CERN- 2004-003-V-2, 2004.

[3] M. Benedikt, P. Collier, V. Mertens, J. Poole, and K. Schindl, “LHC Design Report Vol.3: The LHC Injector Chain,” CERN-2004-003-V-3, 2004.

[4] “The ALICE experiment at the CERN LHC”, JINST 3 S08002 (2008).

[5] “The Forward Muon Spectrometer of ALICE:addendum to the technical proposal for a Large Ion Collider experiment at the CERN LHC”, CERN-LHCC-96-032 ; LHCC-P-3-ADD-1.

[6] The ALICE Collaboration. “ITS Technical Design Report”. CERN-LHCC, 99-12 (1999).

[7] The ALICE Collaboration. “TPC Technical Design Report”. CERN LHCC, 2000-001 (2000).

[8] The ALICE Collaboration. “TRD Technical Design Report”. CERN-LHCC, 2001-021 (2001).

[9] The ALICE Collaboration. "TOF Technical Design Report". CERN-LHCC, 2000-012 (2000).

[10] The ALICE Collaboration. "PHOS Technical Design Report". CERN-LHCC, 99-4 (1999).

[11] The ALICE Collaboration. "EMCAL Technical Design Report". CERN-LHCC, 2006-014 (2006).

[12] The ALICE Collaboration. "HMPID Technical Design Report". CERN-LHCC, 98-19 (1998).

[13] A. Fernndez et al., "ACORDE a cosmic ray detector for ALICE", Nucl. Instrum. Meth. A 572 (2007) 102.

[14] The ALICE Collaboration. "Forward Detectors: FMD, T0 and V0 Technical Design Report". CERN-LHCC, 2004-25 (2004).

[15] The ALICE Collaboration. "PMD Technical Design Report". CERN-LHCC, 99-32 (1999).

[16] The ALICE Collaboration. "ZDC Technical Design Report". CERN-LHCC, 99-5 (1999).

[17] The ALICE Collaboration. "The forward muon spectrometer". Addendum to the ALICE Technical Proposal. CERN-LHCC, 96-32 (1996).

[18] D. Swoboda. "ALICE Muon Arm Dipole Magnet". ALICE Internal Note, 1999-06 (1999).

[19] https://accelconf.web.cern.ch/ica05/proceedings/pdf/O1_011.pdf

[20] The ALICE Collaboration. "Trigger, Data Acquisition, High-Level Trigger and Control System Technical Design Report". CERN-LHCC, 2003-062 (2003).

[21] D. Evans et al. “The ALICE central trigger processor”. CERN-LHCC, 2005-038 (2005).

[22] T. Alt et al. “The ALICE high level trigger”. J. Phys. G 30 , S1097-S1100 (2004).

[23] http://aliweb.cern.ch/Offine.

[24] http://root.cern.ch.

[25] S. Mrenna et al. “PYTHIA 6.4 Physics and Manual”. JHEP 0605 , 026 (2006).

[26] M. Gyulassy et al. “HIJING 1.0: A Monte Carlo program for parton and particle production in high energy hadronic and nuclear collisions”. Comp. Phys. Comm. 83 (2-3), 307-331 (1994).

[27] M. Goossens et al. “GEANT: Detector Description and Simulation Tool”. CERN program library long write-up, W5013 (1994).

[28] S. Agostinelli et al. “Geant4 - a simulation toolkit”. Nucl. Instrum. Meth. A 506 (3), 250-303 (2003).

[29] G. Battistoni et al. “Applications of FLUKA Monte Carlo code for nuclear and accelerator physics”. Nucl. Instrum. Meth. B 269 (24), 2850-2856 (2011).

[30] I. Foster et al. Morgan Kaufmann Publishers, 1999.

[31] http://monarc.web.cern.ch/MONARC.

[32] http://alien2.cern.ch.

[33] http://monalisa.cern.ch/monalisa.html.

[34] A. Behrens et al. “Positioning strategy, metrology and survey in ALICE”, EDMS 884850 (2007).

[35] V. Blobel. “Software alignment for tracking detectors”. Nucl. Instr. Meth. A 566 (1):5-13, 2006.

[36] P. Billoir and Q. Qian, Nucl. Instr. and Meth. A 294 , 219 (1990).

[37] R. Fruhwirth, Nucl. Instr. and Meth. A 262 , 444 (1987).

[38] The ALICE Collaboration. “Technical Design Report for the Upgrade of the ALICE Read-out & Trigger System”. CERN-LHCC-2013-019 (2014).

CHAPTER 4

ψ(2S) production in pp collisions at $\sqrt{s}$ = 5.02 TeV

In this chapter, we shall discuss the inclusive production cross section of ψ(2S), in pp collisions at $\sqrt{s} = 5.02$ TeV at forward rapidity ($2.5 < y < 4$). The integrated cross section has been found to be: $\sigma_{\mathrm{J}/\psi} = 5.88 \pm 0.03 \pm 0.34$ μb, $\sigma_{\psi(2\mathrm{S})} = 0.865 \pm 0.055 \pm 0.100$ μb, where the first (second) uncertainty is the statistical (systematic) one. Results on the transverse momentum (p_{T}) and the rapidity (y) dependence of the production cross sections are presented for J/ψ and ψ(2S), as well as the differential ψ(2S)-to-J/ψ cross section ratio. The increase in the statistics collected in pp collisions at $\sqrt{s} = 5.02$ TeV allows to study for the first time the differential ψ(2S) production cross sections.

A comparison has been shown with the previous pp measurements at $\sqrt{s} = 7$, 8 and 13 TeV, which helps to establish the energy dependence of quarkonium production cross sections. In addition, the comparisons with several model calculations which consider prompt and non-prompt charmonium production have been reported.

The signal extraction, Monte Carlo simulations, evaluation of the acceptance $\times$ efficiency, estimation of experimental uncertainties and cross sections have been done as a part of this thesis work.

Data samples

The analysis discussed in this chapter is based on the data collected in 2017 corresponding to an integrated luminosity of L_{int}= 1229.9 ± 0.4 nb^{-1}. For the analysis, we have used the pass1 dataset of AOD files, which contained most updated information for the analysis.

Signal extraction

The fit of the Opposite-sign dimuon invariant mass spectra has performed in each p_{T} and y interval considered.

In the $2 < m_{\mu^+\mu^-} < 5$ GeV/c^2 mass region, the fit is performed using the same functional form to describe the J/ψ and ψ(2S) signals, together with the conventional function to describe the background.

For the fit, tests are built by combining:

- Two functions for the signal description : extended Crystal Ball function (CB2) [1, 2] and pseudo-Gaussian functions (used by the NA60 experiment) [2, 3].
- Two functions for the background description : variable width Gaussian (VWG) and a combination of a fourth order polynomial and an exponential functions (Pol4.Exp).
- Two invariant mass ranges : $M_{\mu^+\mu^-} \in [2, 5]$ GeV/c^2 and $M_{\mu^+\mu^-} \in [2.2, 4.5]$ GeV/c^2.

- ψ(2S)/J/ψ width ratios: 1.05 ± 5% obtained by fitting the high-statistics data sample in pp collisions at $\sqrt{s} = 13$ TeV [15], where the J/ψ and ψ(2S) widths were left free.

Again, three sets of tails have been used for the signal functions:

- from the embedding MC simulation using GEANT3 transport code [6].
- from the MC simulation with using GEANT4 transport code [7].
- from fitting the dataset in pp collisions at $\sqrt{s} = 13$ TeV keeping the tail parameters of the CB2 function free.

leading to a total of 60 tests. The extended Crystal Ball consists of a Gaussian core with a power-law tail towards the low mass region to account for the energy loss effects caused by the crossing of the front absorber (radiative decays, pair production, Bremsstrahlung). In order to consider the effect of multi-Coulomb scatterings in the front absorber and alignment biases, an additional power-law tail is also required at higher mass. On the other hand, the NA60 function includes a Gaussian-core around the resonance pole along with two tails on the both side of the Gaussian-core, expressed as Gaussian with mass-dependent widths. The functional forms of these funstions are given in appendix. The J/ψ mass pole and width are left free during the fit procedure, while the ψ(2S) mass is bound to the J/ψ one by the mass difference between the two states taken from the PDG [4]:

$$m_{\psi(2S)} = m_{J/\psi}^{FIT} + \Delta m^{PDG} \tag{4.1}$$

$$\sigma_{\psi(2S)} = \sigma_{J/\psi}^{FIT} * 1.05(\pm 5\%) \tag{4.2}$$

Formulas to calculate average (N), statistical error (σ^{stat}) and systematic uncertainty (σ^{syst}) are:

$$N = \frac{\sum w_i.N_i}{\sum w_i}, \; \sigma^{\text{stat}} = \frac{\sum w_i \sigma_i^{\text{stat}}}{\sum w_i} \text{ and } \sigma^{\text{syst}} = \sqrt{\frac{\sum w_i N_i^2}{\sum w_i} - N^2} \tag{4.3}$$

where, N_i is number of J/ψ or ψ(2S) for test i and σ_i^{stat} is the statistical error on test i, provided by the fit. Here σ^{syst} is obtained from the RMS of the 60 values.

The raw J/ψ yield is found to be $N_{\text{J}/\psi} = 101285 \pm 452$ (stat.) $\pm$ 3012 (syst.) for p_{T} below 20 GeV/c, and the ψ(2S) raw yield is found to be $N_{\psi(2\text{S})} = 2086 \pm 133$ (stat.) $\pm$ 150 (syst.) for $p_{\text{T}} < 12$ GeV/c. Figure 4.1 shows an example of fit of the OS dimuon invariant mass spectrum in the mass region $2 < m_{\mu^+\mu^-} < 5$ GeV/c^2, exhibiting the two charmonium resonance states.

Examples of raw J/ψ and ψ(2S) yield extractions as outcome of the 60 fits are shown in Fig. 4.2 and 4.3 for the $0 < p_{\text{T}} < 2$ and $6 < p_{\text{T}} < 12$ GeV/c, respectively. The dashed line in the figure denotes the range of systematics uncertainty in the yield, while the solid line denotes the mean value of the number distributions.

The number of raw ψ(2S) and J/ψ yields are reported in Table 4.1 and 4.2, for the different p_{T} bins. The number obtained after adding those numbers linearly is also shown on the same table to check the yield in the range $0 < p_{\text{T}} < 12$. This number is closely matching with the ψ(2S) and J/ψ yields obtained by fitting the integrated mass spectra.

In Table 4.3 and 4.4, the raw ψ(2S) and J/ψ yields are reported in 6 rapidity bins.

ψ(2S) to J/ψ raw yield ratio

The ψ(2S)-to-J/ψ yield ratio has been calculated for each of the combination in order to reduce the systematic uncertainties on signal extraction. The statistical and systematic uncertainties on the ratio are then evaluated in the same way as in

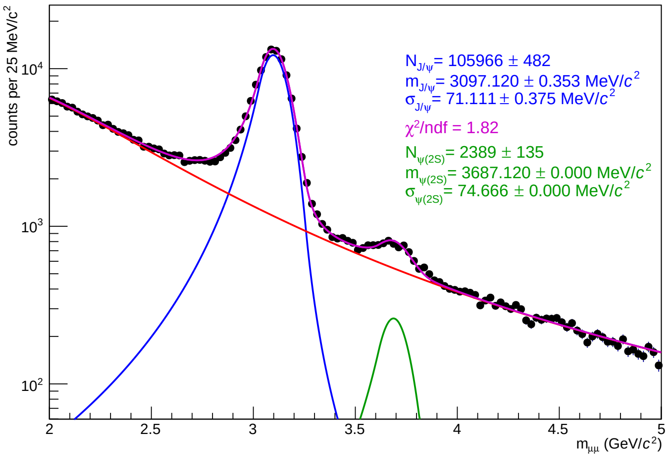

Figure 4.1: A typical fit to the OS dimuon invariant mass spectra in the mass region $2 < m_{\mu^+\mu^-} < 5$ GeV/c^2 for $p_{\rm T} < 20$ GeV/c.

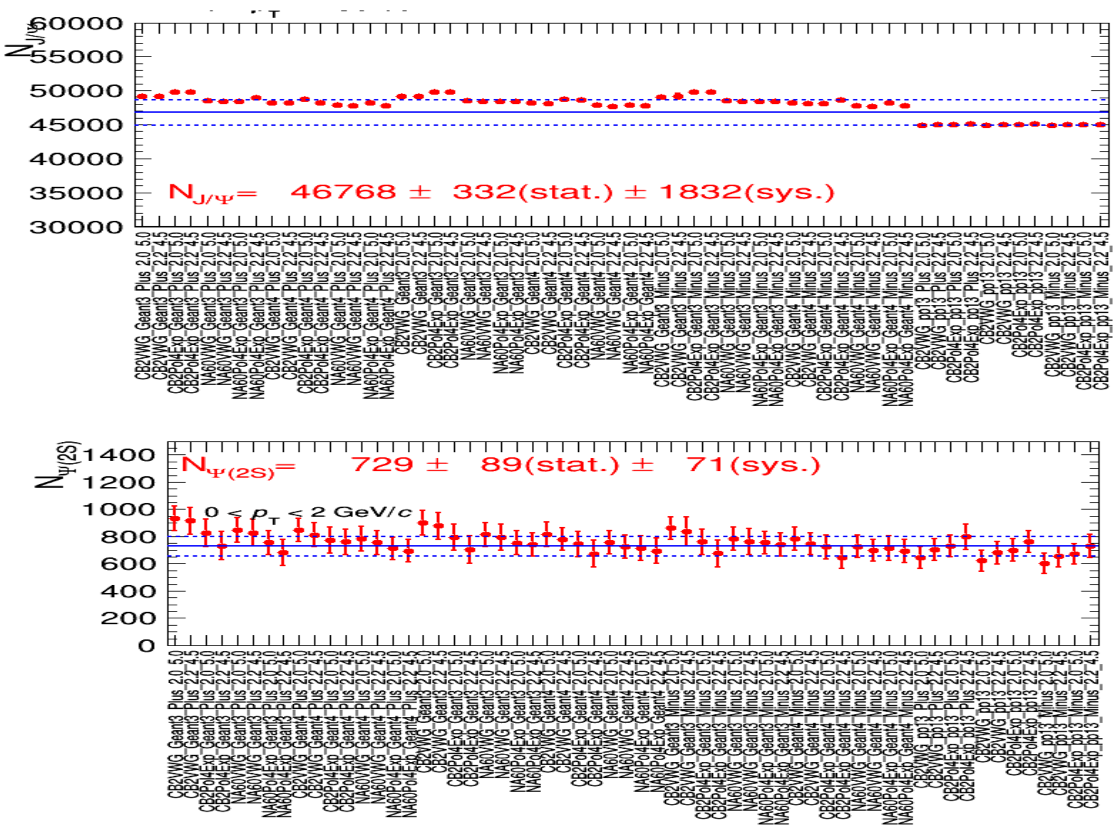

Figure 4.2: J/ψ and ψ(2S) raw yields as a function of the tests performed for the range $0 < p_{\rm T} < 2$.

the case for the J/ψ and ψ(2S) raw yields. The cross section ratio of ψ(2S) over J/ψ has been obtained to be, 0.1458 ± 0.0092 ± 0.0065.

The yield ratio of ψ(2S) over J/ψ has been plotted in Fig. 4.4, 4.5, 4.6, 4.7, 4.8 for

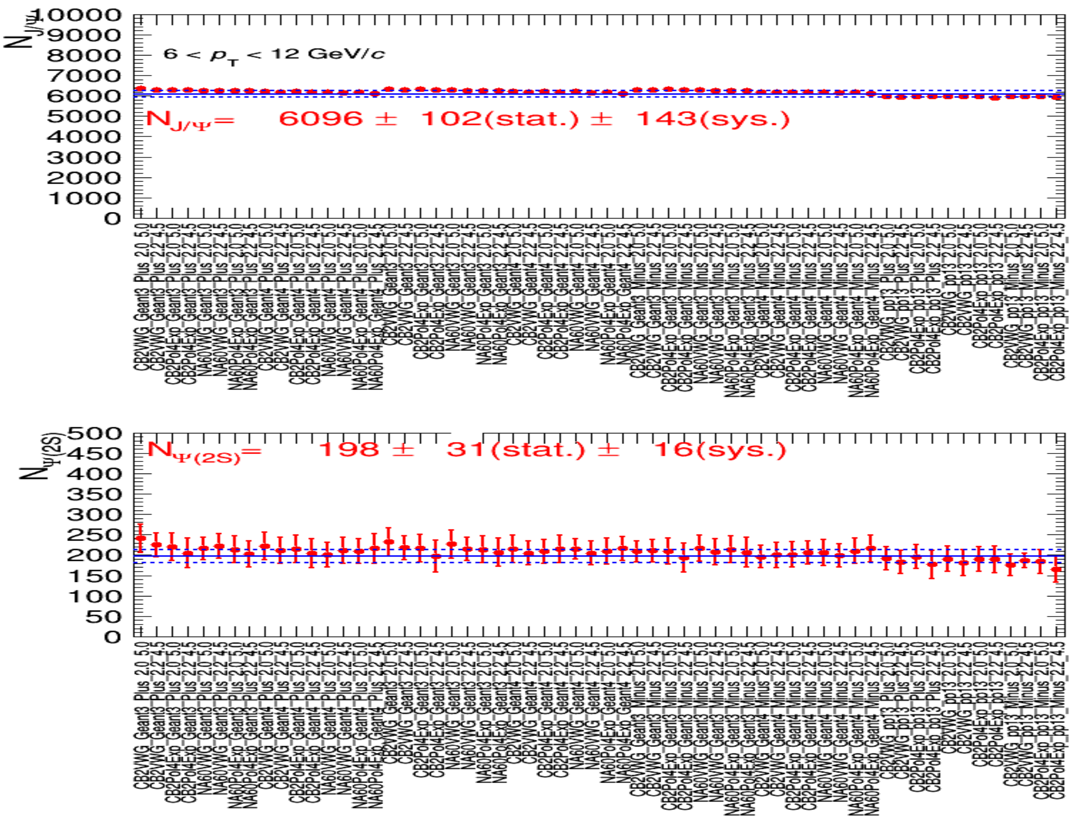

Figure 4.3: J/ψ and $\psi(2S)$ raw yields as a function of the tests performed for the range $6 < p_{\mathrm{T}} < 12$.

Table 4.1: Number of $\psi(2S)$ for different p_{T} bins. First uncertainty is statistical the second one is the systematic on the signal extraction.

p_{T} (GeV/c)	$N_{\psi(2S)}$
$0 < p_{\mathrm{T}} < 1$	192 ± 52 (26.9%) ± 30 (15.6%)
$1 < p_{\mathrm{T}} < 2$	539 ± 72 (13.5%) ± 44 (8.2%)
$0 < p_{\mathrm{T}} < 2$	729 ± 89 (12.3%) ± 71 (9.7%)
$2 < p_{\mathrm{T}} < 3$	626 ± 67 (10.5%) ± 36 (5.8%)
$3 < p_{\mathrm{T}} < 4$	228 ± 49 (22.1%) ± 23 (14.0%)
$4 < p_{\mathrm{T}} < 5$	228 ± 38 (16.5%) ± 26 (10.41%)
$5 < p_{\mathrm{T}} < 6$	103 ± 26 (24.3%) ± 9 (8.7%)
$6 < p_{\mathrm{T}} < 7$	68 ± 20 (27.5%) ± 8 (11.8%)
$7 < p_{\mathrm{T}} < 8$	41 ± 14 (33.3%) ± 6 (14.6%)
$8 < p_{\mathrm{T}} < 12$	87 ± 19 (22.1%) ± 7 (8.0%)
$6 < p_{\mathrm{T}} < 12$	198 ± 31 (16.0%) ± 16 (8.1%)
$0 < p_{\mathrm{T}} < 12$ (adding)	2112 ± 133 (6.3%) ± 88 (4.2%)

the bins $0 < p_{\mathrm{T}} < 12$, $1 < p_{\mathrm{T}} < 2$, $7 < p_{\mathrm{T}} < 8$, $3.5 < y < 3.75$ and $2.5 < y < 2.75$ respectively. The dashed lines in the figures denote the ranges of systematics in the

Table 4.2: Number of J/ψ for different p_T bins. First uncertainty is statistical, the second one is the systematic on the signal extraction.

p_T (GeV/c)	$N_{J/\psi}$
$0 < p_T < 1$	16725 ± 204 ± 736 (4.4%)
$1 < p_T < 2$	29985 ± 263 ± 999 (3.3%)
$0 < p_T < 2$	46768 ± 332 ± 1832 (3.9%)
$2 < p_T < 3$	22337 ± 219 ± 637 (2.8%)
$3 < p_T < 4$	14107 ± 167 ± 402 (2.8%)
$4 < p_T < 5$	8168 ± 122 ± 219 (2.7%)
$5 < p_T < 6$	4740 ± 88 ± 117 (2.5%)
$6 < p_T < 7$	2743 ± 67 ± 76 (2.8%)
$7 < p_T < 8$	1498 ± 51 ± 35 (2.3%)
$8 < p_T < 12$	1838 ± 58 ± 46 (2.5%)
$6 < p_T < 12$	6096 ± 102 ± 143 (2.4%)
$0 < p_T < 12$ (adding)	102209 ± 468 ± 2002 (1.9%)

Table 4.3: Number of $\psi(2S)$ for different y bins. First uncertainty is statistical, the second one is the systematic on the signal extraction.

y	$N_{\psi(2S)}$
$2.5 < y < 2.75$	158 ± 41 (25.6%) ± 20 (12.6%)
$2.75 < y < 3.0$	465 ± 64 (13.8%) ± 43 (9.2%)
$3.0 < y < 3.25$	518 ± 67 (12.9%) ± 35 (6.8%)
$3.25 < y < 3.5$	526 ± 63 (11.9%) ± 30 (5.7%)
$3.5 < y < 3.75$	309 ± 49 (15.5%) ± 27 (8.7%)
$3.75 < y < 4.0$	116 ± 28 (24.3%) ± 16 (13.9%)
$2.5 < y < 4.0$	2086 ± 133 (6.4%) ± 150 (7.2%)

Table 4.4: Number of J/ψ for different y bins. First uncertainty is statistical, the second one is the systematic on the signal extraction.

y	$N_{J/\psi}$
$2.5 < y < 2.75$	6912 ± 129 ± 362 (5.2%)
$2.75 < y < 3.0$	21639 ± 225 ± 761 (3.5%)
$3.0 < y < 3.25$	27349 ± 236 ± 776 (2.8%)
$3.25 < y < 3.5$	23973 ± 221 ± 576 (2.4%)
$3.5 < y < 3.75$	16658 ± 177 ± 424 (2.5%)
$3.75 < y < 4.0$	5521 ± 101 ± 206 (3.7%)
$2.5 < y < 4.0$	102049 ± 468 ± 3120 (3.0%)

evaluated mean yield ratios.

The yield ratio values obtained in differential p_T and y bins are reported in Table

4.5.

Table 4.5: ψ(2S) to J/ψ raw yield ratio for different p_{T} and y bins. First uncertainty is the statistical one, the second is the systematic one. In addition, the uncertainty 7.5% due to BR are taken to be correlated.

bin	$N_{\psi(2S)}/N_{J/\psi}$ ratio
$0<p_{\mathrm{T}}<1$	0.0115 ± 0.0030 ± 0.0016 (13.9%)
$1<p_{\mathrm{T}}<2$	0.0180 ± 0.0024 ± 0.0012 (6.7%)
$2<p_{\mathrm{T}}<3$	0.0280 ± 0.0029 ± 0.0011 (3.9%)
$3<p_{\mathrm{T}}<4$	0.0162 ± 0.0035 ± 0.0013 (8.0%)
$4<p_{\mathrm{T}}<5$	0.0279 ± 0.0046 ± 0.0028 (10.0%)
$5<p_{\mathrm{T}}<6$	0.0218 ± 0.0054 ± 0.0016 (7.3%)
$6<p_{\mathrm{T}}<7$	0.0251 ± 0.0070 ± 0.0023 (9.2%)
$7<p_{\mathrm{T}}<8$	0.0274 ± 0.0095 ± 0.0033 (12.0%)
$8<p_{\mathrm{T}}<12$	0.0476 ± 0.0102 ± 0.0033 (6.9%)
bin	$N_{\psi(2S)}/N_{J/\psi}$
$2.5<y<2.75$	0.0229 ± 0.0057 ± 0.0024 (10.5%)
$2.75<y<3.0$	0.0215 ± 0.0029 ± 0.0018 (8.4%)
$3.0<y<3.25$	0.0190 ± 0.0024 ± 0.0011 (5.8%)
$3.25<y<3.5$	0.0220 ± 0.0026 ± 0.0009 (4.1%)
$3.5<y<3.75$	0.0185 ± 0.0029 ± 0.0012 (6.5%)
$3.75<y<4.0$	0.0209 ± 0.0050 ± 0.0022 (10.5%)

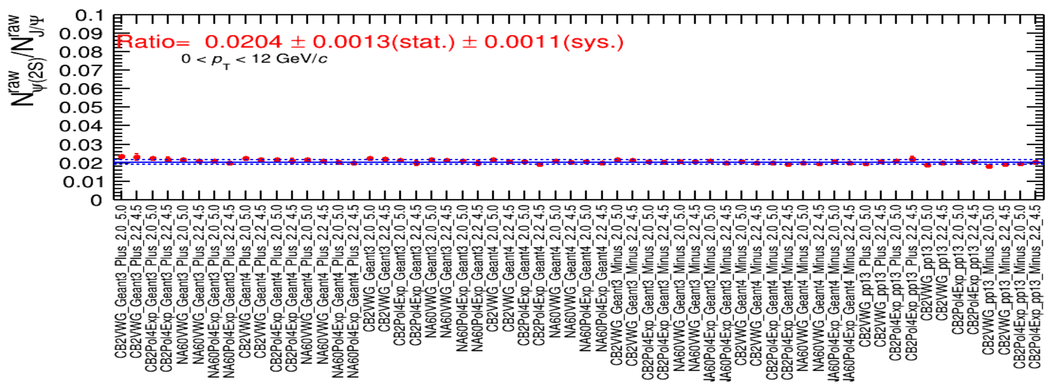

Figure 4.4: ψ(2S) to J/ψ ratio as a function of the tests performed for $0 < p_{\mathrm{T}} < 12$.

Acceptance and efficiency corrections

The charmonium raw yields need to be corrected with the acceptance times efficiency $(A \cdot \epsilon)$ of the muon spectrometer. It is taken as the ratio of the number of

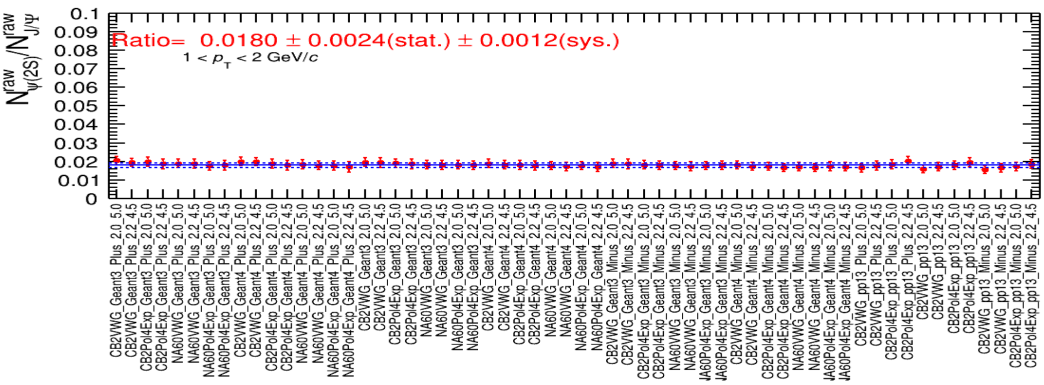

Figure 4.5: ψ(2S) to J/ψ ratio as a function of the tests performed for $1 < p_{\mathrm{T}} < 2$.

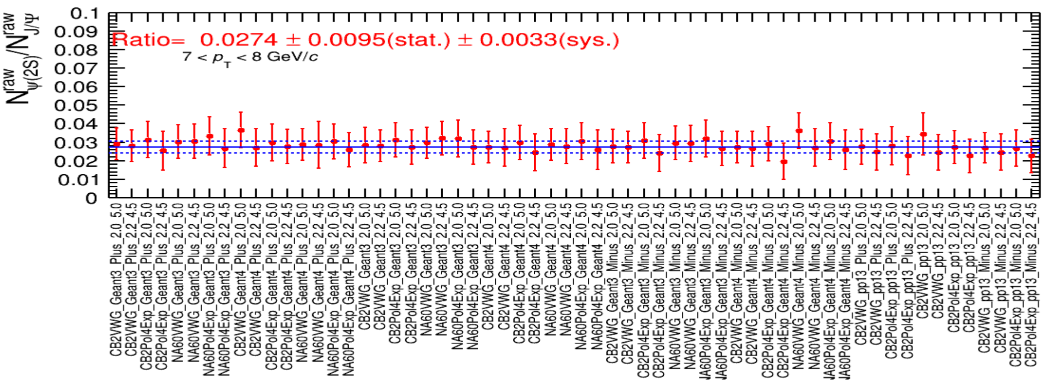

Figure 4.6: ψ(2S) to J/ψ ratio as a function of the tests performed for $7 < p_{\mathrm{T}} < 8$.

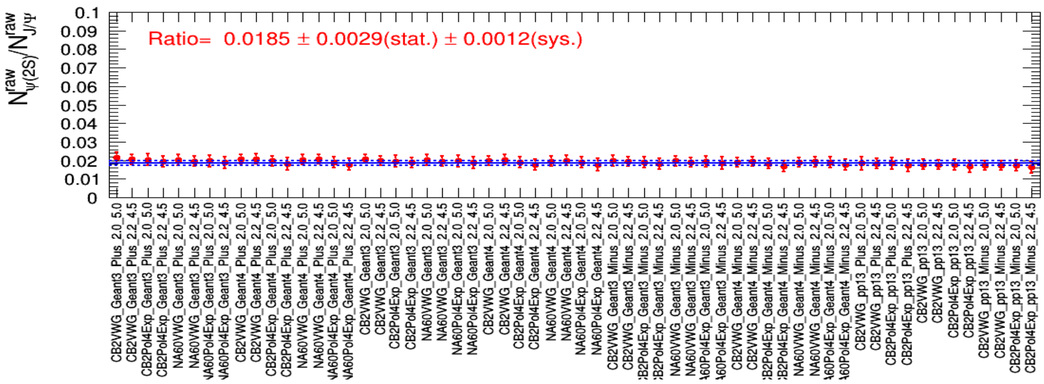

Figure 4.7: ψ(2S) to J/ψ ratio as a function of the tests performed for $3.5 < y < 3.75$.

reconstructed charmonium in the muon spectrometer to the number of generated quarkonium in the same p_{T} and y intervals obtained through MC simulations. A realistic MC simulation is done in order to replicate the detector conditions during the online data collections.

As a first step, realistic p_{T} and y distributions of charmonia are supplied as input

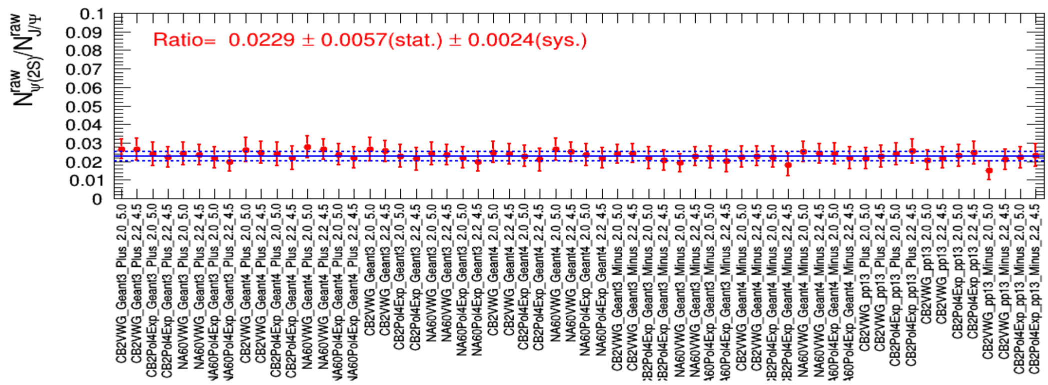

Figure 4.8: ψ(2S) to J/ψ ratio as a function of the tests performed for $2.5 < y < 2.75$.

to the simulation. These distributions are obtained from the RHIC, CDF and LHC data sets [8].

The particle transport of muons and the detector response has been simulated using GEANT3. The detector signals are finally stored as raw data, with an intermediate digitization conversion finally converting to structure similar to real data.

But these distributions do not well represent the data. In order to get a more accurate result, an iterative procedure is used to tune the charmonium input $p_{\rm T}$ and y distributions on the measured data distributions until no significant variation of the input shapes is observed.

For the ψ(2S) A.ϵ simulation, we have used the final J/ψ input $p_{\rm T}$ and y distribution as initial input shapes. Due to the low statisitics of ψ(2S) data, we could not rely on ψ(2S) data to extract proper $p_{\rm T}$ and y shapes. The A.ϵ is first calculated from this MC simulation in order to define the step 0 of the procedure. Then the J/ψ raw yields as a function of $p_{\rm T}$ and rapidity are corrected by A.$\epsilon_0(p_{\rm T})$ and by A.$\epsilon_0(y)$. The resulted data are then fitted by:

$$f(p_{\rm T}) = p_0.\frac{p_{\rm T}}{(1 + (p_{\rm T}/p_1)^{p_2})^{p_3}}, f(y) = p_4.exp^{-0.5(y/p_5)^2} \tag{4.4}$$

where p_0, p_1, p_2, p_3, p_4 and p_5 are the free parameters obtained from fitting the corrected data. Thus only these parameters are updated at each iteration. The resulting data is plotted and the deviation from the previous step is measured. When the result from nth step closely matches with the one obtained from (n-1)th iteration, the method converges.

In this case, the iterative procedure already converges after the 2nd iteration.

The A.ϵ depends on the p_{T} and y of the particle and is plotted in Fig. 4.9. From the figure, it is clear that the detector efficiency is low particularly at low p_{T} and two extreme rapidity bins. The reason is that at low-p_{T}, the bending angle is also large and either of the muon may escape the spectrometer acceptance. On the other hand, at the two extreme rapidity ranges i.e. near the edge of the detector, the glue and supporting frames in the hardware are responsible for fall of the A.ϵ.

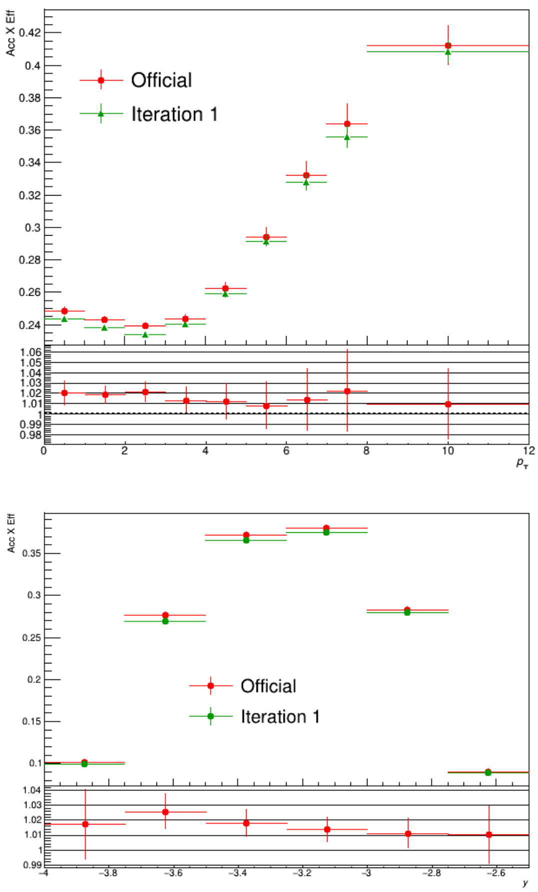

Figure 4.9: The acceptance $\times$ efficiency for ψ(2S), as a function of p_{T} (top) and y (bottom).

Systematics

The systematics have the following categories:.

Signal extraction

The final ψ(2S) yields have been obtained as the weighted average of 60 different tests. The systematic uncertainty is obtained from the RMS of the yields distribution. For the p_{T} and y integrated results, the systematic uncertainty on signal extraction is 7.2%. The systematic varies from 6-16% and 6-14% in p_{T} and y bins respectively.

Input Monte Carlo parametrization

The method of MC systematics evaluation has been described below. The systematics has two parts.

a) As we directly used the input shape from J/ψ p_{T} and y distributions for the MC, as stated before, we have evaluated the systematics on input due to this method. After each iteration, the J/ψ yield as a function of p_{T} and y are fitted with the function mentioned in section 4.3. The deviation in yield compared to the last step, is calculated till the iteration converges i.e. the deviation becomes negligible. Once the iteration converges, the newly obtained acc.ϵ is compared with the one obtained at first step. The ratio of these two A.ϵ gives the uncertainty in the A.ϵ due to the different input shapes used in MC.

(b) For the current analysis, only the above method will not be sufficient as we have used J/ψ shape as input instead of ψ(2S). To evaluate this uncertainty, the $\sigma_{\psi(2\mathrm{S})}/\sigma_{\mathrm{J}/\psi}$ ratio as a function of p_{T} (Fig. 4.10 a)) and y (Fig. 4.10 b)) has been obtained in the current analysis. Next they are fitted with 1st order polynomial function which has two free parameters. Now these two parameters are varied within their uncertainties obtained from the fit. Then all possible combinations of these parameters are considered to draw several straight lines using different colors as shown in Fig. 4.10. Each straight line gives a particular value of p_{T}-differential or y-differential cross section ratio for a particular bin. Now taking this value of the ratio from the straight line, we have calculated new A.ϵ (dividing the raw yield with this new corrected yield from the polynomial). Thus every combination of free parameters gives new set of acc.ϵ for each bin. The RMS of all these A.ϵ contribute to the second part of input MC systematics. The RMS has been plotted in Fig.4.11 a) and the calculated uncertainty in A.ϵ has been plotted as a function of y (Fig. 4.11 b)) and p_{T} (Fig. 4.11 c)). This systematics range from 0.1 to 1.6% in rapidity and 0.65 to 0.95% in p_{T} bins. The MC input systematics of J/ψ is added in quadrature to this systematics.

The different analysis steps mentioned above are presented in the following figures. The plots of the iterative methods are also shown in Fig. 4.12, 4.13, 4.14 and 4.15. While Fig. 4.12 and 4.13 show the performance of step 2 over step 1 as a function of p_{T} and y. Finally in Fig. 4.14 and 4.15, we see good agreements between step 2 and 3.

The table 4.6 lists the MC systematics obtained from the present analysis.

A summary of all the systematic uncertainties is reported in Table 4.7. As stated earlier, few systematics cancel out while taking the ratio of ψ(2S) and J/ψ yields. Only the systematics that appear in the cross section ratio are separately shown in Table 4.8.

The systematics due to B.R. is not included in the results. It is shown separately.

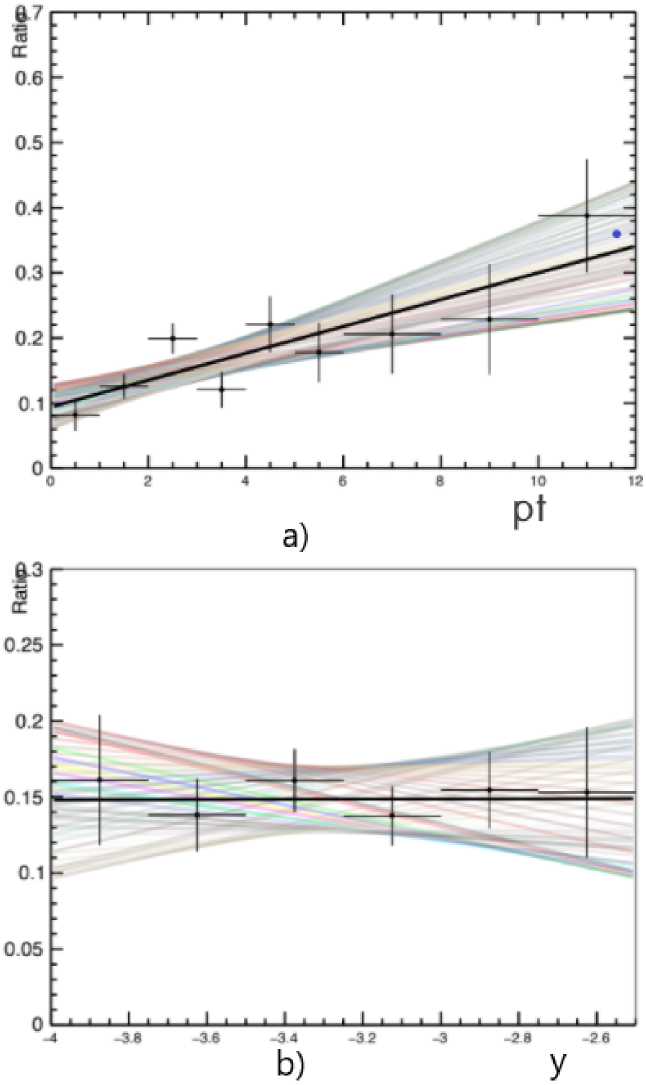

Figure 4.10: Variation of the free parameters of the fit function to the cross section ratio as a function of a) p_{T}, b) y.

Results

ψ(2S) cross section

The production cross section for inclusive ψ(2S) is calculated as:

$$\frac{d^2\sigma_{\psi(2S)}}{dp_{\mathrm{T}}dy} = \frac{N_{\psi(2S)}(\triangle y, \triangle p_{\mathrm{T}})}{L_{int} \times BR \times A.\epsilon(\triangle y, \triangle p_{\mathrm{T}}) \times \triangle y \times \triangle p_{\mathrm{T}}} \tag{4.5}$$

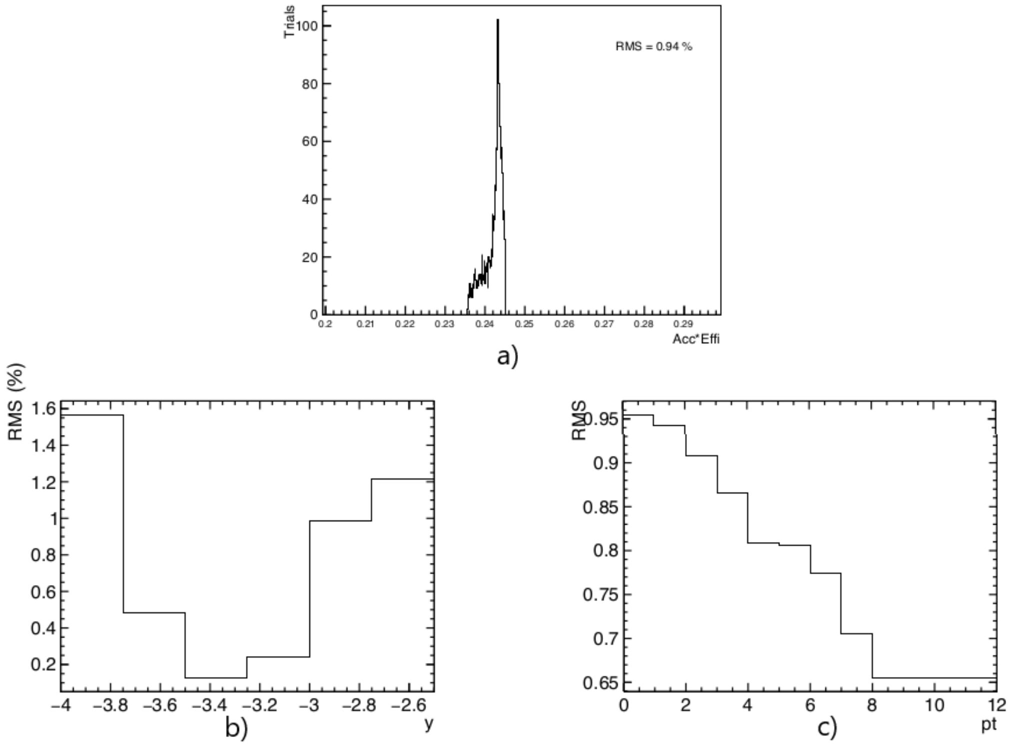

Figure 4.11: a) The RMS of acc.eff. obtained from the fit results with different parameters, b) The RMS in % as a function of y, c) The RMS in % as a function of p_{T}

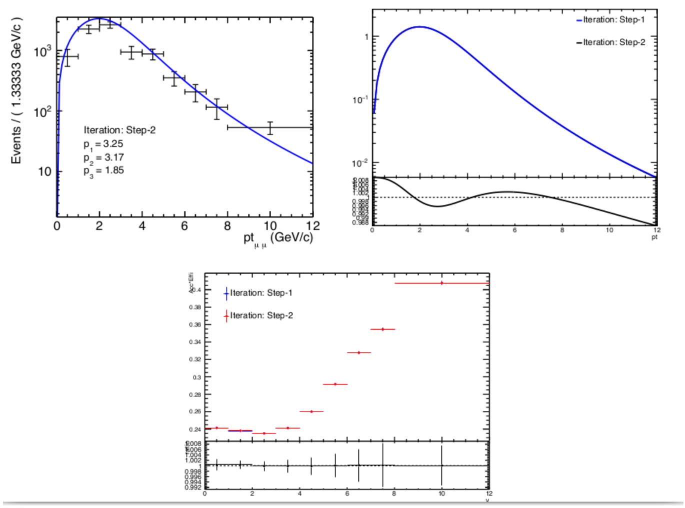

Figure 4.12: The comparison of p_{T} distribution between step 1 and 2

where $N_{\psi(2S)}(\triangle y, \triangle p_{\mathrm{T}})$ is the measured $\psi(2S)$ raw yield in a given $\triangle p_{\mathrm{T}}$ and $\triangle y$ interval. The dimuon branching ratio of $\psi(2S)$ (BR) is $0.8 \pm 0.06\%$.

The inclusive $\psi(2S)$ production cross section, integrated over $0 < p_{\mathrm{T}} < 12$ GeV/c

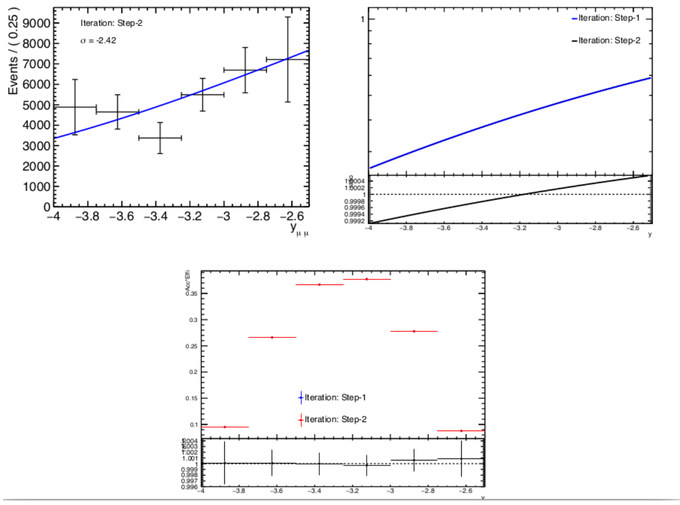

Figure 4.13: The comparison of y distribution between steps 1 and 2

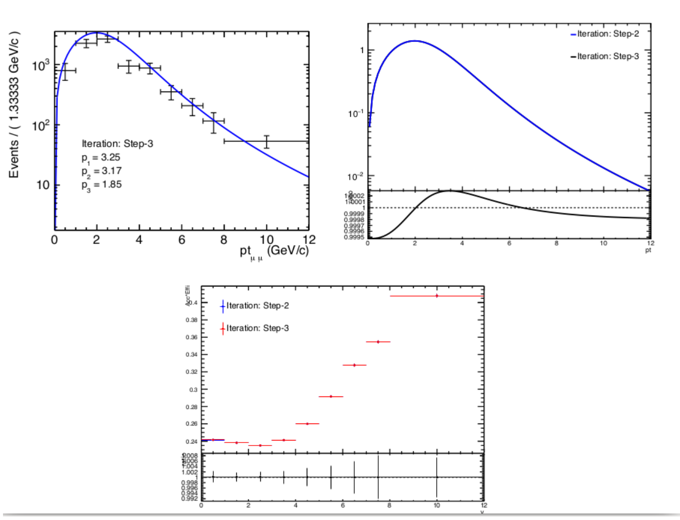

Figure 4.14: The comparison of $p_{\rm T}$ distribution between steps 2 and 3

and for $2.5 < y < 4$, is found to be $\sigma_{\psi(2S)} = 0.86 \pm 0.06$ (stat.) $\pm$ 0.10 (syst.) μb.

A significant improvement of the statistical uncertainty, about three times compared to the previous data set, is achieved. In Fig. 4.16, the first measurements of the $p_{\rm T}$ (left) and y (right) differential $\psi(2S)$ cross section for $2.5 < y < 4$ in pp collisions at $\sqrt{s} = 5.02$ TeV are shown.

The NRQCD calculations [9] match with the experimental data for $3 < p_{\rm T} < 12$ GeV/c, and the NRQCD calculation of [10] describe well the data except for the $5 < p_{\rm T} < 6$ GeV/c range, where it overestimates the data. On the other hand, the

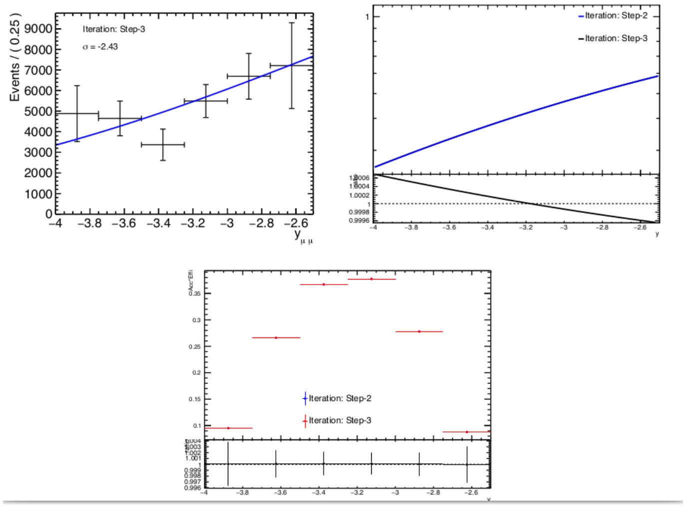

Figure 4.15: The comparison of y distribution between steps 2 and 3

Table 4.6: The MC input to systematic uncertainties, for different p_{T} and y differential bins

p_{T} (GeV/c)	sys in %
$0 < p_{\mathrm{T}} < 1$	0.95 + 2.2 (= 2.4)
$1 < p_{\mathrm{T}} < 2$	0.94 + 1.8 (= 2)
$2 < p_{\mathrm{T}} < 3$	0.90 + 1.8 (= 2)
$3 < p_{\mathrm{T}} < 4$	0.86 + 1.8 (= 2)
$4 < p_{\mathrm{T}} < 5$	0.80 + 1.7 (= 1.9)
$5 < p_{\mathrm{T}} < 6$	0.80 + 1.4 (= 1.6)
$6 < p_{\mathrm{T}} < 7$	0.77 + 1.3 (= 1.5)
$7 < p_{\mathrm{T}} < 8$	0.70 + 1.2 (= 1.4)
$8 < p_{\mathrm{T}} < 12$	0.66 + 1.2 (= 1.4)
$0 < p_{\mathrm{T}} < 12$	0.94 + 3.2 (= 3.3)
y	sys in %
$2.5 < y < 2.75$	1.2 + 4.9 (= 5)
$2.75 < y < 3.0$	0.95 + 2.4 (= 2.6)
$3.0 < y < 3.25$	0.25 + 1.6 (= 1.6)
$3.25 < y < 3.5$	0.1 + 1.4 (= 1.4)
$3.5 < y < 3.75$	0.46 + 1.7 (= 1.8)
$3.75 < y < 4.0$	1.5 + 3.0 (= 3.4)

NLO calculation of CEM [13] shows significant deviation from the data for $p_{\mathrm{T}} > 5$ GeV/c.

The NRQCD+CGC [11] and ICEM [12] models provide a good description of the $\psi(2S)$ cross section as a function of y and integrated over p_{T}, despite of the large

Table 4.7: The systematic uncertainties estimated for the present analysis

source	integrated (%)	vs p_T (%)	vs y (%)
signal extraction	7.2	5.8-15.6	5.7-13.9
trigger	2	1.4-2.2	1-2.6
tracking	2	2	2
matching	1	1	1
MC inputs	3.3	1.4-2.4	1.4-5.0
Luminosity (global)	1.8	1.8	1.8
BR (global)	7.5	7.5	7.5

Table 4.8: The systematic uncertainties for cross section ratio of ψ(2S) and J/ψ

source	integrated (%)	vs p_T (%)	vs y (%)
signal extraction	5.4	3.9-13.9	4.1-10.5
MC inputs (ψ(2S))	3.9	1.4-2.4	1.4-5.0
MC inputs (J/ψ)	3.2	1.2-2.2	1.4-4.9
BR (global)	7.5	7.5	7.5

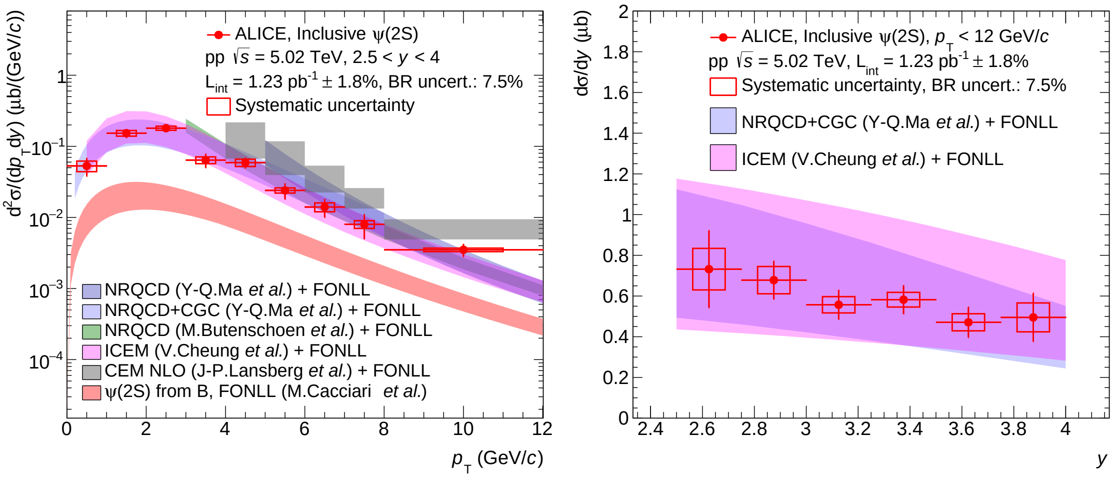

Figure 4.16: The left and right panels show the p_T and y dependence, respectively, for the ψ(2S) production cross section in pp collisions at $\sqrt{s} = 5.02$ TeV. The error bars represent the statistical uncertainties, while the boxes correspond to systematic uncertainties.
The results are compared with the calculations based on NRQCD [9–11], ICEM and NLO CEM [12, 13], and FONLL calculations [14]

uncertainties. It may be noted that, the non-prompt ψ(2S) contribution from FONLL [14] varies from about 10 to 25% as a function of p_T and y.

ψ(2S) over J/ψ cross section ratio

The ratio of inclusive ψ(2S)-to-J/ψ production cross section integrated over p_{T} and y is found to be 0.15 ± 0.01 (stat.) ± 0.02 (syst.), being consistent with the other measurements in pp collisions at $\sqrt{s} = 7$ TeV, 8 TeV and 13 TeV as shown in Fig. 4.17. The ratio has been found to be independent of the centre-of-mass energy.

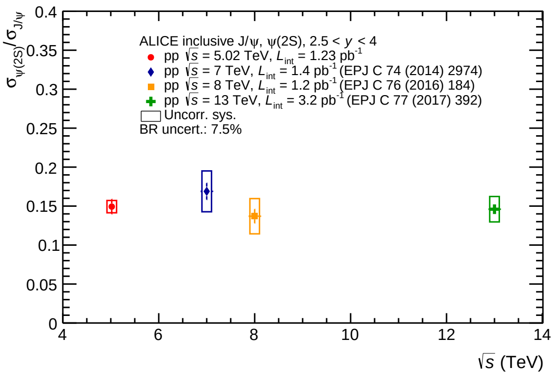

Figure 4.17: The ψ(2S)-to-J/ψ cross section ratio at various centre of mass energies.

In Fig. 4.18, the p_{T} and y dependence of the ψ(2S) over J/ψ cross-section ratio in pp collisions at $\sqrt{s} = 5.02$ TeV are shown in the top and bottom panel, respectively.

The NRQCD calculations from [9] describe well the p_{T} dependence of the cross-section ratio albeit with large uncertainties while the NRQCD result from [10] describe well the p_{T} dependence but systematically overestimates the data for $5 < p_{\mathrm{T}} < 8$ GeV/c. The NRQCD+CGC [11] model provides a good explanation of the ψ(2S) over J/ψ cross-section ratio as a function of p_{T} and y for $p_{\mathrm{T}} < 8$ GeV/c. The trend of the ψ(2S) over J/ψ cross-section ratio as a function of p_{T} and y is overestimated by the ICEM model [12] in the low p_{T} region.

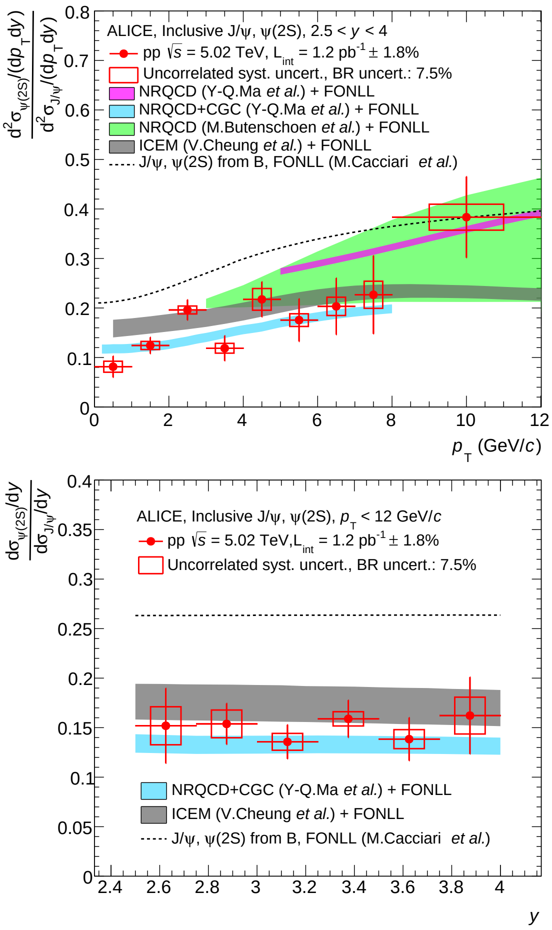

Figure 4.18: The ψ(2S)-to-J/ψ cross section ratio as a function of p_{T} (top) and rapidity (bottom) and compared with the theoretical calculations [9–12, 14].

Discussions

The inclusive cross section measurement of ψ(2S) in pp collisions at $\sqrt{s}$ = 5.02 TeV has been described in this chapter. The ψ(2S) results are in good agreement with the previous publication at the same collision energy. The first p_{T} and y differential cross section measurement of ψ(2S) has extended the scope of comparison of cross section ratio at various energies. The results are described well by the models based on CEM and NRQCD.

Bibliography

[1] J. E. Gaiser, Charmonium Spectroscopy From Radiative Decays of the J/ψ and ψ. PhD thesis, SLAC, 1982. http://www-public.slac.stanford.edu/sciDoc/docMeta.aspx?slacPubNumber=slac-r-255.html.

[2] ALICE Collaboration, "Quarkonium signal extraction in ALICE", 2015. https://cds.cern.ch/record/2060096, accessed ALICE-PUBLIC-2015-006.

[3] R. Shahoyan, J/ψ and ψ(2S) production in 450 GeV pA interactions and its dependence on the rapidity and xF. PhD thesis, Lisbon, IST, 2001. http://lss.fnal.gov/archive/other/thesis/shahoyan-ruben.pdf.

[4] Particle Data Group Collaboration, M. Tanabashi et al., "Review of Particle Physics", Phys. Rev. D98 no. 3, (2018) 030001.

[5] ALICE Collaboration, S. Acharya et al., "Energy dependence of forward-rapidity J/ψ and ψ(2S) production in pp collisions at the LHC", Eur. Phys. J. C77 no. 6, (2017) 392, arXiv:1702.00557.

[6] R. Brun et al., "GEANT3 User guide", 1987. https://cds.cern.ch/record/1119728?ln=fr, accessed CERN-DD-EE-84-01.

[7] GEANT4 Collaboration, S. Agostinelli et al., "GEANT4: A Simulation toolkit", Nucl. Instrum. Meth. A506 (2003) 250303.

[8] F. Bossu et al. “Phenomenological interpolation of the inclusive J/psi cross section to proton-proton collisions at 2.76 TeV and 5.5 TeV”, arXiv:1103.2394 [nucl-ex].

[9] Butenschoen et al., Phys. Rev. Lett. 106 (2011) 022003.

[10] Ma et al., Phys. Rev. Lett. 106 (2011) 042002.

[11] Ma et al., Phys. Rev. Lett. 113 (2014) 19.

[12] Cheung et al., Phys. Rev. D 98 (2018) 11.

[13] Lansberg et al., arxiv:2004.14345.

[14] Cacciari et al., JHEP 10 (2012).

CHAPTER 5

$\psi(2\mathrm{S})$ production studies in p–Pb collisions at $\sqrt{s_{\mathrm{NN}}} = 8.16$ TeV

In this chapter two analysis have been presented based on the data collected in p–Pb collisions at $\sqrt{s_{\mathrm{NN}}} = 8.16$ TeV. These are p_{T} and y dependence and centrality dependence of $\psi(2\mathrm{S})$ production cross-sections.

In p–Pb collisions, the rapidity in CM frame is shifted by $\pm$ 0.46 with respect to the laboratory frame. When the proton (lead) beam is directed towards the muon spectrometer, the collision is called p-Pb (Pb–p) and corresponds to the rapidity coverage of $2.03 < y < 3.53$ ($-4.46 < y < -2.96$).

We have used the latest AOD files which were pass2 for p–Pb and pass3 for Pb–p collisions.

The signal extraction, Monte Carlo simulations, evaluation of acceptance $\times$ efficiency, evaluation of pp cross section for reference, estimation of all the experimental uncertainties and evaluation of R_{pPb} have been done as a part of this thesis work.

$p_{\rm t}$ and y dependence of ψ(2S) cross-section

Motivation

A larger suppression of ψ(2S) compared to J/ψ has been observed in p–Pb collisions, especially at backward rapidity at $\sqrt{s_{\rm NN}}$ = 5.02 TeV [1–5]. However, the CNM effects are expected to affect similarly both charmonium resonances. The additional suppression for ψ(2S) is believed to be the result of the break-up of this more loosely bound state due to the collisions with the dense system of interacting particles produced in p–Pb collisions [6–8]. A similar effect was also reported, although with larger uncertainties, by the PHENIX experiment in p-Al and p-Au collisions at $\sqrt{s_{\rm NN}}$ = 0.2 TeV [9].

Recently, p–Pb collisions data at $\sqrt{s_{\rm NN}}$ = 8.16 TeV became available providing larger statistics than the last one. In this chapter, we will present the first results on inclusive ψ(2S) production in p–Pb collisions at $\sqrt{s_{\rm NN}}$ = 8.16 TeV.

Data samples

The data have been collected during the p–Pb (integrated luminosity of 8.4 nb^{-1}) and Pb–p (integrated luminosity of 12.8 nb^{-1}) at $\sqrt{s_{NN}}$ = 8.16 TeV period in November-December 2016.

Signal Extraction

The $\psi(2S)$ yields are extracted starting from the opposite sign invariant mass spectra in the range $2 < m_{\mu^+\mu^-} < 5$ GeV/c^2 and fitting them with a number of phenomenological functions which describe the signal of J/ψ and $\psi(2S)$ and the background.

The $\psi(2S)$ final yields are calculated considering the average of all the fit performed for each p_{T} and y bin and for the integrated bin and the RMS of the results of tests provides the systematic uncertainty. The different combinations used for the tests are the following:

- signal shape : extended Crystal Ball function (CB2) and "NA60" function
- background shape : Variable Width Gaussian (VWG), combination of a fourth order polynomial and an exponential function(Pol4xExp).
- fitting ranges : $2.2 < m_{\mu^+\mu^-} < 4.5$ GeV/c^2 or $2 < m_{\mu^+\mu^-} < 5$ GeV/c^2

J/ψ and $\psi(2S)$ are described by the same signal shape and $\psi(2S)$ mass and width are bounded to the J/ψ ones, which are let free in the fit. The ratio between $\psi(2S)$ and J/ψ widths is around 5% with a relative uncertainty of 5% which has been estimated from the fit of pp $\sqrt{s} = 13$ TeV high statistics data. To estimate the effect of this uncertainty on signal extraction, fits have been performed varying the scale factor ± 5 %. The systematics induced an additional systematic of 5% in the raw numbers. To consider that, an uncorrelated syatematics of 5% has been added to all the bins. This method allows to include all possible variations due to scaling of the width independent of fitting methods.

Fig. 5.1 shows the plots of the MC simulated invariant mass spectra for J/ψ and $\psi(2S)$ fitted with a CB2 in order to obtain the width of the two resonances and evaluate their ratio.

Because of the small number of $\psi(2S)$ (approximately 1 $\psi(2S)$ for every 100 J/ψ) the yields are sensitive to the choice of backgrounds and tails, which are described below :

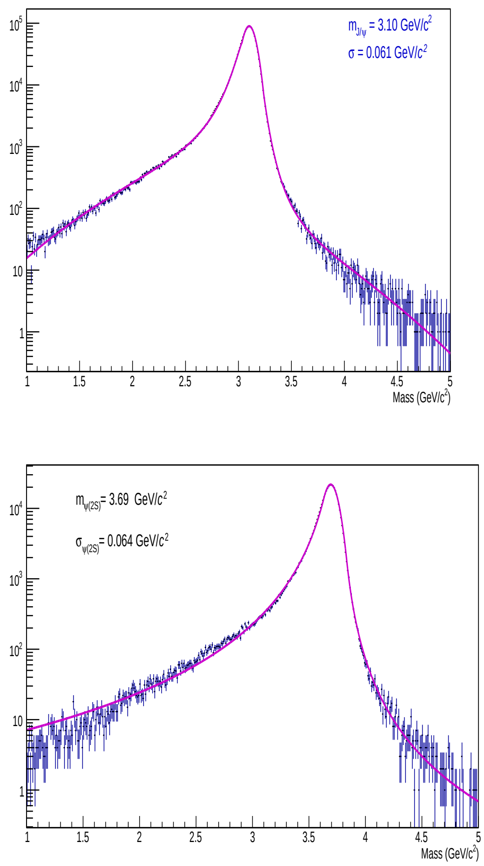

Figure 5.1: Fits to the J/ψ (top) and ψ(2S) (bottom) MC spectra at 8.16 TeV using an extended Crystal Ball function (CB2) with all parameters free.

– tails tuned on p-Pb MC invariant mass spectrum at $\sqrt{s_{NN}} = 8.16$ TeV (CB2 and NA60)

– tails fixed to the values extracted directly from data in pp collisions at $\sqrt{s_{NN}} = 8$ TeV (CB2 only)

– tails fixed to the values extracted directly from data in p-Pb collisions at $\sqrt{s_{NN}} = 8.16$ TeV (CB2 only)

p_{T} and y integrated ψ(2S) yield

The signal extraction procedure is performed using 16 different combinations of the signal, the background and the tail: 2 signal functions, 2 backgrounds shapes, 2 invariant mass fitting ranges and 3 sets of tails for the CB2. The plots with the results of all the tests is shown in Fig. 5.2 and Fig. 5.3. The values are reported in Table 5.1 and 5.2.

In Fig. 5.4 two examples of fit for the integrated invariant mass spectrum are presented.

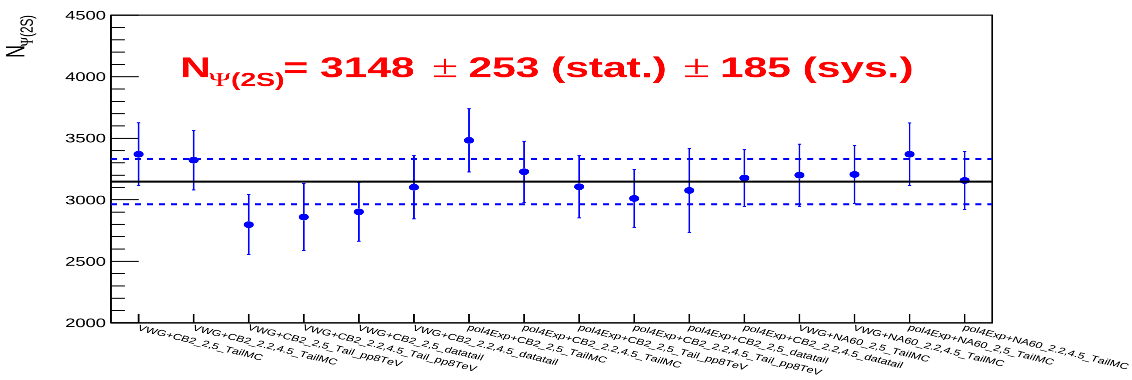

Figure 5.2: The ψ(2S) raw yields as a function of the tests performed for the p-Pb period.

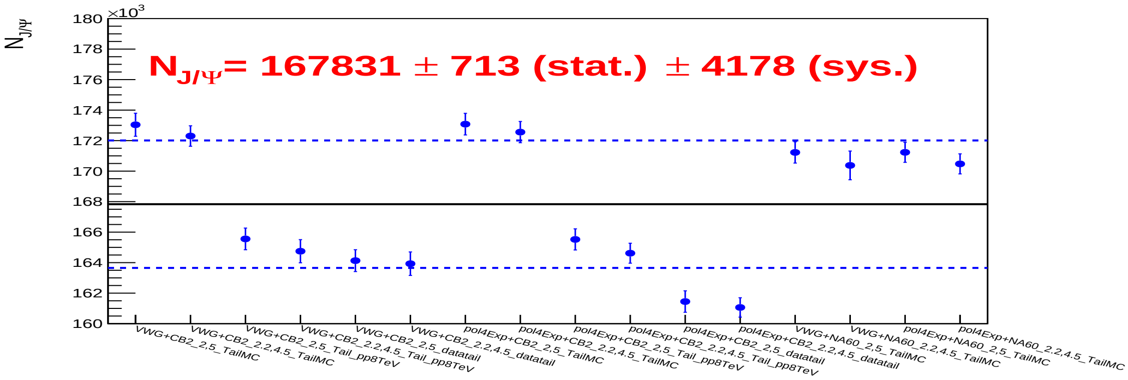

Figure 5.3: The J/ψ raw yields as a function of the tests performed for the p-Pb period.

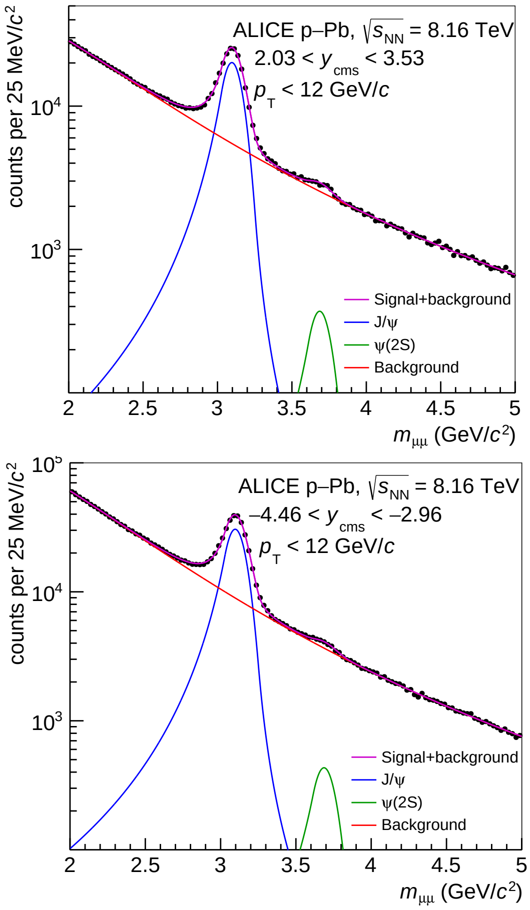

Figure 5.4: Typical fits to the $p_{\rm T}$ and y integrated mass spectrum for the p–Pb (left) and Pb–p (right) period. For these two canvas the signal function is CB2, the background shape is VWG.

Table 5.1: Number of ψ(2S) integrated over $p_{\rm T}$ and y for the p-Pb and Pb-p period. The first uncertainty is statistical, second one is the systematic one.

Period	$N_{\psi(2S)}$
p-Pb	3148 ± 253 (8.0%) ± 185 (5.9%)
Pb-p	3595 ± 283 (7.9%) ± 321 (8.9%)

Table 5.2: Number of J/ψ integrated over $p_{\rm T}$ and y for the p-Pb and Pb-p period. The first uncertainty is statistical, second one is the systematic one.

Period	$N_{J/\psi}$
p-Pb	167831 ± 713 (0.4%) ± 4178 (2.5%)
Pb-p	252355 ± 905 (0.4%) ± 7123 (2.8%)

$p_{\rm T}$ and y differential ψ(2S) yield

The signal extraction procedure, followed for the estimation of differential in $p_{\rm T}$ and y, is the same as the integrated one with some differences in the choice of the mass ranges used in the fit. The ψ(2S) yields are evaluated in 5 $p_{\rm T}$ bins from 0 to 12 GeV/c and 2 y bins from 2.03 to 3.53 (p-Pb) and -4.46 to -2.96 (Pb-p) and fits of these spectra are more sensitive to the background shapes and to the fitting ranges. These are shown in Fig. 5.5 and 5.6 for the bin $0 < p_{\rm T} < 2$ in p–Pb and Pb–p periods, respectively. The ψ(2S) and J/ψ raw yields in $p_{\rm T}$ bins are reported in Table 5.3 and 5.4 in p–Pb collisions, respectively. In Table 5.5 and 5.6, the $p_{\rm T}$-differential raw ψ(2S) and J/ψ yields are reported in Pb–p collisions, respectively. The ψ(2S) and J/ψ raw yields in y bins are reported in Table 5.7 and 5.8 in p–Pb collisions, respectively. In Table 5.9 and 5.10, the y-differential raw ψ(2S) and J/ψ yields are reported in Pb–p collisions, respectively.

Acceptance × efficiency

The acceptance × efficiency is evaluated using the MC simulation. The up-to-date alignment and misalignment files have been used, together with efficiency maps

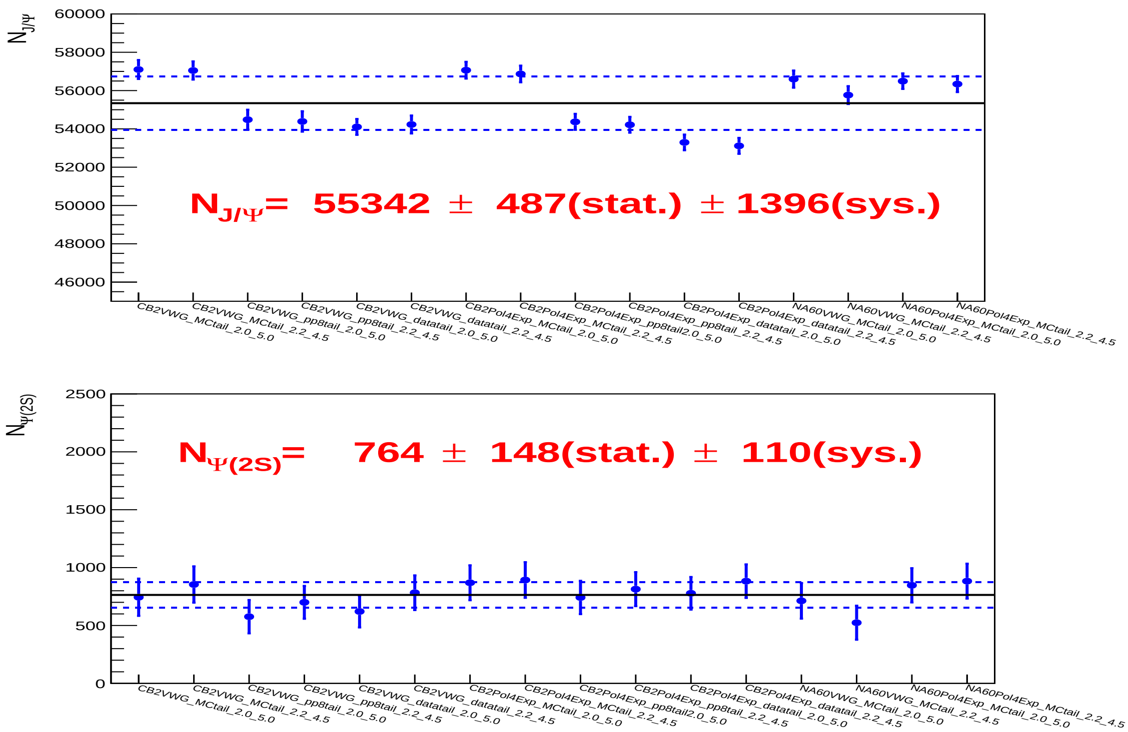

Figure 5.5: The J/ψ and the ψ(2S) raw yields as a function of the tests performed in for $0 < p_{\mathrm{T}} < 2$ GeV/c in p–Pb period.

Table 5.3: The number of $\psi(2S)$ for the p_{T} bins for the p-Pb period. The first uncertainty is statistical and the second one is the systematic one. The third uncertainty is due to the scaling of $\sigma_{\psi(2\mathrm{S})}$ which amounts to 5 %.

p_{T} (GeV/c)	$N_{\psi(2S)}$
$0 < p_{\mathrm{T}} < 2$	764 ± 148 (19.4%) ± 110 (14.4%) ± 38
$2 < p_{\mathrm{T}} < 3$	531 ± 112 (21%) ± 60 (11.3%) ± 26
$3 < p_{\mathrm{T}} < 5$	1062 ± 126 (11.9%) ± 67 (6.3%) ± 53
$5 < p_{\mathrm{T}} < 8$	570 ± 76 (13.3%) ± 51 (8.9%) ± 28
$8 < p_{\mathrm{T}} < 12$	150 ± 39 (26%) ± 29 (19.3%) ± 7

Table 5.4: The number of J/ψ for different p_{T} bins for the p-Pb period. The first uncertainty is statistical and the second one is the systematic one.

p_{T} (GeV/c)	$N_{J/\psi}$
$0 < p_{\mathrm{T}} < 2$	55342 ± 487 (0.9%) ± 1396 (2.5%)
$2 < p_{\mathrm{T}} < 3$	35385 ± 310 (0.9%) ± 922 (2.6%)
$3 < p_{\mathrm{T}} < 5$	44470 ± 338 (0.8%) ± 1108 (2.5%)
$5 < p_{\mathrm{T}} < 8$	24007 ± 227 (0.9%) ± 581 (2.4%)
$8 < p_{\mathrm{T}} < 12$	6827 ± 122 (1.8%) ± 171 (2.5%)

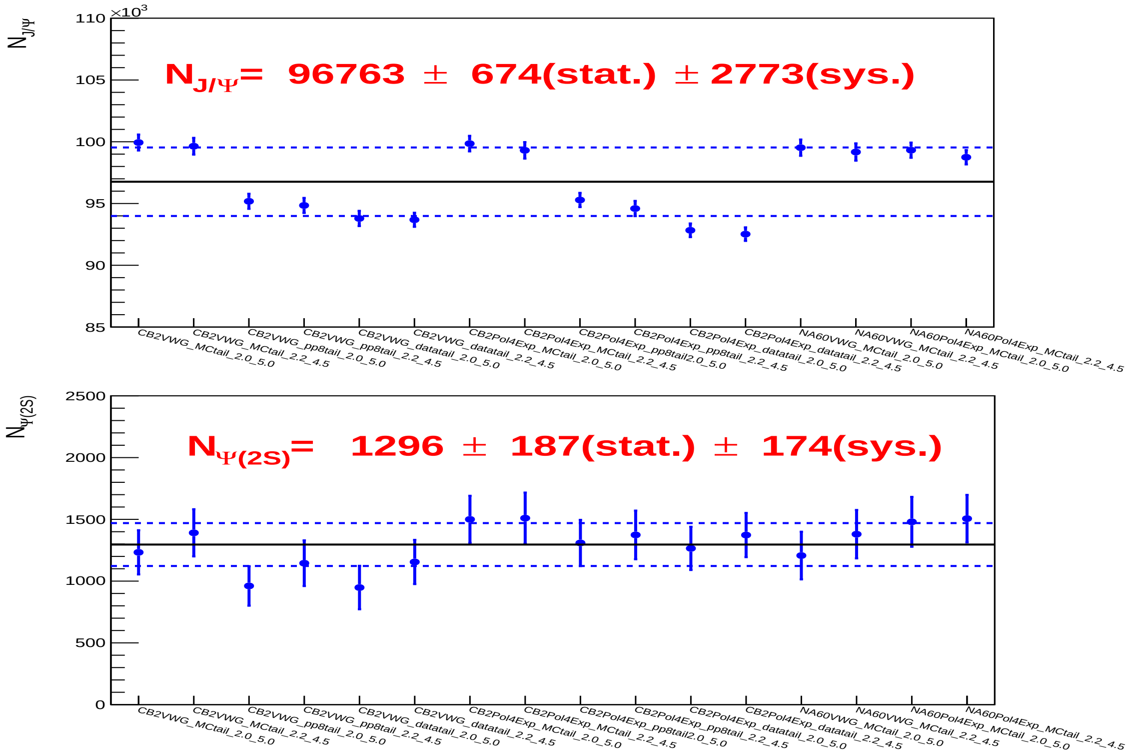

Figure 5.6: The J/ψ and the ψ(2S) raw yields as a function of the tests performed for $0 < p_{\mathrm{T}} < 2$ GeV/c in Pb-p period.

Table 5.5: The number of ψ(2S)) for different p_{T} bins for the Pb-p period. The first uncertainty is statistical and the second one is the systematic one. The third uncertainty is due to the scaling of $\sigma_{\psi(2\mathrm{S})}$ which amounts to 5 %.

p_{T} (GeV/c)	$N_{\psi(2S)}$
$0 < p_{\mathrm{T}} < 2$	1296 ± 187 (14%) ± 174 (13%) ± 21
$2 < p_{\mathrm{T}} < 3$	584 ± 141 (24%) ± 59 (10%) ± 29
$3 < p_{\mathrm{T}} < 5$	1101 ± 146 (13%) ± 84 (8%) ± 55
$5 < p_{\mathrm{T}} < 8$	507 ± 82 (16%) ± 96 (19%) ± 25
$8 < p_{\mathrm{T}} < 12$	131 ± 40 (30%) ± 32 (24%) ± 6

Table 5.6: The number of J/ψ for different p_{T} bins for the Pb-p period. The first uncertainty is statistical and the second one is the systematic one.

p_{T} (GeV/c)	$N_{\mathrm{J}/\psi}$
$0 < p_{\mathrm{T}} < 2$	96763 ± 674 (0.7%) ± 2773 (2.9%)
$2 < p_{\mathrm{T}} < 3$	57271 ± 414 (0.7%) ± 1623 (2.8%)
$3 < p_{\mathrm{T}} < 5$	63198 ± 403 (0.6%) ± 1869 (2.9%)
$5 < p_{\mathrm{T}} < 8$	27831 ± 233 (0.8%) ± 817 (2.9%)
$8 < p_{\mathrm{T}} < 12$	6090 ± 105 (1.7%) ± 191 (3.1%)

Table 5.7: The number of $\psi(2S)$ for different y bins for the p-Pb period. First uncertainty is statistical the second one is the systematic on the signal extraction. The third uncertainty is due to the scaling of $\sigma_{\psi(2\mathrm{S})}$ which amounts to 5 %

y	$N_{\psi(2S)}$
$2.03 < y < 2.78$	1663 ± 189 (11%) ± 192 (11%) ± 83
$2.78 < y < 3.53$	1479 ± 163 (11%) ± 109 (7%) ± 73

Table 5.8: Number of J/ψ for the y bins for the p-Pb period. First uncertainty is statistical the second one is the systematic on the signal extraction.

y	$N_{\mathrm{J}/\psi}$
$2.03 < y < 2.78$	91844 ± 736 (0.8%) ± 2351 (2.6%)
$2.78 < y < 3.53$	76233 ± 472 (0.6%) ± 1863 (2.4%)

Table 5.9: Number of $\psi(2S)$ for the y bins for the Pb-p period. First uncertainty is statistical the second one is the systematic on the signal extraction. The third uncertainty is due to $\sigma_{\psi(2\mathrm{S})}$ syst which amounts to 5 %

y	$N_{\psi(2S)}$
$-3.71 < y < -2.96$	1921 ± 227 (12%) ± 216 (11%) ± 96
$-4.46 < y < -3.71$	1645 ± 167 (10%) ± 163 (10%) ± 82

Table 5.10: Number of J/ψ for the y bins for the Pb-p period. First uncertainty is statistical the second one is the systematic on the signal extraction.

y	$N_{\mathrm{J}/\psi}$
$-3.71 < y < -2.96$	142446 ± 679 (0.5%) ± 4164 (2.9%)
$-4.46 < y < -3.71$	110087 ± 533 (0.5%) ± 3161 (2.9%)

stored in the OCDB. The MC simulation has been performed separately for each run, in order to correctly reproduce the detectors conditions during the data taking. The number of simulated ψ(2S) in each run is proportional to the number of collected CMUL7 triggers.

The p_{T} and y input shapes used for simulation of ψ(2S) are the ones tuned on p–Pb data at $\sqrt{s} = 8.16$ TeV for J/ψ. The reconstructed spectra have been fitted with both CB2 and NA60 function to get the acceptance efficiency and extract the tail parameters which has been used for fitting the data. Fig 5.7 shows the run by run acceptance $\times$ efficiency for ψ(2S) in p–Pb and Pb–p periods. The acceptance $\times$

efficiency is constant as a function time in p–Pb period and is 0.2802 ± 0.0024 on average. The acceptance $\times$ efficiency in Pbp period has fluctuations as a function of time due to the HV trips in the overlapping regions of chamber-03 and chamber-04 and it has lowered the value to 0.2499 ± 0.0017.

The pp reference

The evaluation of the proton-proton reference for ψ(2S) at $\sqrt{s_{\mathrm{NN}}} = 8.16$ TeV is performed through the study of the single ratio $\sigma_{\psi(2\mathrm{S})}/\sigma_{\mathrm{J}/\psi}$. Two possibilities has been investigated :

An interpolation in $\sqrt{s}$ is performed, starting from the ratio $\sigma_{\psi(2\mathrm{S})}/\sigma_{\mathrm{J}/\psi}$ in pp collisions published by the ALICE experiment at different center of mass energies, with a set of appropriate functions to obtain the value at $\sqrt{s} = 8.16$ TeV

$\sigma_{\psi(2\mathrm{S})}/\sigma_{\mathrm{J}/\psi}$: interpolation vs $\sqrt{s}$

A short summary of the systematics considered in the interpolation process is given below:

- $\sqrt{s}$ =5 TeV $\rightarrow$ only the integrated spectrum is considered and the systematic uncertainty is given by the the sum in quadrature of the relative uncertainties on signal extraction and MC input (the whole contribution is around 9%);

- $\sqrt{s}$ =7 TeV $\rightarrow$ the systematics on the signal extraction and on MC input are considered, while the one on $BR_{\psi(2\mathrm{S})}$ is not included in the ratio reported in the article (both integrated and differential) [10].

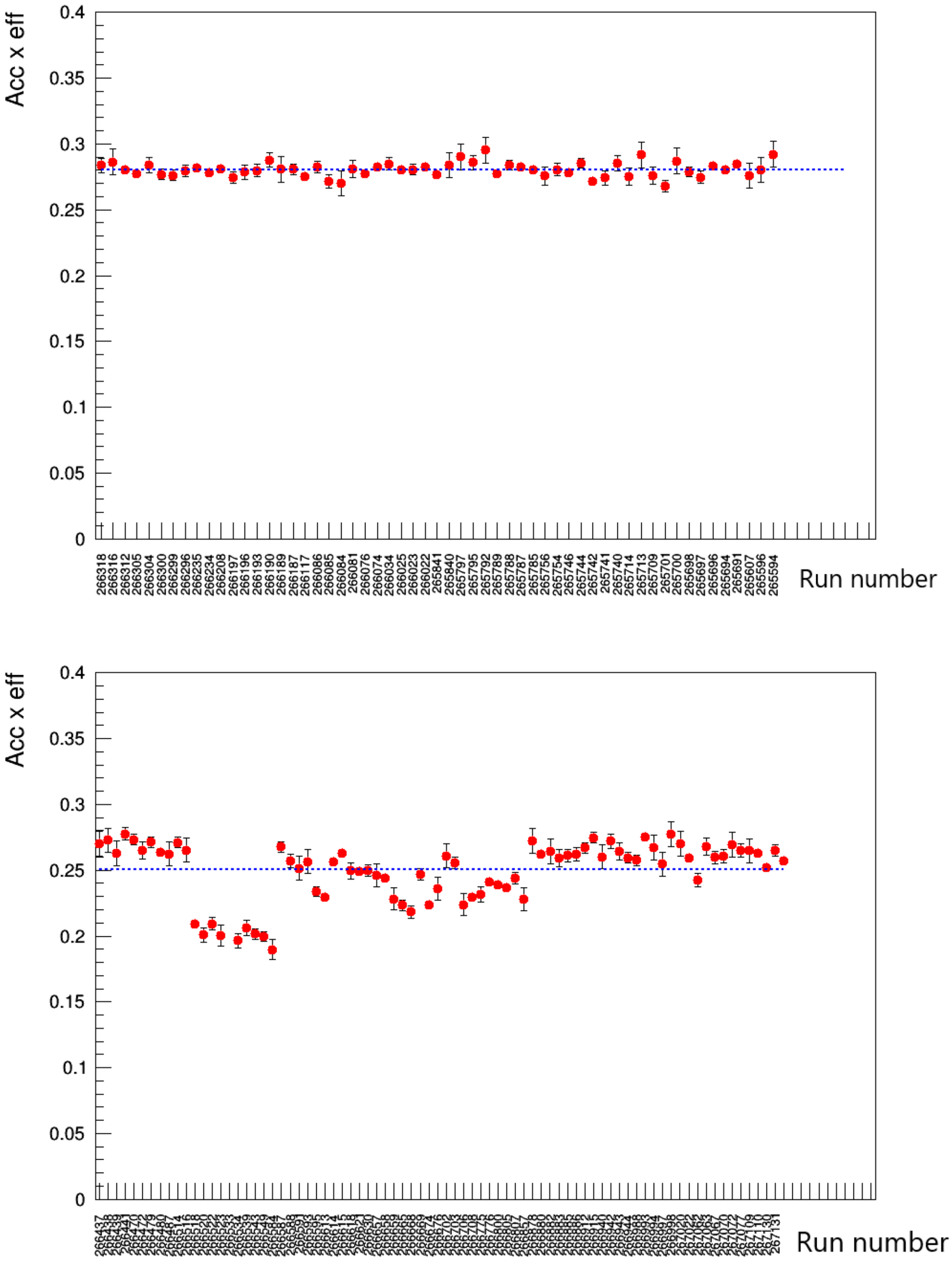

Figure 5.7: The acceptance × efficiency for $\psi(2S)$, integrated over y and $p_{\rm T}$, shown as a function of time (run number) for the period LHC16r (top) and LHC16s (bottom). The blue dashed line represents the average acceptance × efficiency.

– $\sqrt{s}$ =8 TeV → the systematics on the signal extraction and the MC input are considered, while the one on $BR_{\psi(2S)}$ is included only in the integrated spectrum [11].

– $\sqrt{s}$ =13 TeV $\rightarrow$only the systematics on signal extraction and MC input are considered, while the one on $BR_{\psi(2S)}$ is provided separately both in the integrated and in the differential spectra [12].

The ratio $\sigma_{\psi(2S)}/\sigma_{J/\psi}$ shows a negligible energy dependence, so the interpolation is performed using a constant function and, in order to verify the hypothesis of independence from $\sqrt{s}$, data are also fitted with a linear one. These are shown in Fig. 5.8 for integrated $p_{\rm T}$ and y.

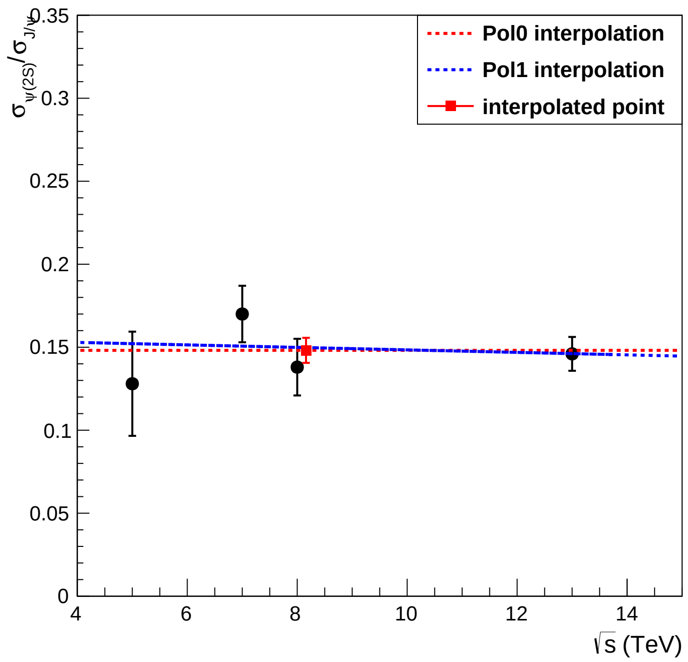

Figure 5.8: The interpolation of the ratio of ψ(2S) and J/ψ integrated cross sections with a constant (red dashed line) and a linear function (blue dashed line).

In Fig. 5.9 and 5.10, the comparisons between experimental ratio and the interpolated one as functions of $p_{\rm T}$ and y are reported.

The shape of the ratio is not flat as function of rapidity. To quantify this deviation the $d\sigma/dy$ distribution of J/ψ is studied and compared with the ψ(2S) distribution obtained from the fit of the J/ψ experimental points with a Gaussian function and

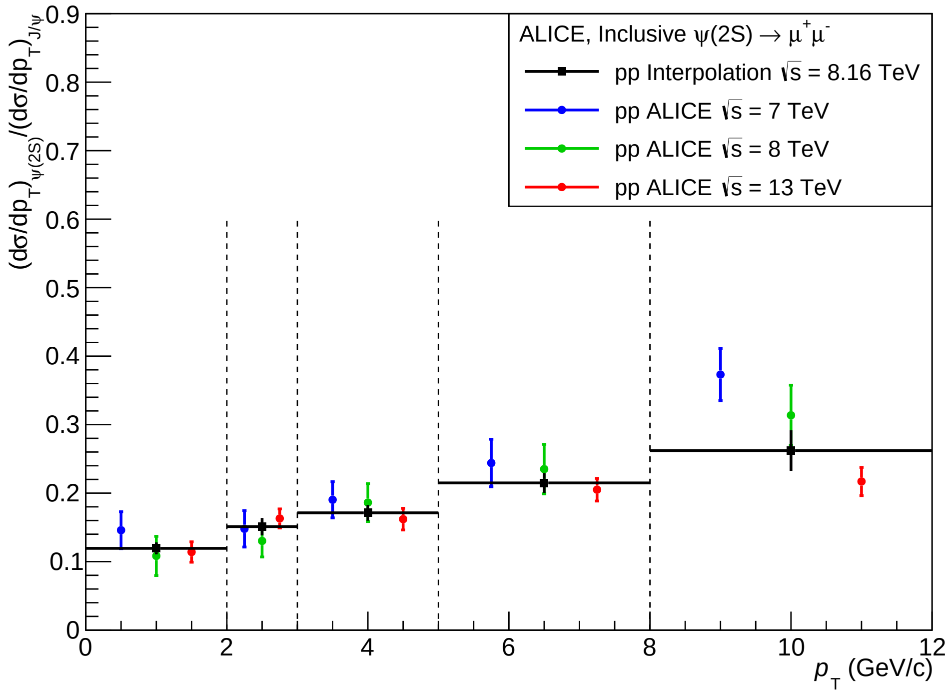

Figure 5.9: The comparison between $(d\sigma/dp_{\rm T})_{\psi(2S)}/(d\sigma/dp_{\rm T})_{J/\psi}$ as a function of $p_{\rm T}$ using the interpolation in $\sqrt{s}$ and ratios calculated using measured differential cross sections at $\sqrt{s}$ = 7, 8 and 13 TeV.

transforming its width as follows :

$$\frac{y_{max}^{\psi(2S)}}{y_{max}^{J/\psi}} = \log(\frac{\sqrt{s}}{m_{\psi(2S)}})/\log(\frac{\sqrt{s}}{m_{J/\psi}}) \tag{5.1}$$

$$\sigma_{\psi(2S)} = \sigma_{J/\psi}^{FIT} * \frac{y_{max}^{\psi(2S)}}{y_{max}^{J/\psi}} \tag{5.2}$$

In this way the dashed blue line is obtained and the point-to-point ratio between the two distributions is calculated (bottom plot in Fig. 5.11. This plot shows that there is a variation in the ratio versus rapidity, but it's quite small.

In order to quantify this systematics the ratio between the integrals of the two

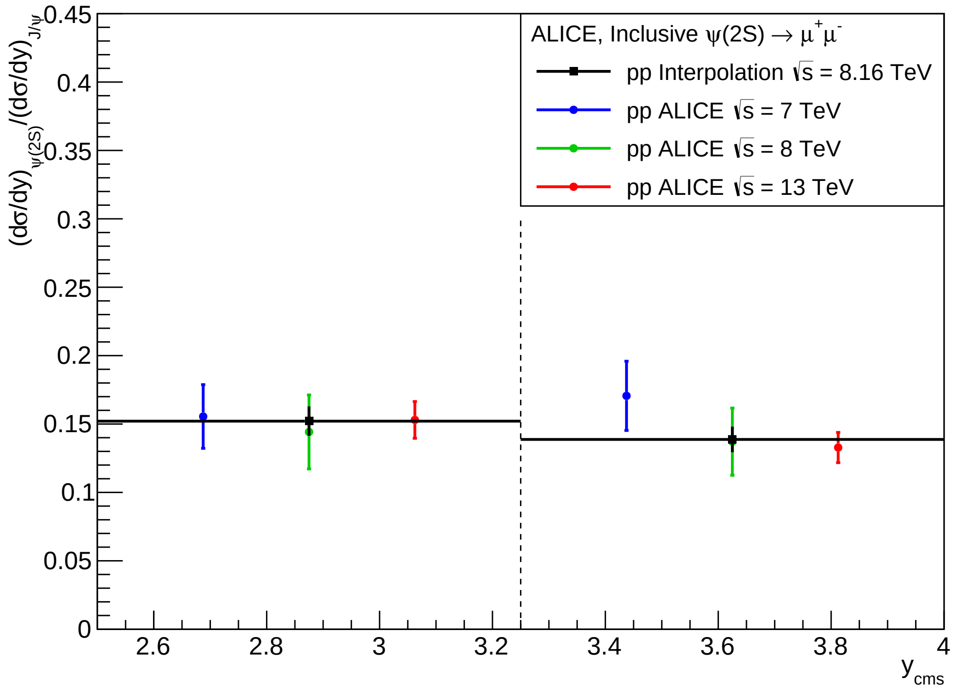

Figure 5.10: The comparison between $(d\sigma/dy)_{\psi(2\mathrm{S})}/(d\sigma/dy)_{\mathrm{J}/\psi}$ as a function of y using the interpolation in $\sqrt{s}$ and ratios calculated using experimental differential cross sections at $\sqrt{s}$ = 7, 8 and 13 TeV.

Gaussian functions for ψ(2S) and J/ψ have been normalized to the integrated value.

$$f = (\psi(2\mathrm{S})/J/\psi)_{a<y<b} = \frac{\int_a^b (e^{\frac{(x-\mu)^2}{2*\sigma}})_{\psi(2\mathrm{S})} / \int_a^b (e^{\frac{(x-\mu)^2}{2*\sigma}})_{\mathrm{J}/\psi}}{\int_{2.5}^{4.0} (e^{\frac{(x-\mu)^2}{2*\sigma}})_{\psi(2\mathrm{S})} / \int_{2.5}^{4.0} (e^{\frac{(x-\mu)^2}{2*\sigma}})_{\mathrm{J}/\psi}} * (\frac{\sigma_{\psi(2\mathrm{S})}}{\sigma_{\mathrm{J}/\psi}})^{interpolation}_{2.5-4.0} \tag{5.3}$$

where a and b are the ranges of p-Pb ($2.03 < y < 3.53$) and Pb-p ($-4.46 < y < -2.96$).

The hypothesis that the ratio as a function of rapidity is constant can be written as :

$$g = (\psi(2\mathrm{S})/J/\psi)_{2.5<y<4.0} = (\frac{\sigma_{\psi(2\mathrm{S})}}{\sigma_{\mathrm{J}/\psi}})^{interpolation}_{2.5-4.0} \tag{5.4}$$

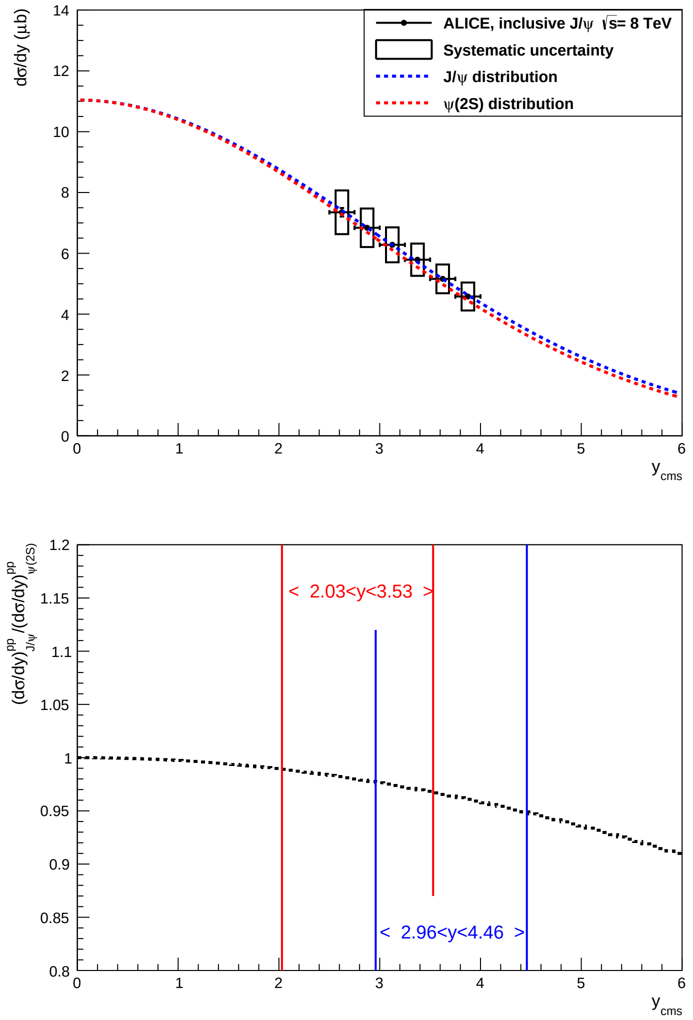

Figure 5.11: (upper panel) ALICE $(d\sigma/dy)_{\mathrm{J}/\psi}$ at $\sqrt{s} = 8$ TeV and the result of the fit performed with a gaussian function (red dashed line). The ψ(2S) is obtained from the J/ψ through a suitable transformation (blue dashed line). (bottom panel) The ratio between J/ψ and ψ(2S) distributions, the ranges for p–Pb and Pb–p analysis are depicted by coloured lines.

The relative difference between the two hypothesis can be computed as :

$$(\frac{f-g}{g})_{2.03<y<3.53} = 1.007 - 1 = +0.07 \sim 1\% \tag{5.5}$$

$$(\frac{f-g}{g})_{2.96<y<4.46} = 0.992 - 1 = -0.08 \sim 1\% \tag{5.6}$$

The calculation shows that the contribution of this variation in y is smaller than

1% both in p–Pb and Pb–p and this contribution has been added as a systematic on the ratio of the references.

pp reference calculation from Theory

An extra systematic has been added to avoid possible bias in interpolation results. The theoretical results are taken from [13], [14]. The difference in the central value is used as a systematic added in quadrature with other systematic uncertainties. The theoretical values are given in Table 5.11.

Table 5.11: The ψ(2S)/J/ψ ratio obtained from theory in the integrated and differential in $p_{\rm T}$ and y bins.

	ψ(2S)/J/ψ
Integrated	0.146 ± 0.008
$2.50 < y < 3.25$	0.147 ± 0.010
$3.25 < y < 4.00$	0.133 ± 0.009
$0 < p_{\rm T} < 2$	0.115 ± 0.008
$2 < p_{\rm T} < 3$	0.148 ± 0.012
$3 < p_{\rm T} < 5$	0.168 ± 0.011
$5 < p_{\rm T} < 8$	0.210 ± 0.014
$8 < p_{\rm T} < 12$	0.263 ± 0.030

Estimation of systematic uncertainties

A summary of all the systematic uncertainties is reported in Table 5.12.

Signal extraction

For the $p_{\rm T}$ and y integrated results, the systematic uncertainty on signal extraction is 8% and 12%, whereas it varies from 6.3 - 19.3% and 8 - 24% in $p_{\rm T}$ and y bins in p–Pb and Pb–p, respectively. An additional systematic of 5% has been added in all the bins to take into account the possible bias on fixing the width.

Input Monte Carlo parametrization

The Monte Carlo systematics have been evaluated in two steps.

The MC simulation is evaluated performing an alternative MC for the ψ(2S), using as input shapes those which were tuned on the J/ψ data in p–Pb at 8 TeV. The difference between this MC and the default one provides the systematic on the MC input. A further check has also been done which verified that the usage of a flat y distribution would have given very similar systematics.

The other contribution due to the uncertainties on the data points has also been considered by extracting alternative input shapes while allowing the points to vary within the data uncertainties. The new $A \times \epsilon$ gives a small difference at the per mille level with respect to the one already obtained in the first step.

A systematic uncertainty of 3% and 1.5% has been evaluated for in p–Pb and Pb–p periods, respectively. In p_{T} and y bins, the systematic uncertainty ranges from 0.3-4% and 0.01-4% in p–Pb and Pb–p, respectively.

pp reference

The contribution of systematics from pp reference has two parts: uncorrelated over p_{T} and y bins and correlated one. Both the systematics are same for p–Pb and Pb–p period. The uncertainty coming from the interpolation of ψ(2S)/J/ψ ratio in pp is considered as correlated over bins. The systematics of 1% is taken to be global systematics. The uncorrelated systematics are added to the systematics in the calculation of R_{pPb} later in section 6.3. The systematic is due to the uncertainty on the J/ψ cross section interpolated at pp 8.16 TeV has been considered. Another systematic calculated from theory, as stated before, is also added as bin to bin uncorrelated. This systematic has very negligible contribution.

Tracking efficiency

A 1% and 2% correlated uncertainty on the tracking efficiency is applied for p–Pb and Pb–p, respectively. The value of this systematic uncertainty is independent on the $p_{\rm T}$ or y bin and is considered as bin-to-bin correlated. There were multiple HV trips in the tracking chambers during the data taking in Pb–p collisions resulting in higher value of the tracking systematics.

Trigger efficiency

The $p_{\rm T}$ and y integrated trigger uncertainty amounts to 2.4% and 2.9% in p-Pb and Pb-p respectively. As a function of $p_{\rm T}$ and y these uncertainties range between 2 and 4%. A 1% uncertainty is added, to take into account the intrinsic chamber efficiency. This systematic on trigger efficiency is considered as uncorrelated between p-Pb and Pb-p.

Matching efficiency

An uncorrelated contribution to the systematic uncertainty of 1% is considered. This systematics has been estimated by observing the difference in matching between tracks reconstructed by tracking chambers and trigger chambers by varying χ^2 cuts in simulations.

Results

The ψ(2S) cross section is calculated as follows:

$$\sigma_{\rm pPb}^{\psi(2S)} = \frac{N_{\psi(2S)}^{\rm corr}}{L_{\rm int} \cdot B.R._{\psi(2S)\rightarrow\mu\mu}} \tag{5.7}$$

Table 5.12: The systematic uncertainties for both p-Pb and Pb-p periods as estimated from the present analysis

source	p-Pb (%)	Pb-p (%)
signal extraction	6 (6-19) +5	9 (8-24) +5
trigger	2.6 (1-5)	3.1 (1-6)
tracking (global)	1	2
matching (global)	1	1
MC inputs	3 (0.3-5)	1.5 (0.01-4)
pp reference	7.2 (1.1-4.4) + 6 (6-13) + 1(0.2-2.2)	7.3 (1.1-4.5) + 6 (6-13) + 1(0.2-2.2)
pp reference (global)	1	1

where, $N^{\mathrm{corr}}_{\psi(2S)}$ is the number of ψ(2S) corrected by A.ϵ, B.R.(ψ(2S) $\rightarrow \mu\mu$) = (0.78 $\pm$ 0.09)% is the branching ratio for ψ(2S) to dimuon decay, L_{int} is the integrated luminosity.

The measured inclusive ψ(2S) production cross sections for p–Pb collisions at $\sqrt{s_{\mathrm{NN}}}$ = 8.16 TeV, times the branching ratio to dimuon pairs and integrated over $p_{\mathrm{T}} < 12$ GeV/c are found to be:

$$\mathrm{B.R.}_{\psi(2S)\rightarrow\mu^+\mu^-} \cdot \sigma^{\psi(2S)}_{\mathrm{pPb}}(2.03 < y_{\mathrm{cms}} < 3.53) = 1.337 \pm 0.108 \pm 0.121 \pm 0.007\,\mu\mathrm{b}$$

$$\mathrm{B.R.}_{\psi(2S)\rightarrow\mu^+\mu^-} \cdot \sigma^{\psi(2S)}_{\mathrm{Pbp}}(-4.46 < y_{\mathrm{cms}} < -2.96) = 1.124 \pm 0.089 \pm 0.126 \pm 0.008\,\mu\mathrm{b}$$

where the first uncertainty is statistical, the second and third are uncorrelated and correlated systematic, respectively. The results on differential ψ(2S) cross sections are determined as a function of y_{cms} (with the forward and backward intervals separated in two sub-intervals) and p_{T} are shown in Figs. 5.12 and 5.13, respectively. In addition, the reference pp cross section evaluated from the interpolation, scaled by A_{Pb} is also plotted as a band.

In Fig. 5.14, the p_{T}-integrated cross section ratio of ψ(2S) and J/ψ is shown for the two rapidity intervals. The result is compared to the corresponding pp result at the same collision energy, obtained through the interpolation procedure explained

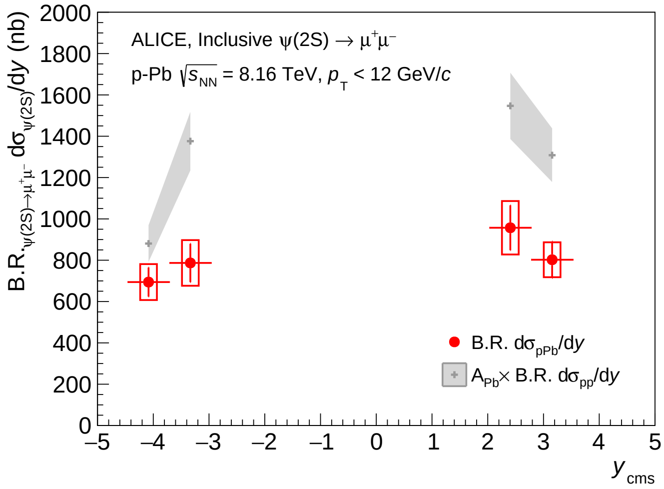

Figure 5.12: The differential cross section times branching ratio (B.R.$_{\psi(2S)\to\mu^+\mu^-}$d$\sigma^{\psi(2S)}$/dy) for $p_{\rm T}$ < 12 GeV/c. The error bars represent the statistical uncertainties, while the boxes correspond to total systematic uncertainties. The latter are uncorrelated among the points, except for a very small correlated uncertainty (0.5% and 0.7% for the forward and backward $y_{\rm cms}$ samples, respectively). The grey bands correspond to the reference pp cross section scaled by A$_{\rm Pb}$.

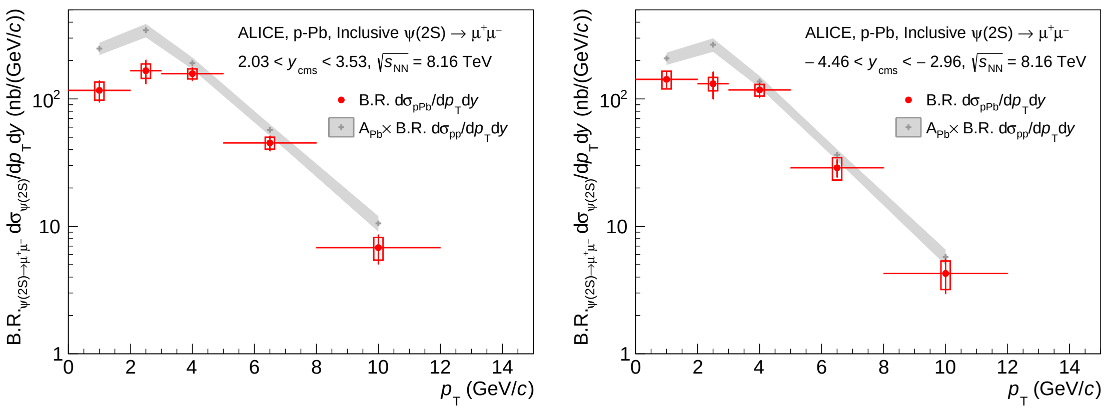

Figure 5.13: The differential cross sections (B.R.$_{\psi(2S)\to\mu^+\mu^-}$d$^2\sigma^{\psi(2S)}$/dyd$p_{\rm T}$) for p–Pb collisions at $\sqrt{s_{\rm NN}}$ = 8.16 TeV, shown separately for the forward and backward $y_{\rm cms}$ samples. The error bars represent the statistical uncertainties, while the boxes correspond to total systematic uncertainties. The latter are uncorrelated among the points, except for a very small correlated uncertainty (0.5% and 0.7% for the forward and backward $y_{\rm cms}$ samples, respectively). The grey bands correspond to the reference pp cross section scaled by A$_{\rm Pb}$.

before. At backward rapidity, the ratio seems to be significantly lower (2.9σ effect) than in pp, while at forward rapidity the values are compatible. The results are further compared with those obtained in pPb collisions at $\sqrt{s_{\rm NN}}$ = 5.02 TeV [1]. No significant $\sqrt{s_{\rm NN}}$ dependence can be observed within the experimental uncertainties.

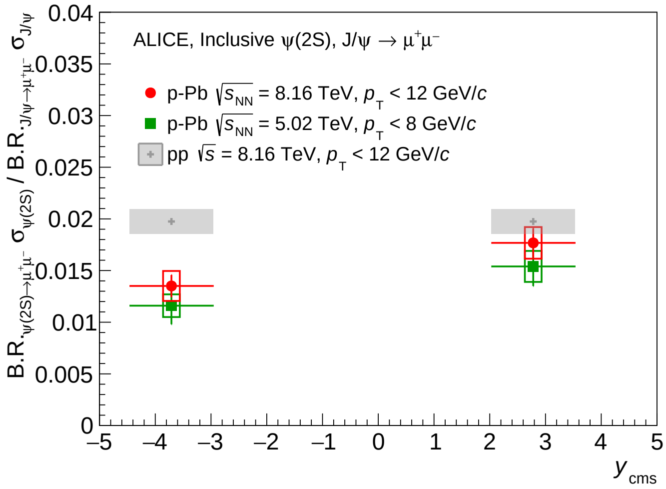

Figure 5.14: The ratio $(\mathrm{B.R.}_{\psi(2S)\to\mu^+\mu^-}\sigma^{\psi(2S)}/\mathrm{B.R.}_{J/\psi\to\mu^+\mu^-}\sigma^{J/\psi})$ as a function of y_{cms} for p–Pb collisions at $\sqrt{s_{\mathrm{NN}}}$ = 8.16 TeV, compared with the corresponding pp values, shown as a grey band and obtained via an interpolation of results at $\sqrt{s}$ = 5, 7, 8 and 13 TeV [15]. The error bars represent the statistical uncertainties, while the boxes correspond to uncorrelated systematic uncertainties. The published p–Pb results at $\sqrt{s_{\mathrm{NN}}}$ = 5.02 TeV [1] are also shown.

In Fig. 5.15 the p_{T}-dependence of the ratio has been plotted. A comparison with the corresponding ratio in pp collisions obtained through the interpolation is also provided on the same figure. These results show indication of a stronger relative suppression of ψ(2S) with respect to J/ψ at backward rapidity.

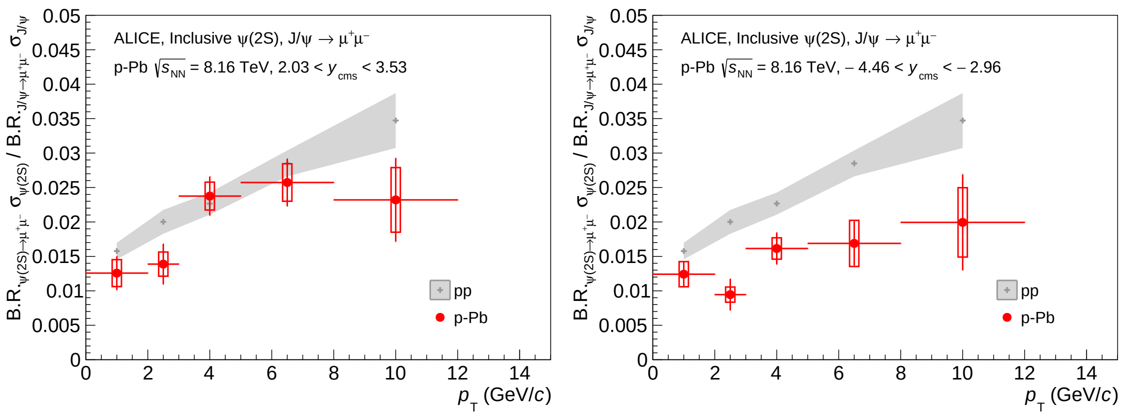

Figure 5.15: The ratio $(\mathrm{B.R.}_{\psi(2S)\to\mu^+\mu^-}\sigma^{\psi(2S)}/\mathrm{B.R.}_{J/\psi\to\mu^+\mu^-}\sigma^{J/\psi})$ as a function of p_{T}, for p–Pb collisions at $\sqrt{s_{\mathrm{NN}}}$ = 8.16 TeV, compared with the corresponding pp values, shown as a grey band and obtained via an interpolation of results at $\sqrt{s}$ = 7, 8 and 13 TeV [15]. The error bars represent the statistical uncertainties, while the boxes correspond to uncorrelated systematic uncertainties.

The suppression of ψ(2S) is directly expressed in terms of the nuclear modification factors: $R_{\rm pPb}^{\psi(2S)}$. Its evaluation is performed through the following expression:

$$R_{\rm pPb}^{\psi(2S)}(p_{\rm T}, y_{\rm cms}) = \frac{{\rm d}^2\sigma_{\rm pPb}^{\psi(2S)}/{\rm d}p_{\rm T}{\rm d}y_{\rm cms}}{{\rm A_{Pb}}\cdot {\rm d}^2\sigma_{\rm pp}^{\psi(2S)}/{\rm d}p_{\rm T}{\rm d}y_{\rm cms}} \tag{5.8}$$

where $A_{\rm Pb} = 208$ is the mass number of the Pb-nucleus.

The values of $R_{\rm pPb}^{\psi(2S)}$, integrated over the interval $p_{\rm T} < 12$ GeV/c, are as follows:

$$R_{\rm pPb}^{\psi(2S)}(2.03 < y_{\rm cms} < 3.53) = 0.628 \pm 0.050\,({\rm stat.}) \pm 0.069\,({\rm syst.uncorr.}) \pm 0.045\,({\rm syst.corr.})$$

$$R_{\rm Pbp}^{\psi(2S)}(-4.46 < y_{\rm cms} < -2.96) = 0.684 \pm 0.054\,({\rm stat.}) \pm 0.088\,({\rm syst.uncorr.}) \pm 0.049\,({\rm syst.corr.})$$

In Fig. 5.16, $R_{\rm pPb}^{\psi(2S)}$ as a function of rapidity is shown. The observations are also compared with those for $R_{\rm pPb}^{{\rm J}/\psi}$ [16].

ψ(2S) exhibits a stronger suppression Compared to J/ψ at backward rapidity, while the results are compatible at forward rapidity. The data are also compared (left panel) with theoretical model calculations based on initial-state effects or coherent energy loss. These calculations are independent of the specific resonance, and therefore they give same predictions for both J/ψ and ψ(2S). Calculations based on the CGC approach [17, 18] on nuclear shadowing [18, 19] that adopts different parametrizations (EPS09NLO [20], nCTEQ15 [21]) as well as coherent energy loss [18, 22], show good agreement with the J/ψ results, but fail to describe the ψ(2S) $R_{\rm pPb}$ at backward rapidity. Theory calculations from [6] are based on effects due to soft color exchanges in the hadronizing c$\bar{\rm c}$ pair. It considers the initial state as a CGC state, and therefore the results are constrained to only forward rapidity (low Bjorken-x values in the Pb nucleus), where explanation of the system using this approach is valid. The calculations based on final-state interactions with the comoving medium [7] are also compared with the experimental findings. Both the models reach a fairly good description of the data for both ψ(2S) and J/ψ, as shown

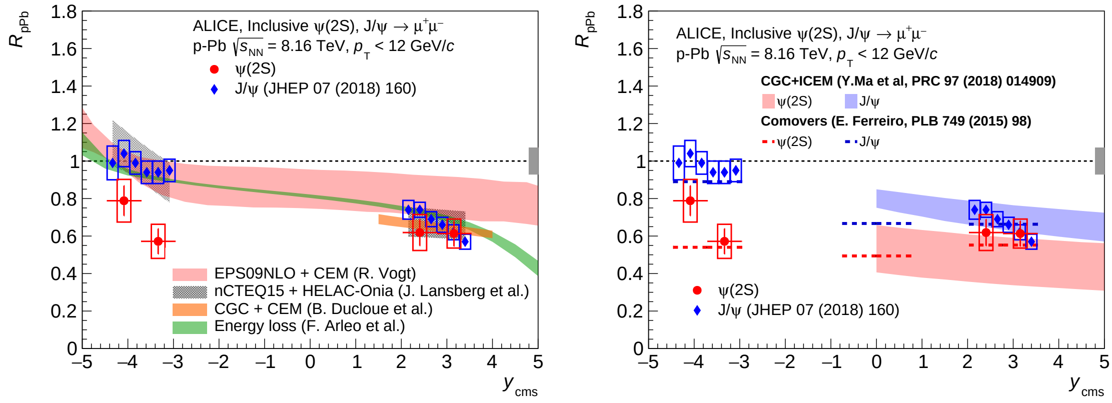

Figure 5.16: The $y_{\rm cms}$-dependence of $R_{\rm pPb}$ for ψ(2S) and J/ψ [16] in p–Pb collisions at $\sqrt{s_{\rm NN}}$ = 8.16 TeV. The error bars represent the statistical uncertainties, while the boxes correspond to uncorrelated systematic uncertainties and the box at $R_{\rm pPb} = 1$ to correlated systematic uncertainties. The results are compared with models including initial-state effects [17–19] and coherent energy loss [18,22] (left panel), and to models which also implement final-state effects [6,7] (right panel).

in the right panel of Fig. 5.16.

The $p_{\rm T}$-differential $R_{\rm pPb}^{\psi(2S)}$ are plotted in Fig. 5.17, separately for the forward and the backward rapidities, and compared with published results for J/ψ [16]. At forward rapidity the ψ(2S) suppression is compatible with that of J/ψ, while at backward rapidity the ψ(2S) suppression is visibly stronger. The ψ(2S) suppression is found to be independent of $p_{\rm T}$ within its experimental uncertainties at backward rapidity. The CGC-based model [6] calculations give a fair description of the experimental findings. No model calculation is available at backward rapidity.

In Fig. 5.18, a comparison of the rapidity dependence of ψ(2S) suppression at $\sqrt{s_{\rm NN}}$ = 8.16 TeV and 5.02 TeV [16] is shown along with the results from theoretical models based on final-state effects [6,7]. Both models describe well the ψ(2S) $R_{\rm pPb}$ at both energies. In Fig. 5.19, $R_{\rm pPb}^{\psi(2S)}$ as a function of $p_{\rm T}$ at the two energies ($\sqrt{s_{\rm NN}}$ = 5.02 and 8.16 TeV) are presented. The results match within uncertainties, although at the backward-rapidity, results for $\sqrt{s_{\rm NN}}$ = 5.02 TeV seems to indicate an increasing trend towards high $p_{\rm T}$.

The double ratio of the ψ(2S) and J/ψ cross sections between p–Pb and pp as shown

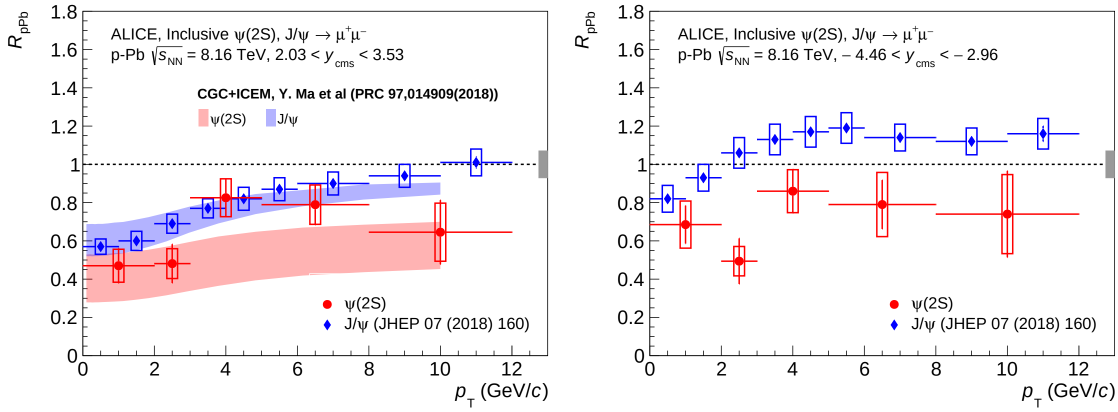

Figure 5.17: The p_{T}-dependence of R_{pPb} for ψ(2S) and J/ψ at forward (left) and backward (right) rapidity in p–Pb collisions, at $\sqrt{s_{\mathrm{NN}}} = 8.16$ TeV. The error bars represent the statistical uncertainties, while the boxes correspond to uncorrelated systematic uncertainties and the box at $R_{\mathrm{pPb}} = 1$ to correlated systematic uncertainties. The comparison with the results of a CGC-based model [6], which implements final-state effects, is also shown.

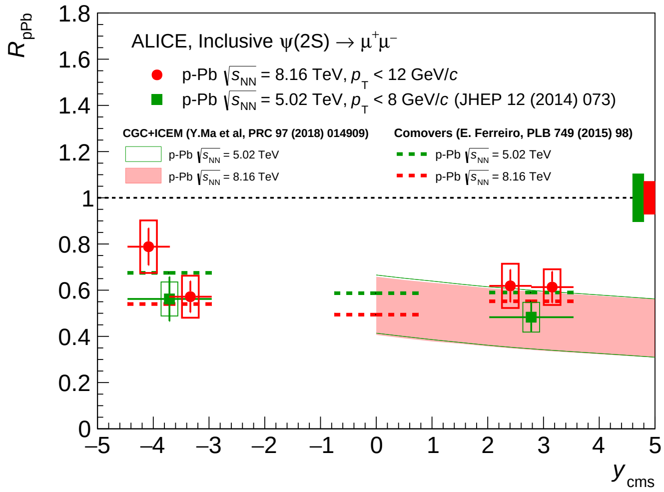

Figure 5.18: The comparison of the rapidity dependence of R_{pPb} for ψ(2S) in p–Pb collisions at $\sqrt{s_{\mathrm{NN}}} = 8.16$ and 5.02 TeV [1]. The error bars represent the statistical uncertainties, while the boxes correspond to uncorrelated systematic uncertainties and the boxes at $R_{\mathrm{pPb}} = 1$ to correlated systematic uncertainties, separately shown for the two energies. The results are also compared with theoretical models that include final-state effects [6,7].

in Fig. 5.20 and Fig. 5.21 make it easier to quantify the relative suppression of the two resonances with respect to pp collisions. A similar observation is also exhibited here. The y_{cms}-dependence shows a relative suppression of the ψ(2S) with respect to the J/ψ at backward rapidity, while the p_{T}-dependence does not follow any trend.

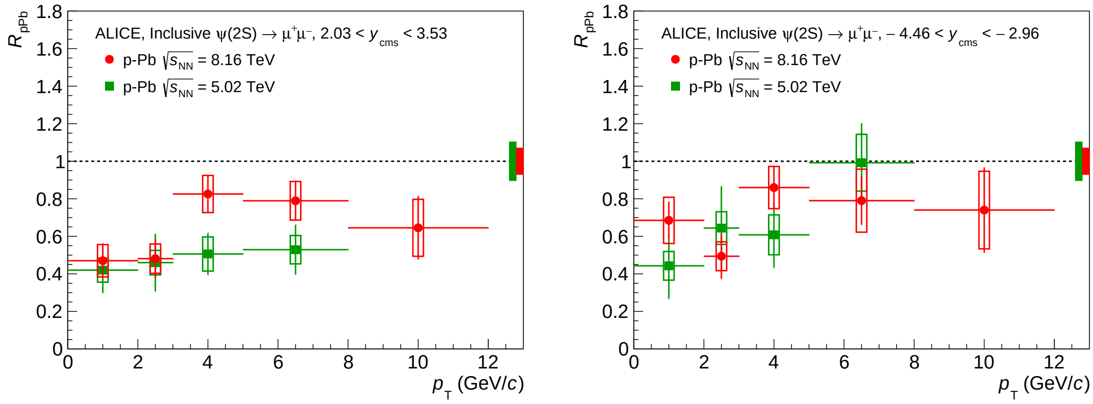

Figure 5.19: The comparison of the transverse-momentum dependence of $R_{\rm pPb}$ for ψ(2S) in p–Pb collisions at $\sqrt{s_{\rm NN}}$ = 8.16 and 5.02 TeV [1]. The error bars represent the statistical uncertainties, while the boxes correspond to uncorrelated systematic uncertainties and the boxes at $R_{\rm pPb} = 1$ to correlated systematic uncertainties, separately shown for the two energies.

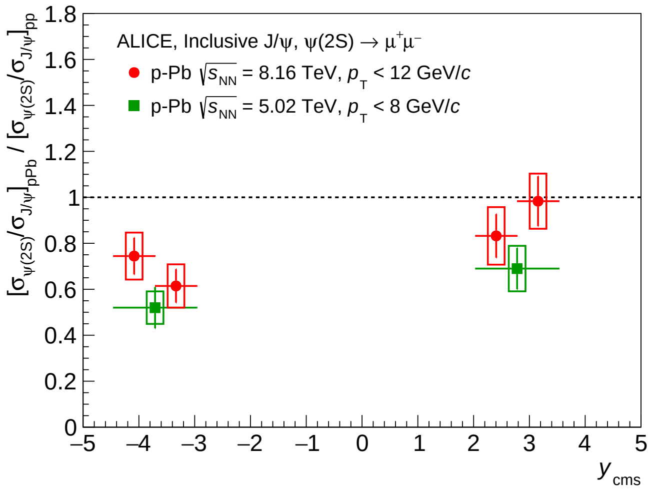

Figure 5.20: The double ratio of ψ(2S) and J/ψ cross sections in p–Pb and pp collisions as a function of rapidity, at $\sqrt{s_{\rm NN}}$ = 8.16 TeV, compared with the corresponding results at $\sqrt{s_{\rm NN}}$ = 5.02 TeV [1]. The error bars represent the statistical uncertainties, while the boxes correspond to uncorrelated systematic uncertainties.

Discussions

The results of studies on the inclusive ψ(2S) production in p–Pb collisions at $\sqrt{s_{\rm NN}}$ = 8.16 TeV, as a function of $p_{\rm T}$ and rapidity have been presented. The two times larger statistics of the current datasets than the one at $\sqrt{s_{\rm NN}}$ = 5.02 TeV [16] have significantly improved the statistical uncertainties in the results and made

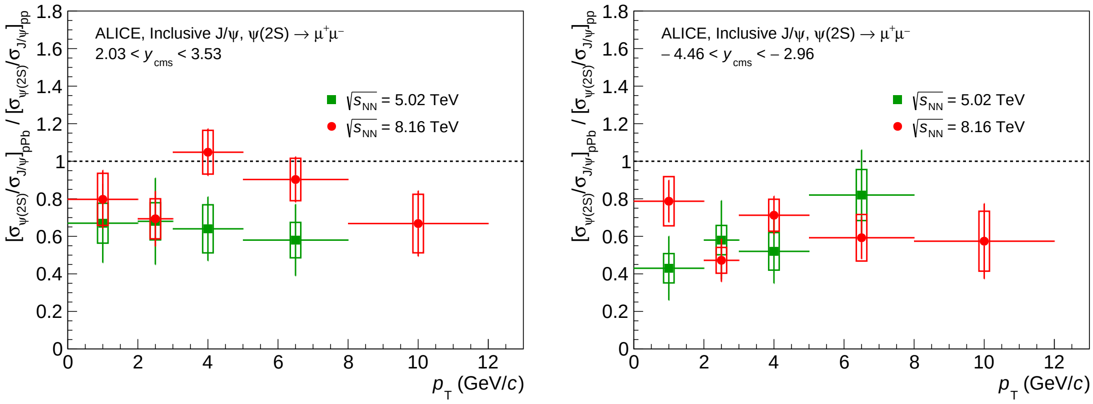

Figure 5.21: The double ratio of $\psi(2S)$ and J/ψ cross sections in p–Pb and pp collisions as a function of transverse momentum, at forward (left) and backward (right) rapidity at $\sqrt{s_{NN}} = 8.16$ TeV, compared with the corresponding results at $\sqrt{s_{NN}} = 5.02$ TeV [1]. The error bars represent the statistical uncertainties, while the boxes correspond to uncorrelated systematic uncertainties.

differential measurements in finer pt and y bins possible.

The values of the R_{pPb} show a 30–40% $\psi(2S)$ suppression at both forward and backward rapidity, with no significant p_T dependence. The suppression being mainly driven by the initial-state effects such as nuclear shadowing at forward rapidity, is similar to that for J/ψ. $\psi(2S)$ is strongly suppressed than J/ψ at backward rapidity, which is well reproduced in the model based on final-state effects. These results confirm, with a better accuracy and higher p_T reach up to 12 GeV/c, the previous observations carried out by ALICE in p–pb collisions at $\sqrt{s_{NN}} = 5.02$ TeV.

Centrality dependence study of $\psi(2S)$ cross-section

Motivation

The J/ψ and $\psi(2S)$ suppression as a function of centrality has also been studied in p-Pb collisions at $\sqrt{s_{NN}} = 5.02$ TeV [23,25]. The difference between the $\psi(2S)$ and J/ψ suppression seems to increase with increasing centrality, especially at the backward rapidity, which indicates that shadowing or coherent parton energy-loss mechanisms are not sufficient to describe the ψ(2S) suppression [25]. Complementarily, the ALICE Collaboration also studied the charged particle multiplicity dependence of J/ψ production at forward, mid, and backward rapidity. At mid-y [26], the study has shown an increase of the relative J/ψ yields with the relative charged-particle multiplicity. At forward rapidity the increase tends to saturate towards the highest multiplicities, whereas at backward rapidity there is a hint of a faster-than-linear increase with multiplicity.

Also, in high-multiplicity p–Pb events, long-range angular correlations between the J/ψ at large rapidity and charged particles at midrapidity are observed [27]. These correlations are reminiscent of those observed in Pb–Pb collisions, which are often interpreted as signatures of the collective motion of the particles during the hydrodynamic evolution of the hot and dense medium. The data analysis of ψ(2S) measurement as a function of centrality in p–Pb collisions at $\sqrt{s_{\rm NN}}$ = 8.16 TeV is reported in this section. The centrality dependence has been studied by calculating the relative ψ(2S) to J/ψ cross section ratio in p–Pb to pp collisions known as double ratio and nuclear modification factor $Q_{\rm pPb}$.

Physics Selection and Pile-up

After passing the track selection cuts, the tracks must satisfy some physics conditions applied.

In p–Pb collisions, the method of centrality estimation is different from that in case of Pb–Pb collisions. In this case, the centrality cannot be estimated using the V0 signal amplitudes as they may induce a bias unrelated to the collision geometry in p–Pb collisions. More details on this can be found in [24]. On the other hand, the energy deposited in the ZDC by nucleons emitted from the nuclear de-excitation processes after the collisions, are free from such bias. The centrality classes are

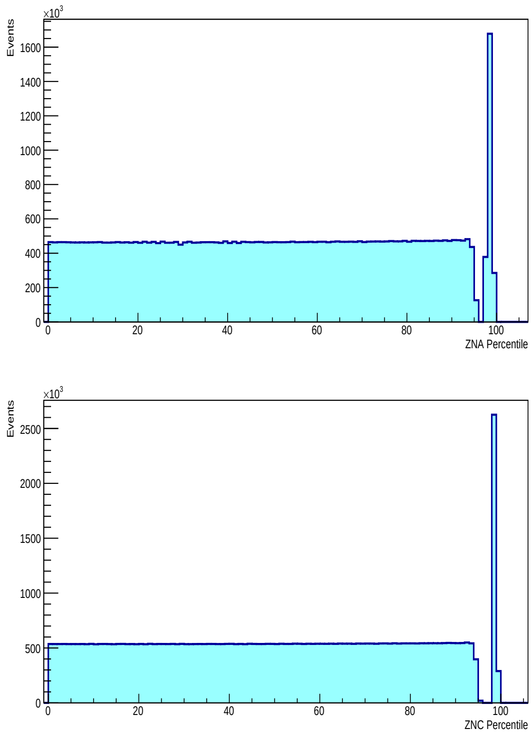

Figure 5.22: ZNA and ZNC multiplicity with CINT7 trigger for p-Pb (top) and Pb-p (bottom) respectively.

measured using the ZN detector (neutron calorimeter of ZDC): ZNA (p–Pb) and ZNC (Pb–p). The centrality are classified on the basis of certain ranges of energy deposited in the Pb-remnant side of ZN. Then the number of participant nucleons $\langle N_{part} \rangle$ is calculated for a particular ZN-energy class. As a next step, number of binary nucleon collisions $\langle N_{coll} \rangle$ is calculated assuming that the charged-particle multiplicities determined at mid-rapidities are proportional to the $\langle N_{part} \rangle$. Fig. 5.22 shows the stability of the events over multiplicity range 0–90%. There are few spikes in the multiplicities over 90%. These events in the range 90–100% cannot be considered for analysis, as there are still problems related to the association of the correct centrality estimations using the ZDC.

The number of CMUL7 triggers decrease $\sim 15\%$ after physics selection and pile-up cut.

Signal Extraction

The signal extraction procedure is the same as stated in the previous section. Few example fits are shown in Fig.5.23.

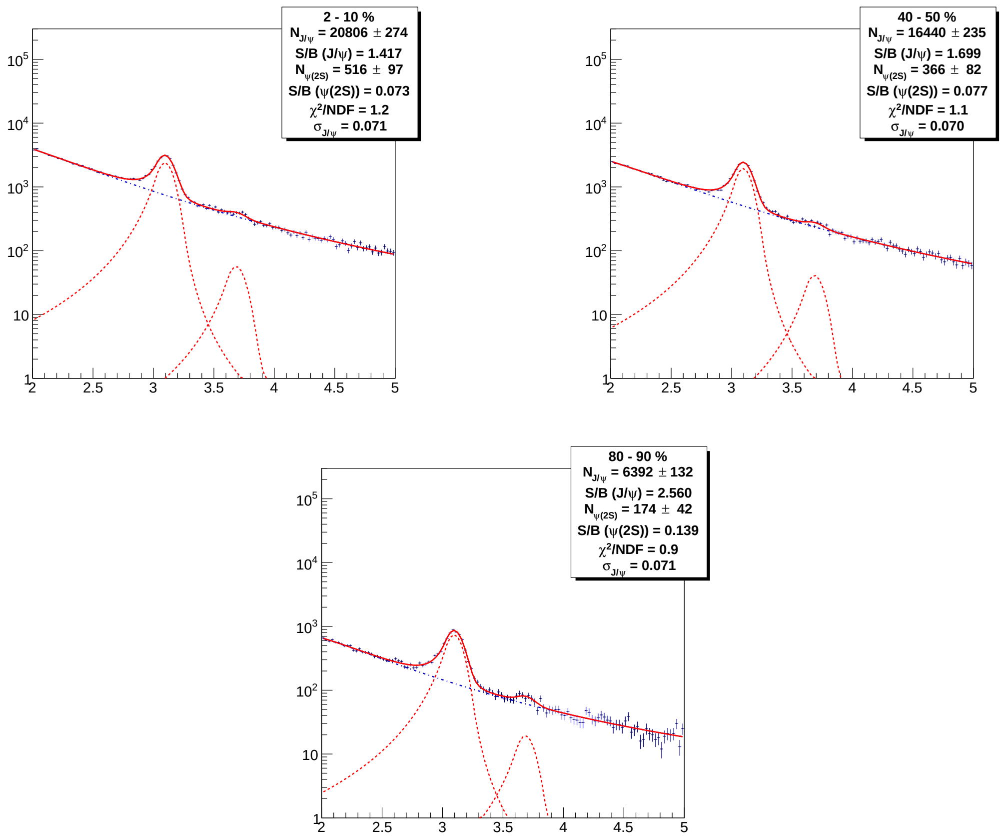

Figure 5.23: The typical fits to the invariant mass spectra for three different centrality classes in p–Pb collisions.

Number of ψ(2S) and J/ψ as a function of centrality

The number of ψ(2S) and J/ψ has been obtained for 9 centrality classes, in the range $0-90\%$ and are reported in table 5.13 (p–Pb) and table 5.14 (Pb–p). The fitting results in three centrality bins are shown in Fig. 5.24, 5.25, 5.26 (p–Pb) and 5.27, 5.28, 5.29 (Pb–p).

Table 5.13: The number of $\psi(2S)$ and J/ψ in different centrality for the p-Pb period. The first uncertainty is statistical and the second one is the systematic one. The 5% systematic due to the resonance width is not included.

p–Pb	$N_{\psi(2S)} \pm stat \pm syst$
0-10%	662 ± 108 (16.4%) ± 52 (8.0%)
2-10%	524 ± 97 (18.6%) ± 40 (7.8%)
10-20%	356 ± 100 (28.3%) ± 26 (7.6%)
20-30%	228 ± 91 (40.1%) ± 19 (8.4%)
30-40%	323 ± 85 (26.4%) ± 23 (7.1%)
40-50%	324 ± 77 (23.8%) ± 20 (6.4%)
50-60%	206 ± 67 (32.4%) ± 12 (6.3%)
60-70%	174 ± 58 (33.6%) ± 20 (11.8%)
70-80%	188 ± 47 (25.4%) ± 12 (6.8%)
80-90%	165 ± 42 (25.5%) ± 9 (5.7%)
20-40%	555 ± 126 (22.7%) ± 36 (6.6%)
40-60%	529 ± 102 (19.4%) ± 32 (6.1%)
60-80%	362 ± 76 (21.2%) ± 31 (8.8%)

p–Pb	$N_{J/\psi} \pm stat \pm syst$
0-10%	25556 ± 304 (1.2%) ± 836 (3.3%)
2-10%	20040 ± 270 (1.3%) ± 655 (3.3%)
10-20%	22734 ± 285 (1.3%) ± 721 (3.2%)
20-30%	21651 ± 267 (1.2%) ± 689 (3.2%)
30-40%	18737 ± 241 (1.3%) ± 605 (3.2%)
40-50%	15901 ± 219 (1.4%) ± 496 (3.1%)
50-60%	12993 ± 196 (1.5%) ± 400 (3.1%)
60-70%	10615 ± 180 (1.7%) ± 335 (3.2%)
70-80%	8085 ± 145 (1.8%) ± 256 (3.2%)
80-90%	6195 ± 130 (2.1%) ± 198 (3.2%)
20-40%	40360 ± 358 (0.9%) ± 1273 (3.2%)
40-60%	28891 ± 295 (1.0%) ± 896 (3.1%)
60-80%	18701 ± 234 (1.3%) ± 592 (3.2%)

A$\times\epsilon$

The $A \times \epsilon$ value for integrated $p_{\rm T}$ and y has been used for all the multiplicity bins.

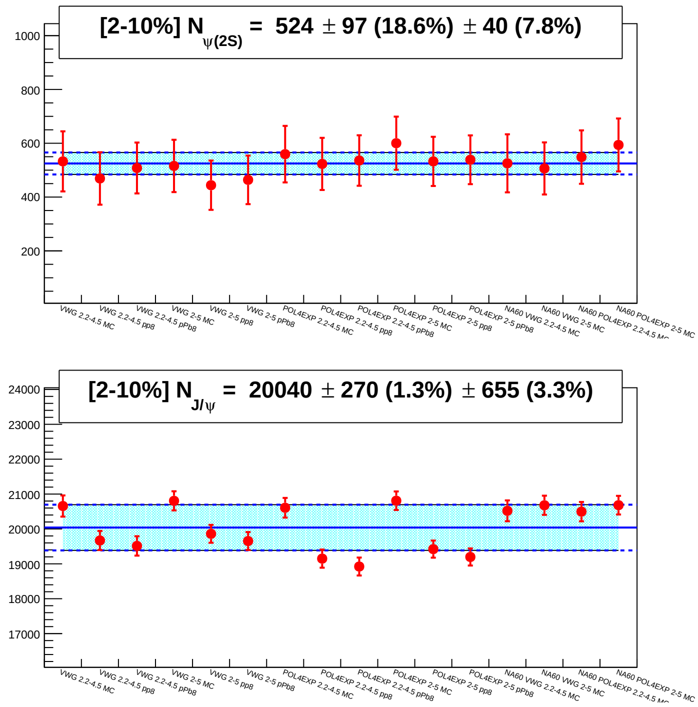

Figure 5.24: The ψ(2S) and the J/ψ raw yields as a function of the tests performed in the centrality class $2-10\%$ in p–Pb collisions.

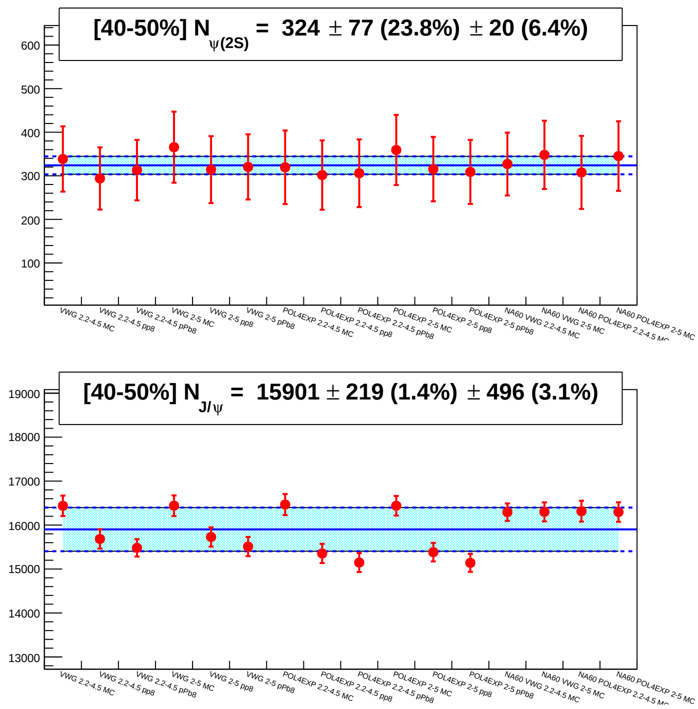

Figure 5.25: The ψ(2S) and the J/ψ raw yields as a function of the tests performed in the centrality class $40-50\%$ in p–Pb collisions.

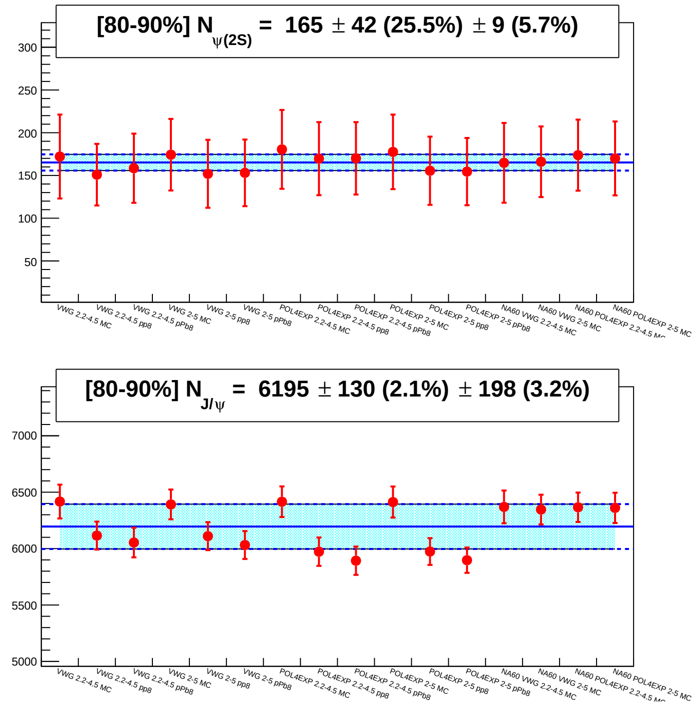

Figure 5.26: The ψ(2S) and the J/ψ raw yields as a function of the tests performed in the centrality class $80-90\%$ in p–Pb collisions.

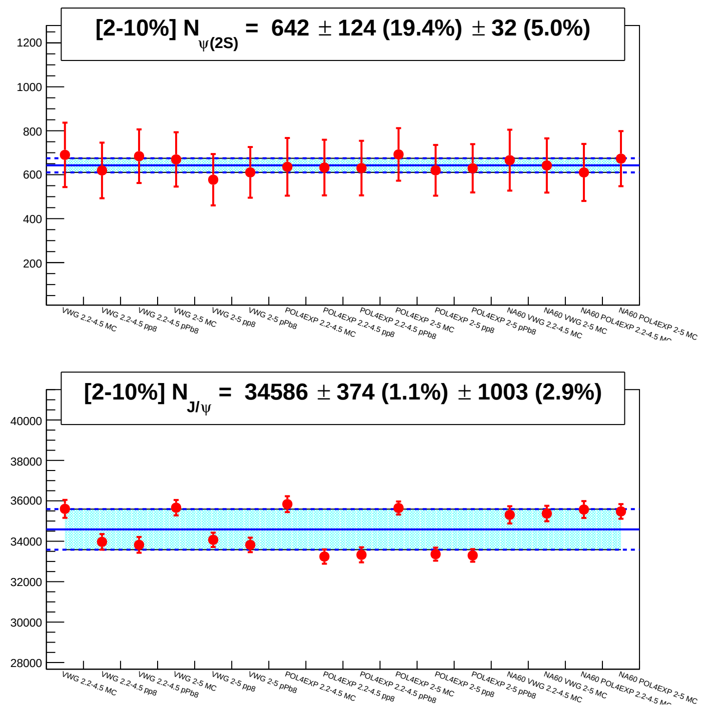

Figure 5.27: The ψ(2S) and the J/ψ raw yields as a function of the tests performed in the centrality class $2-10\%$ in Pb–p collisions.

Table 5.14: The number of ψ(2S) and J/ψ for different centrality bins for the Pb–p period. The first uncertainty is statistical and the second one is the systematic one. The 5% due to the resonance width is not included.

Pb–p	$N_{\psi(2S)} \pm stat \pm syst$
0-10%	787 ± 139 (17.7%) ± 44 (5.6%)
2-10%	642 ± 124 (19.4%) ± 32 (5.0%)
10-20%	415 ± 124 (30.0%) ± 26 (6.4%)
20-30%	505 ± 110 (21.9%) ± 42 (8.4%)
30-40%	392 ± 98 (25.0%) ± 36 (9.2%)
40-50%	227 ± 84 (37.3%) ± 20 (8.9%)
50-60%	228 ± 71 (31.4%) ± 19 (8.5%)
60-70%	146 ± 57 (39.3%) ± 12 (8.6%)
70-80%	97 ± 44 (45.7%) ± 14 (15.1%)
80-90%	104 ± 36 (34.3%) ± 8 (7.7%)
20-40%	903 ± 150 (16.6%) ± 76 (8.5%)
40-60%	456 ± 111 (24.4%) ± 29 (6.5%)
60-80%	241 ± 70 (29.2%) ± 23 (9.6%)

Pb–p	$N_{J/\psi(2S)} \pm stat \pm syst$
0-10%	44191 ± 420 (1.0%) ± 1342 (3.0%)
2-10%	34586 ± 374 (1.1%) ± 1003 (2.9%)
10-20%	38108 ± 371 (1.0%) ± 1075 (2.8%)
20-30%	33283 ± 342 (1.0%) ± 1015 (3.1%)
30-40%	27894 ± 305 (1.1%) ± 797 (2.9%)
40-50%	22115 ± 265 (1.2%) ± 642 (2.9%)
50-60%	17055 ± 218 (1.3%) ± 488 (2.9%)
60-70%	12601 ± 185 (1.5%) ± 357 (2.8%)
70-80%	9080 ± 148 (1.6%) ± 251 (2.8%)
80-90%	6069 ± 120 (2.0%) ± 176 (2.9%)
20-40%	61101 ± 462 (0.8%) ± 1751 (2.9%)
40-60%	39144 ± 345 (0.9%) ± 1104 (2.8%)
60-80%	21686 ± 234 (1.1%) ± 603 (2.8%)

The p-p reference

The detailed method to obtain pp reference has been described in the previous section 5.1.5. The cross section evaluated for the integrated $p_{\rm T}$ and y range, has been used here for all the centrality bins.

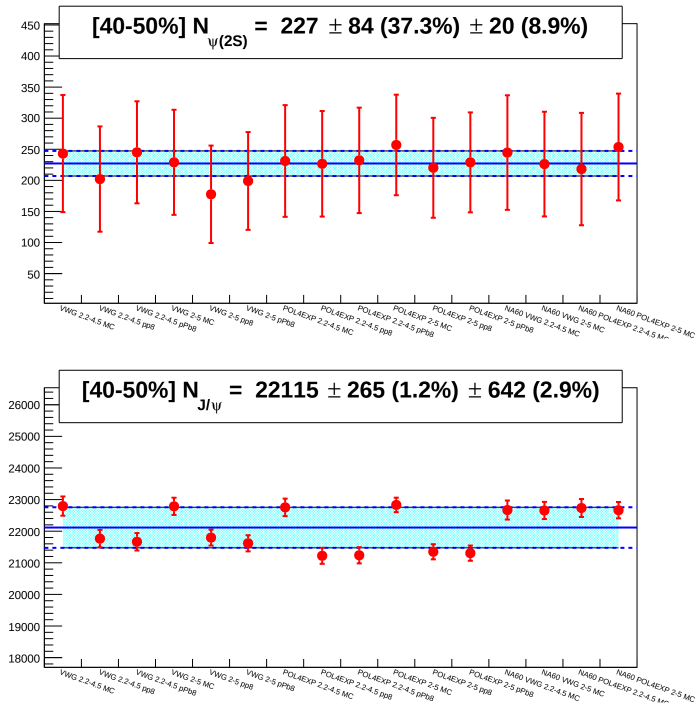

Figure 5.28: The $\psi(2S)$ and the J/ψ raw yields as a function of the tests performed in the centrality class $40 - 50\%$ in Pb–p collisions.

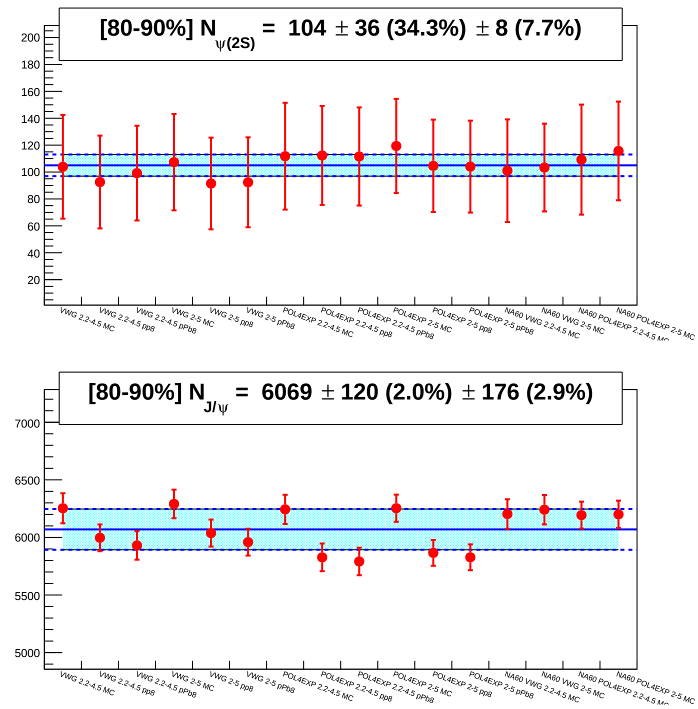

Figure 5.29: The $\psi(2S)$ and the J/ψ raw yields as a function of the tests performed in the centrality class $80 - 90\%$ in Pb–p collisions.

	$\sigma_{\psi(2S)}/\sigma_{J/\psi}$
$0 < p_{\mathrm{T}} < 12$ (GeV/c) $2.50 < y < 4.00$	0.149 ± 0.009 (6.0%) $\pm$ 1% $\pm$ 1%

Systematics

The evaluation of systematic uncertainty is also described in the previous section.

Signal extraction

This uncertainty varies from 5.7-11.8% and 5.0-15.1% in centrality bins in p-A and A-p respectively. In addition, the extra uncertainty of 5%, which comes from fixing of the $\sigma_{J/\psi}/\sigma_{\psi(2S)}$ has also been added in the results. This systematic of 5% has been estimated using the method mentioned in the previous section.

Trigger efficiency

The p_{T} and y integrated trigger uncertainty amounts to 2.4% and 2.9% in p-Pb and Pb-p respectively. This systematic on trigger efficiency is considered as uncorrelated between p-A and A-p. In addition to those values, an uncertainty of 1% has been taken as the intrinsic chamber efficiency.

Tracking efficiency

A 1% and 2% uncorrelated uncertainty on the tracking efficiency is applied for p-A and A-p respectively.

Matching efficiency

An uncorrelated contribution to the systematic uncertainty of 1% is considered.

Input Monte Carlo parametrization

A systematic uncertainty of 3% and 1.5% has been considered in pA and Ap respectively.

This uncertainty has been considered correlated for all centrality classes.

pp reference

The pp reference has a systematic uncertainty of 6% for the ratio and a 1% to take into account the rapidity shift between p-Pb and pp collisions. In addition a 1% is evaluated to take into account the difference between the theoretical predictions and the interpolated ratio $\psi(2S)/\mathrm{J}/\psi$.

Table 5.15: The systematic uncertainties for both p-Pb and Pb-p periods as estimated from the present analysis.

source	p-Pb (%)	Pb-p (%)
signal extraction	5.7-11.8 + 5	5.0-15.1 + 5
trigger (global)	2.6	3.1
tracking (global)	1	2
matching (global)	1	1
MC inputs (global)	3	1.5
MC inputs	2.5-2.7	1.6-1.7
pp reference (global)	6.2(ratio) + 7.1(J/ψ)	6.2(ratio) + 7.1(J/ψ)
pile-up (global)	2	2
FNorm (global)	1	1
FNorm	0.1-1.0	0.1-0.8
T_{pPb}	2.1-4.8	2.1-4.8

All the systematic uncertainties are summarised in Table 5.15.

Results

All the results are plotted as a function of average number of binary nucleon-nucleon collisions ($\mathrm{N_{coll}}$). $\mathrm{N_{coll}}$ is determined using hybrid method [24] which gives unbiased centrality estimator. The relation between the event centrality classes and $\mathrm{N_{coll}}$ are given in Table 5.16.

Table 5.16: The relation between $\mathrm{N_{coll}}$ and ZN centrality classes determined using the hybrid model.

ZN classes	$\mathrm{N_{coll}}$
0-10%	12.9
2-10%	12.7
10-20%	11.5
20-30%	10.4
30-40%	9.21
40-50%	7.82
50-60%	6.37
60-70%	4.93
70-80%	3.63
80-90%	2.53
20-40%	9.81
40-60%	7.09
60-80%	4.28

The single ratio : $\psi(2S)/\mathrm{J}/\psi$

In Figs. 5.30 and 5.31 the ratio of ψ(2S) and J/ψ cross-sections times the branching ratio is plotted for the two resonances for pPb and Pbp collisions. The values for the same are listed in Table 5.17 and 5.18 for p–Pb and Pb–p collisions, respectively. The results have been compared with the same ratio obtained in p–Pb collisions at $\sqrt{s_{\mathrm{NN}}} = 5.02$ TeV [25] as well as in pp collisions at $\sqrt{s} = 7$ TeV [10]. The systematic uncertainty includes the systematic on the number of J/ψ and ψ(2S), the systematic from Monte Carlo input for J/ψ and ψ(2S) and the 5% systematic associated to the width of ψ(2S). All the other systematics such as tracking, trigger, matching and pileup systematics cancel out, as they are the same for the two resonances.

Table 5.17: The ψ(2S)/J/ψ values at $\sqrt{s_{NN}} = 8.16$ TeV in p-Pb collisions for different centrality bins.

	ψ(2S)/J/ψ $\pm$ *stat* $\pm$ *syst* $[2.03 < y < 3.53]$
2-10%	0.0246 $\pm$ 0.0046 (18.7%) $\pm$ 0.0026 (10.5%)
10-20%	0.0148 $\pm$ 0.0042 (28.4%) $\pm$ 0.0015 (10.4%)
20-40%	0.0130 $\pm$ 0.0029 (22.3%) $\pm$ 0.0012 (9.6%)
40-60%	0.0173 $\pm$ 0.0033 (19.1%) $\pm$ 0.0016 (9.0%)
60-80%	0.0182 $\pm$ 0.0038 (20.9%) $\pm$ 0.0021 (11.3%)
80-90%	0.0251 $\pm$ 0.0064 (25.5%) $\pm$ 0.0023 (9.2%)

Table 5.18: The ψ(2S)/J/ψ values at $\sqrt{s_{NN}} = 8.16$ TeV in Pb-p collisions for different centrality bins.

	ψ(2S)/J/ψ $\pm$ *stat* $\pm$ *syst* $[-4.46 < y < -2.96]$
2-10%	0.0176 $\pm$ 0.0034 (19.3%) $\pm$ 0.0014 (8.1%)
10-20%	0.0103 $\pm$ 0.0031 (30.1%) $\pm$ 0.0009 (8.9%)
20-40%	0.0140 $\pm$ 0.0023 (16.4%) $\pm$ 0.0014 (10.1%)
40-60%	0.0110 $\pm$ 0.0027 (24.5%) $\pm$ 0.0010 (9.2%)
60-80%	0.0105 $\pm$ 0.0031 (29.5%) $\pm$ 0.0012 (11.6%)
80-90%	0.0162 $\pm$ 0.0056 (34.6%) $\pm$ 0.0016 (10.0%)

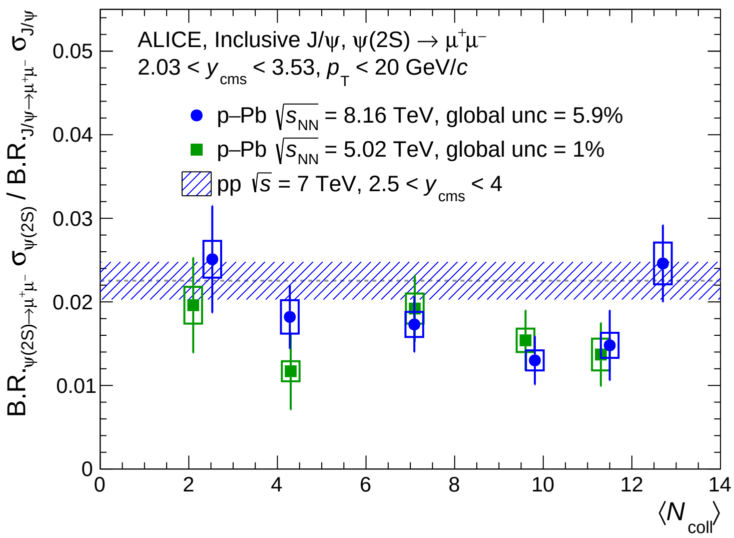

Figure 5.30: The ratio ψ(2S)/J/ψ as a function of centrality at $\sqrt{s_{NN}} = 8.16$ TeV for p–Pb collisions. The result is compared with the ratio obtained in p–Pb collisions at $\sqrt{s_{NN}} = 5.02$ TeV [28] and in pp collisions at 7 TeV. The error bar and the box correspond to statistical and systematic uncertainties, respectively.

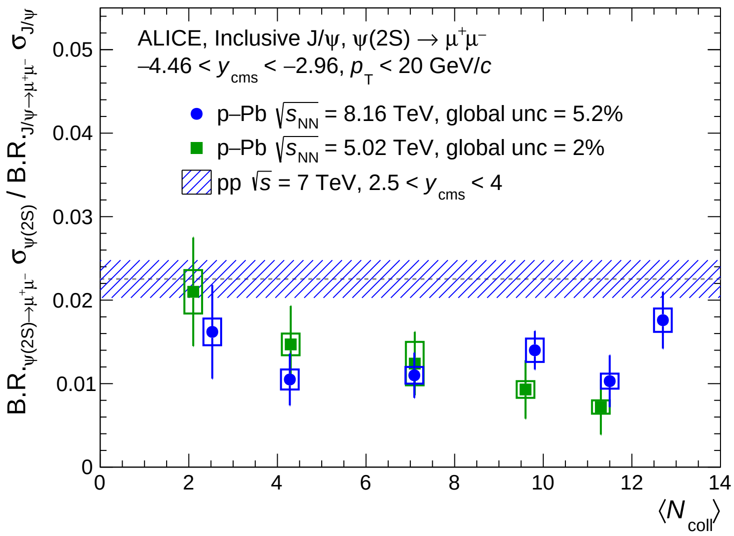

Figure 5.31: The ratio ψ(2S)/J/ψ as a function of centrality at $\sqrt{s_{\mathrm{NN}}}$ = 8.16 TeV for Pb–p collisions. The result is compared with the ratio obtained in Pb–p collisions at $\sqrt{s_{\mathrm{NN}}}$ = 5.02 TeV [28] and in pp collisions at 7 TeV.

Several observations can be made from the plots.

Firstly, the ψ(2S)/J/ψ ratio is independent of the collision energy. Secondly, the ratio seems to be smaller in p–Pb than in pp collisions, in both the rapidity regions and for all centrality ranges, except for the most peripheral, and the most central bins. In this context, it is worthy to mention that no significant energy dependence is found in the ψ(2S)/J/ψ ratio in pp collisions [12] also. Thus, the production of the ψ(2S) in p–Pb collisions appears to be suppressed compared to that of the J/ψ with respect to the expectation from pp collisions. Thirdly, constrained with the current experimental uncertainties, it is not possible to conclude the trend of the ratio as a function of centrality. Finally, the suppression of the ψ(2S) relative to the J/ψ in p–Pb compared to pp collisions seems to be stronger at the backward rapidity (Pb–p) than at the forward rapidity (p–Pb).

The double ratio : $(\psi(2S)/\mathrm{J}/\psi)_{pA}/(\psi(2S)/\mathrm{J}/\psi)_{pp}$

The double ratio is computed dividing the ratio of ψ(2S) and J/ψ cross-sections in p–Pb (and Pb–p) collisions by the same ratio observed in pp collisions. The ratio

$\sigma_{\psi(2S)}/\sigma_{J/\psi}$ in pp collisions is the one obtained with the interpolation procedure. The uncorrelated systematic uncertainty includes the systematic on the number of J/ψ and ψ(2S) and the 5% systematic associated to the width of ψ(2S) and the Monte-Carlo input systematic, while the global correlated systematic is computed considering the pp reference.

The values are reported in Table 5.19 and 5.20 for p–Pb and Pb–p collisions, respectively.

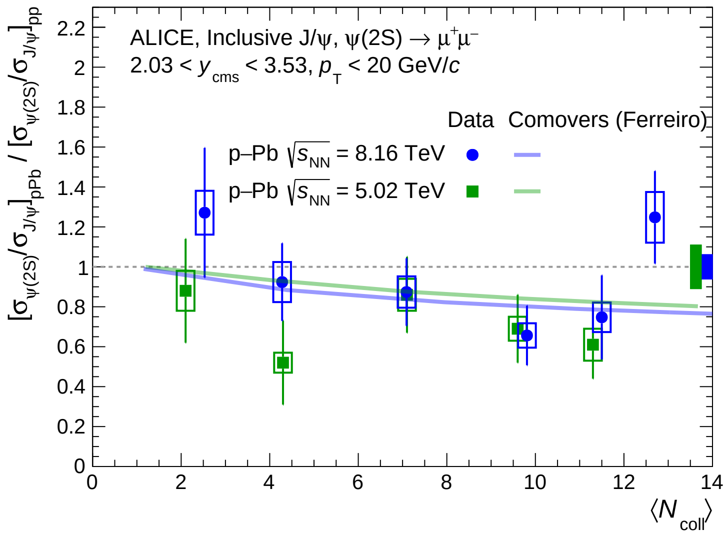

Figure 5.32: The double ratio as a function of centrality at $\sqrt{s_{\mathrm{NN}}}$ = 8.16 TeV for p–Pb collisions. The result is compared with the double ratio obtained in p–Pb collisions at $\sqrt{s_{\mathrm{NN}}}$ = 5.02 TeV [28] and the theoretical predictions of the Comovers model [29, 30].

Table 5.19: The double ratio at $\sqrt{s_{\mathrm{NN}}}$ = 8.16 TeV in p-Pb collisions. The first uncertainty is statistical, the second is the uncorrelated systematic while the third one is the correlated systematic.

	$(\psi(2S)/J/\psi)_{Ap}/(\psi(2S)/J/\psi)_{pp} \pm stat \pm syst$ [2.03 < y < 3.53]
2-10%	1.2479 ± 0.2316 (18.6%) ± 0.1307 (10.5%) ± 0.0769 (6.2%)
10-20%	0.7473 ± 0.2101 (28.1%) ± 0.0763 (10.2%) ± 0.0461 (6.2%)
20-40%	0.6563 ± 0.1491 (22.7%) ± 0.0633 (9.6%) ± 0.0405 (6.2%)
40-60%	0.8738 ± 0.1687 (19.3%) ± 0.0815 (9.3%) ± 0.0539 (6.2%)
60-80%	0.9238 ± 0.1943 (21.0%) ± 0.1032 (11.2%) ± 0.0569 (6.2%)
80-90%	1.2711 ± 0.3246 (25.5%) ± 0.1149 (9.0%) ± 0.0784 (6.2%)

A conclusion similar to the one derived from single ratio plot, can be made in case

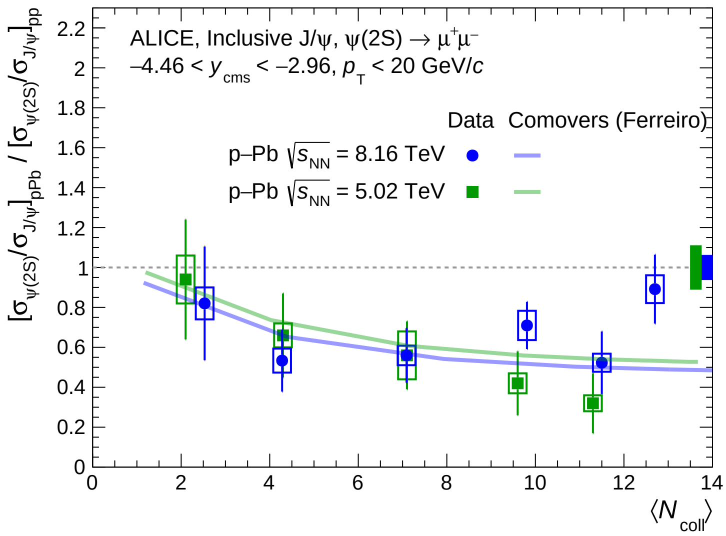

Figure 5.33: The double ratio as a function of centrality at $\sqrt{s_{\mathrm{NN}}}$ = 8.16 TeV for Pb–p collisions. The result is compared with the double ratio obtained in Pb–p collisions at $\sqrt{s_{\mathrm{NN}}}$ = 5.02 TeV [28] and the theoretical predictions of the Comovers model [29, 30].

Table 5.20: The double ratio at $\sqrt{s_{\mathrm{NN}}}$ = 8.16 TeV in Pb-p collisions. The first uncertainty is statistical, the second is the uncorrelated systematic while the third one is the correlated systematic.

	$(\psi(2S)/J/\psi)_{Ap}/(\psi(2S)/J/\psi)_{pp} \pm stat \pm syst$ $[-4.46 < y < -2.96]$
2-10%	0.8914 ± 0.1724 (19.3%) ± 0.0711 (8.0%) ± 0.0549 (6.2%)
10-20%	0.5229 ± 0.1563 (29.9%) ± 0.0460 (8.8%) ± 0.0322 (6.2%)
20-40%	0.7097 ± 0.1180 (16.6%) ± 0.0742 (10.5%) ± 0.0437 (6.2%)
40-60%	0.5594 ± 0.1363 (24.4%) ± 0.0497 (8.9%) ± 0.0345 (6.2%)
60-80%	0.5336 ± 0.1551 (29.1%) ± 0.0608 (11.4%) ± 0.0329 (6.2%)
80-90%	0.8202 ± 0.2844 (34.7%) ± 0.0812 (9.9%) ± 0.0506 (6.2%)

of double ratio as well. The Comovers + EPS09LO model considers dissociation of resonances through interactions with 'comoving particles' (partonic or hadronic, not being declared in the model) created in the same rapidity region. This phenomenon is governed by the comover interaction cross sections which amounts to, 0.65 mb for J/ψ and 6 mb (ψ(2S)), which is determined from the fits to low-energy experimental data. The main source of uncertainty in this model comes from the nPDF parametrisation, which is strongly correlated between the J/ψ and the ψ(2S) and consequently is canceled in the ratio. The agreement between the model calculations and the experimental results is good at both the collision energies. The double ratio decreases with increase of collision energy in the model because of the increase of the comover density. However, with the present systematic uncertainties, it is difficult to confirm the observation of a decrease of the double ratio as a function of $N_{\rm coll}$.

The nuclear modification factor ($Q_{\rm pPb}$)

To compute the $Q_{\rm pPb}$ the formula used is:

$$Q^{i}_{pPb} = \frac{N^{i}_{\rm J/\psi}}{< T^{i}_{pPb} > \cdot N^{i}_{MB} \cdot (A \times \epsilon) \cdot BR_{\rm J/\psi \to \mu^{+}\mu^{-}} \cdot \sigma^{pp}_{\rm J/\psi}} \tag{5.9}$$

where $N^{i}_{\rm J/\psi}$ is the number of ψ(2S) obtained from the signal extraction for multiplicity bin i, N^{i}_{MB} is the number of minimum bias events and it is obtained by multiplying normalization factor with the number of CMUL7 trigger in the corresponding multiplicity bin i, while $< T^{i}_{pPb} >$ is the average nuclear overlap function.

The $Q_{\rm pPb}$ values as a function of centrality are tabulated in Table 5.21 in the rapidity range $2.03 < y < 3.53$ in 6 centrality bins, and in Table 5.22 for the range $-4.46 < y < -2.96$.

Table 5.21: $Q_{\rm pPb}$ values of ψ(2S) at $\sqrt{s_{\rm NN}}$ = 8.16 TeV in p–Pb collisions in different centrality bins. The first uncertainty is statistical, the second is the uncorrelated systematic while the third one is the correlated systematic.

	$Q_{\rm pPb} \pm stat \pm syst$ [$2.03 < y < 3.53$]
2-10%	0.8580 ± 0.1590 (18.5%) ± 0.0960 (11.2%) ± 0.0867 (10.1%)
10-20%	0.5140 ± 0.1440 (28.0%) ± 0.0525 (10.2%) ± 0.0520 (10.1%)
20-40%	0.4710 ± 0.1070 (22.7%) ± 0.0440 (9.3%) ± 0.0476 (10.1%)
40-60%	0.6190 ± 0.1190 (19.2%) ± 0.0605 (9.8%) ± 0.0626 (10.1%)
60-80%	0.6970 ± 0.1460 (20.9%) ± 0.0820 (11.8%) ± 0.0705 (10.1%)
80-90%	1.0650 ± 0.2710 (25.4%) ± 0.0949 (8.9%) ± 0.1076 (10.1%)

Table 5.22: Q_{pPb} of ψ(2S) at $\sqrt{s_{\mathrm{NN}}}$ = 8.16 TeV in Pb-p collisions in centrality bins. The first uncertainty is statistical, the second is the uncorrelated systematic while the third one is the correlated systematic.

	$Q_{\mathrm{pPb}} \pm stat \pm syst$ $[-4.46 < y < -2.96]$
2-10%	1.0170 ± 0.1970 (19.4%) ± 0.0923 (9.1%) ± 0.1057 (10.4%)
10-20%	0.5800 ± 0.1730 (29.8%) ± 0.0529 (9.1%) ± 0.0603 (10.4%)
20-40%	0.7420 ± 0.1230 (16.6%) ± 0.0774 (10.4%) ± 0.0771 (10.4%)
40-60%	0.5160 ± 0.1260 (24.4%) ± 0.0498 (9.7%) ± 0.0536 (10.4%)
60-80%	0.4500 ± 0.1310 (29.1%) ± 0.0549 (12.2%) ± 0.0468 (10.4%)
80-90%	0.6520 ± 0.2260 (34.7%) ± 0.0642 (9.8%) ± 0.0678 (10.4%)

Comparison with theory

The comparison with theoretical calculations have been shown in Fig. 5.34 and Fig. 5.35 for p–Pb and Pb–p collisions, respectively.

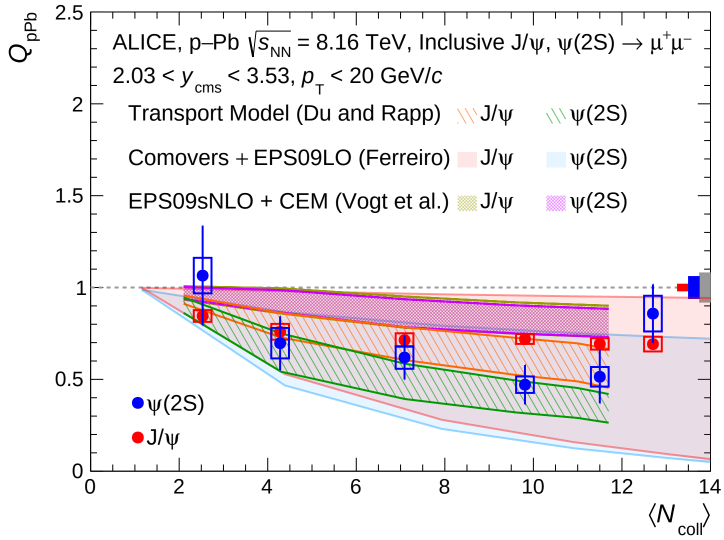

Figure 5.34: Q_{pPb} of ψ(2S) and J/ψ compared with theory in p-Pb collisions [29, 31, 32]. The box in red around unity represents the J/ψ global systematic, in blue the $\psi(2S)$ one and in gray the global systematic shared between J/ψ and $\psi(2S)$.

At forward rapidity, the suppression behavior of ψ(2S) as a function of centrality is similar to that for the J/ψ. But at backward rapidity, a systematically stronger suppression of the ψ(2S) relative to the J/ψ is visible, except for the most peripheral and most central collisions, where the large uncertainties in the results do not allow us to reach a firm conclusion. The centrality dependence of ψ(2S) Q_{pPb} at $\sqrt{s_{\mathrm{NN}}}$ =

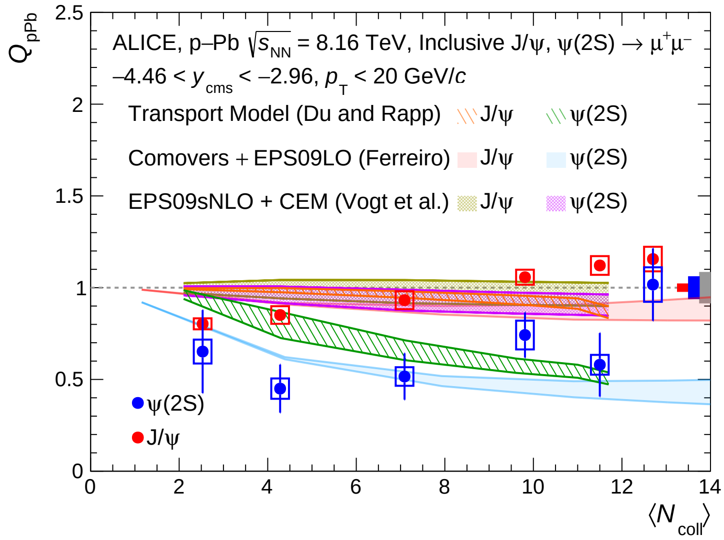

Figure 5.35: Q_{pPb} of ψ(2S) and J/ψ compared with theory in Pb-p collisions [29, 31, 32]. The box in red around unity represents the J/ψ global systematic, in blue the $\psi(2S)$ one and in gray the global systematic shared between J/ψ and $\psi(2S)$.

8.16 TeV shows a similar trend to that at $\sqrt{s_{\mathrm{NN}}} = 5.02$ TeV. The EPS09s NLO + CEM calculations [31] predict a similar Q_{pPb} for both ψ(2S) and J/ψ. However, the model fails to describe ψ(2S) results at forward rapidity, while the J/ψ results lie near the lower limit of the band. At backward rapidity, the model calculation is close to the J/ψ data, although it shows different centrality behavior. It again fails to describe the stronger ψ(2S) suppression. The transport model [32] calculations yield significantly smaller Q_{pPb} for the ψ(2S) than for the J/ψ, with the difference being more prominent at the backward rapidity, where this difference exhibits an increasing trend with increasing centrality. The description of the forward rapidity results is fairly good for both J/ψ and ψ(2S). At backward rapidity, the model overestimates the ψ(2S) result in the most peripheral centrality bins. This model considers lower Q_{pPb} for the ψ(2S) than for the J/ψ caused due to a larger suppression of the ψ(2S) in the short QGP and the hadron resonance gas phases. Finally, the Comovers + EPS09LO model [31] gives a significantly lower Q_{pPb} for the ψ(2S) than for the J/ψ in the backward rapidity region. However, at the forward rapidity, the model uncertainties are too large to draw any firm conclusion.

To summarize, we can safely say that the effect of the comovers, responsible for the stronger suppression of the $\psi(2S)$ compared to the J/ψ and is dominant at backward rapidity due to the larger density of comovers in the Pb-going direction [28]. This model gives a good description of $\psi(2S)$ Q_{pPb} at backward rapidity. However, the trend with centrality shown for the J/ψ does not reproduce the one found in the data.

Thus, only the models, which include the final-state interactions are able to describe, at least qualitatively, the stronger suppression of $\psi(2S)$ than of the J/ψ in p–Pb collisions at LHC.

Bibliography

[1] ALICE collaboration, JHEP 12 (2014) 073.

[2] Adam et al., JHEP 06 (2016) 050.

[3] LHCb collaboration, JHEP 03 (2016) 133.

[4] CMS collaboration, Phys. Lett. B 790 (2019).

[5] ATLAS collaboration, Eur. Phys. J. C78 (2018) 3.

[6] Ma et al., Phys. Rev. C97 (2018) 1.

[7] Ferreiro E., Phys. Lett. B749 (2015).

[8] Du et al., Nucl. Phys. A943 (2015).

[9] PHENIX collaboration, Phys. Rev. C95 (2017) 3.

[10] ALICE Collaboration, B. Abelev et al., "Measurement of quarkonium production at forward rapidity in pp collisions at $\sqrt{s} = 7$ TeV", Eur. Phys. J. C74 no. 8, (2014) 2974, arXiv:1403.3648.

[11] https://arxiv.org/pdf/1509.08258.pdfhttps://arxiv.org/pdf/1509.08258.pdf, page 8.

[12] ALICE Collaboration, S. Acharya et al., "Energy dependence of forward-rapidity J/ψ and ψ(2S) production in pp collisions at the LHC", Eur. Phys. J. C77 no. 6, (2017) 392, arXiv:1702.00557.

[13] Y.-Q. Ma, K. Wang, and K.-T. Chao,"J/ψ(ψ(2S)) production at the Tevatron and LHC at ($\alpha_s^4 v^4$) in nonrelativistic QCD,"Phys.Rev.Lett.106(2011)042002

[14] Y.-Q. Ma and R. Venugopalan, "Comprehensive Description of J/ψ Production in Proton-ProtonPhys.Rev.Lett.113no.19,(2014)192301 Collisions at Collider Energies,"

[15] ALICE collaboration, Eur. Phys. J. 77 (2017) 6.

[16] ALICE collaboration, JHEP 07(2018)160.

[17] Ducloue et al., Phys. Rev. D.94 (2016) 074031.

[18] Albacete et al., Nucl. Phys. A972 (2018).

[19] Kusina et al., Phys. Rev. Lett. 121 (2018) 5.

[20] Eskola et al., JHEP 04 (2009) 065.

[21] Kovarik et al., Phys. Rev. D93 (2016) 8.

[22] Arleo et al., JHEP 10 (2014) 073

[23] ALICE Collaboration], "Centrality dependence of inclusive J/ψ production in p–Pb collisions at $\sqrt{s_{\mathrm{NN}}} = 5.02$ TeV", JHEP 1511 (2015) 127, arXiv:1506.08808.

[24] ALICE Collaboration, J. Adam et al., Centrality dependence of particle production in p-Pb collisions at $\sqrt{s_{\mathrm{NN}}}$= 5.02 TeV, Phys.Rev. C91 no. 6, (2015) 064905, arXiv:1412.6828.

[25] ALICE Collaboration], "Centrality dependence of ψ(2S) production in p–Pb collisions at $\sqrt{s_{\mathrm{NN}}} = 5.02$ TeV", JHEP 06 (2016) 050, arXiv:1603.02816.

[26] ALICE Collaboration, D. Adamova et al "J/ψ production as a function of charged-particle pseudorapidity density in p-Pb collisions at $\sqrt{s_{\mathrm{NN}}}$=5.02 TeV", Phys. Lett.B776(2018), arXiv:1704.00274.

[27] ALICE Collaboration, S. Acharya et al., “Search for collectivity with azimuthal J/ψ-hadron correlations in high multiplicity p–Pb collisions at $\sqrt{s_{\rm NN}}$=5.02 and 8.16 TeV”, Phys. Lett.B780645 (2018), arXiv:1709.06807.

[28] E. G. Ferreiro, “Excited charmonium suppression in protonnucleus collisions as a consequence of comovers”, Phys. Lett. B749 (2015) 98103, arXiv:1411.0549.

[29] J. L. Albacete et al., “Predictions for p+Pb Collisions at $\sqrt{s_{NN}}$ = 5 TeV: Comparison with Data”, Int. J. Mod. Phys. E 25 no. 9, (2016) 1630005, arXiv:1605.09479.

[30] J. L. Albacete et al., “Predictions for Cold Nuclear Matter Effects in p+Pb Collisions at $\sqrt{s_{\rm NN}}$ = 8.16 TeV”, Nucl. Phys. A972 (2018), arXiv:1707.09973.

[31] D. C. McGlinchey, A. D. Frawley, and R. Vogt, “Impact parameter dependence of the nuclear modification of J/ψ production in d+Au collisions at $\sqrt{s_{\rm NN}}$ = 200 GeV”, Phys. Rev. C87 no. 5, (2013) 054910, arXiv:1208.2667.

[32] X. Du and R. Rapp, “Sequential Regeneration of Charmonia in Heavy-Ion Collisions”, Nucl. Phys. A943 (2015), arXiv:1504.00670.

CHAPTER 6

J/ψ and ψ(2S) production in Pb–Pb collisions at $\sqrt{s_{\mathrm{NN}}}$ = 5.02 TeV

In this chapter we shall discuss two separate analyses on multi-differential J/ψ cross-section (first two sections) and single differential ψ(2S) cross-section.

I participated in the analysis of double differential R_{AA} of J/ψ and reproduced the analysis results presented in this thesis. The signal extraction, Monte Carlo simulations, evaluation of the acceptance $\times$ efficiency, evaluation of pp cross section for reference, estimation of experimental uncertainties, evaluation of triple differential R_{AA} of J/ψ and R_{AA} of ψ(2S) have been done as a part of this thesis work.

Double-differential R_{AA} of J/ψ studies

Motivation

In the present study, the J/ψ production as measured by ALICE in Pb–Pb collisions at $\sqrt{s_{\mathrm{NN}}}$ = 5.02 TeV, at the forward rapidity region ($2.5 < y < 4.0$), is discussed.

Over the past decades, the J/ψ production in heavy-ion collisions has been studied at the SPS, RHIC and LHC, which cover a wide range of center-of-mass energies per nucleon pair ($\sqrt{s_{\rm NN}}$) beginning from about 17 GeV to 5.02 TeV.

Surprisingly, the observed suppression did not show the increasing trend with increasing collision energy contrary to the expectation of the color-screening scenario which becomes pronounced due to the rising temperature of the QGP. This may happen due to regeneration of J/ψ from the abundantly produced c$\bar{\rm c}$ pairs at higher temperatures. In order to have a closer look at the suppression-regeneration picture, extensive studies of the centrality, $p_{\rm T}$ and rapidity dependence of the J/ψ nuclear modification factor have to be carried out.

Data samples, event and track selection

The present analysis is carried out using the Pb–Pb data at a center of mass energy $\sqrt{s_{\rm NN}}$ = 5.02 TeV which was recorded in November 2015. We have analysed the pass1 datasets of AOD files. The data samples is further filtered to obtain the events within the centrality limit of 0-90 % by using the VZERO detector.

Signal extraction

As the ratio of the signal to background in data is very low at the edges of the signal functions, we have fixed the tail parameters of the fit function (CB2 and NA60) used to reproduce the shape of the signal. The sets of tail parameters were extracted from MC simulation. In the present analysis three sets of tail parameters are used extracting from the:

- embedding MC simulation where GEANT3 has been used as transport code.
- pure J/ψ simulation using the GEANT4 as the transport code.
- pp at $\sqrt{s}$= 13 TeV J/ψ analysis for the CB2, where fits are performed by letting

the tail parameters free.

Two functions have been chosen for fitting the background: a second to third order polynomial ratio (Pol2/Pol3) and an extended variable width Gaussian (VWG2). All the fits are performed in two mass ranges: [2.2,4.5] and [2.4,4.7] GeV/c^2. In total there 20 tests performed in each bin.

Event Mixing

Another approach for the signal extraction is done by using event-mixing technique. In this technique, the single muon low-p_{T} trigger threshold (CMSL7) dataset are combined together to reproduce the invariant mass distribution. Also, the invariant mass-distribution of like-sign muon-pairs (to get N^{++}_{Raw} and N^{--}_{Raw}) are obtained by analyzing the CMUL7 or CMLL7 triggered events. The dataset is divided into 9 centrality pools of event each of pool size 10 %. The event-mixing is then done by mixing the muons of similar events coming from the same centrality pool and same run (N^{+-}_{Mix}). The mixed dimuon invaraint mass spectra is then normalized by a normalization factor

$$F = \frac{\int_2^8 2R\sqrt{N^{++}_{Raw}N^{--}_{Raw}}dm}{\int_2^8 N^{+-}_{Mix}} \tag{6.1}$$

where, the Ns are the unlike-sign (+-) and like-sign (++ or $--$) spectra of the raw and mixed events and R is a detector related factor. The value of ‘R’ is around 1 in our integration range.

$$R = \frac{N^{+-}_{Mix}}{\sqrt{N^{++}_{Mix}N^{--}_{Mix}}} \tag{6.2}$$

After the normalization, the dataset in various centrality pools are merged. Finally, the normalized mix-spectrum is subtracted from the raw spectrum. The subtracted invariant mass spectrum is used for fitting with the combination of signal function and background function. The signal shape is fitted by using the same shapes as used for the direct fit, which are, CB2 and NA60. The background is fitted by exponential function for same mass ranges as direct fit.

We have split the data set into 9 centrality bins (10 % intervals) and 11 $p_{\rm T}$ bins for 0-90 % and 0-20 % centrality.

Example of fits using the two methods mentioned above, are shown in Fig. 6.1.

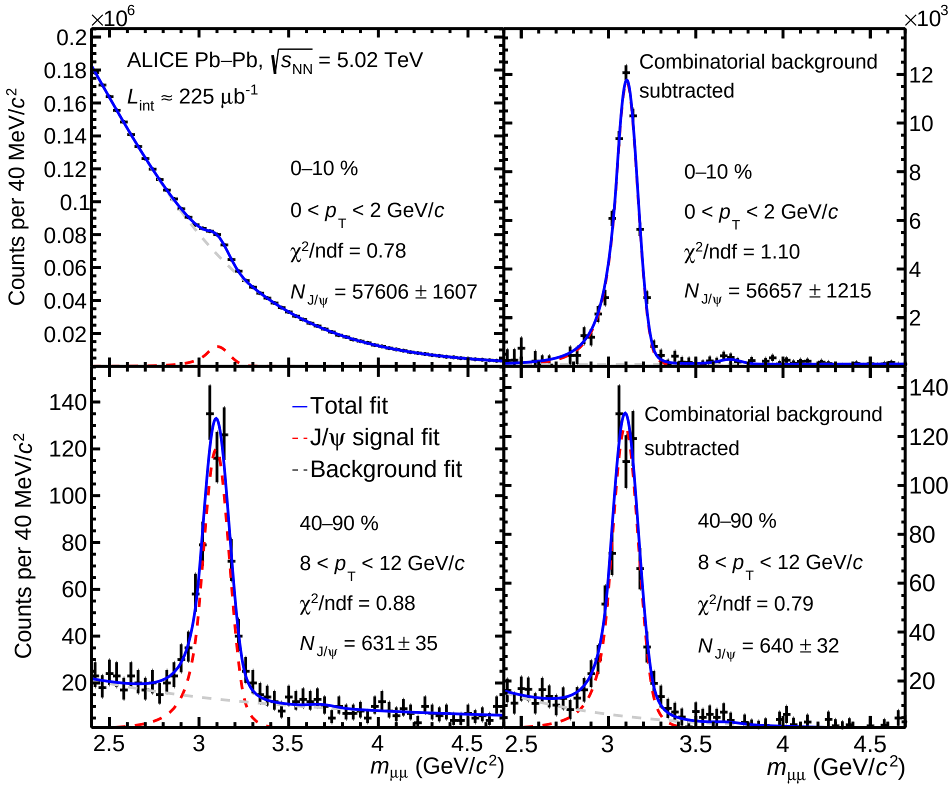

Figure 6.1: Typical fits to the dimuon invariant mass spectra for two centrality bins.

Acceptance-efficiency correction

In order to evaluate the J/ψ acceptance efficiency ($A \times \epsilon$) correction, the embedded Monte-Carlo data set has been used. To take care of the different trigger used in the simulation (CINT7-MUFAST-B) and signal analysis (CMUL7), following weightage has been applied :

- A weight proportional to number of CMUL7 trigger in each run for proper evalution of $A \times \epsilon$;

- A weight proportional to the number of reconstructed raw J/ψ in each centrality has been applied for correct evaluation of centrality-integrated $A \times \epsilon$;

- To take into account the centrality dependence of the input shapes of $A \times \epsilon$, a weight proportional to p_{T} and y distribution functions for J/ψ for given centrality bin are applied.

The weightage of p_{T} or y can be applied by fitting the $A \times \epsilon$ corrected data by J/ψ p_{T} or y input shapes in different centrality bins. These distribution functions are used as weights for the embedded data.

The outcome after re-weighting is shown in Fig. 6.2 for the bin $2.5 < y < 3.25$ and $3.25 < y < 4$. The ratios of the unweighted to the weighted $A.\epsilon$ are also plotted to show the effect of the weight quantitatively.

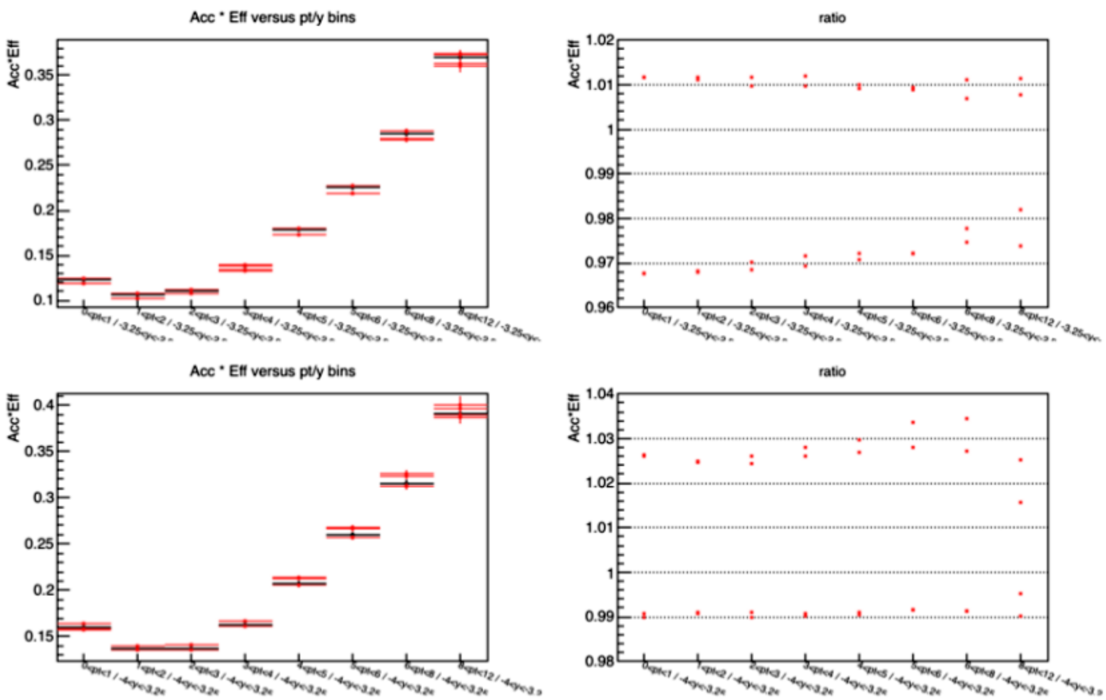

Figure 6.2: The $A \times \epsilon$ corrections for J/ψ as a function of p_{T} after re-weighting for rapidity ranges $2.5 < y < 3.25$ $(3.25 < y < 4)$ one the top left (bottom left) panel and their ratio over the central values on the right panel.

Systematics uncertainties

T_{AA} systematics

The values of the average nuclear overlap function $\langle T_{AA} \rangle$ used in this analysis were obtained using Glauber calculation. The value of $\langle T_{AA} \rangle$ only depends on the centrality and independent of p_{T} and y. Therefore, the systematic uncertainties in the 3 centrality bins vary from 3.2% to 4.5%.

Trigger systematics

The trigger response function (RF) has been calculated by taking the ratio of the Lpt (i.e. p_{T} threshold of 1 GeV/c) and Allpt (i.e. p_{T} threshold of 0.5 GeV/c) of single muon p_{T} distribution. The ratio of the number of J/ψ using Lpt/Allpt muon distributions from Data over MC versus p_{T} is shown in Fig. 6.3.

The trigger response has been measured both for raw and simulated data set as a function of single muon p_{T} by dividing them into 6 η bins to check rapidity dependence. The trigger response function for η is shown in Fig. 6.4. The trigger response function is then fitted with a sigmond function and the parameters are evaluated for both. The weight is then applied to both the monte-carlo and raw data set. The number of J/ψ is estimated for the data and monte-carlo by applying this weight factor. The difference between number of J/ψ in two cases gives the trigger systematics.

Sytematic on centrality limits

The systematic uncertainty on the centrality limits are determined by comparing the number of J/ψ in different centrality estimator in various centrality bins. The estimated systematics vary from 0.2 to 1.4 % for three centrality bins of 0-20, 20-40

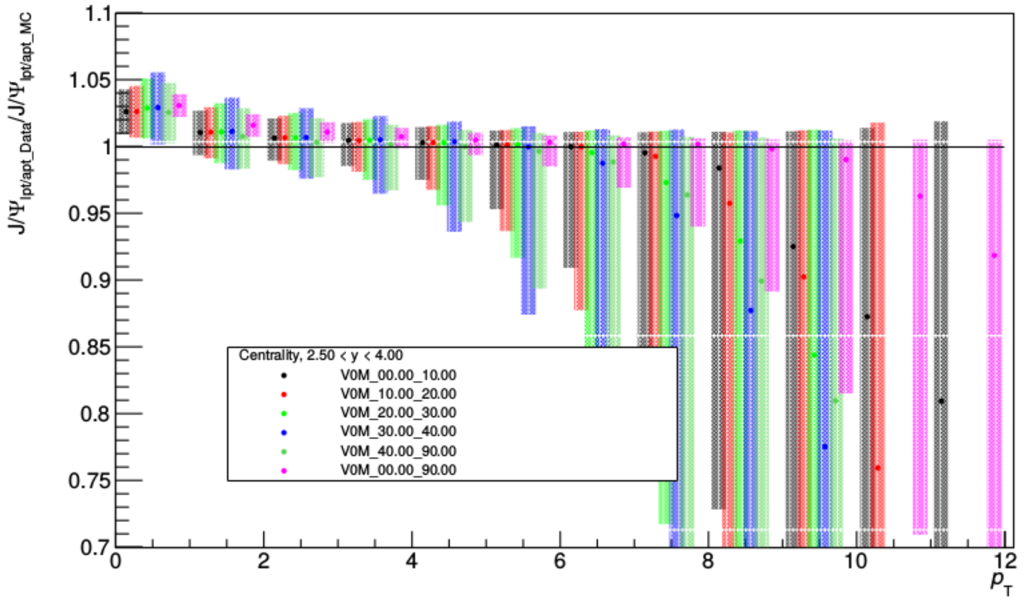

Figure 6.3: The ratio of the number of J/ψ using Lpt/Allpt muon distributions from data over MC versus p_{T} for each centrality and integrated in y.

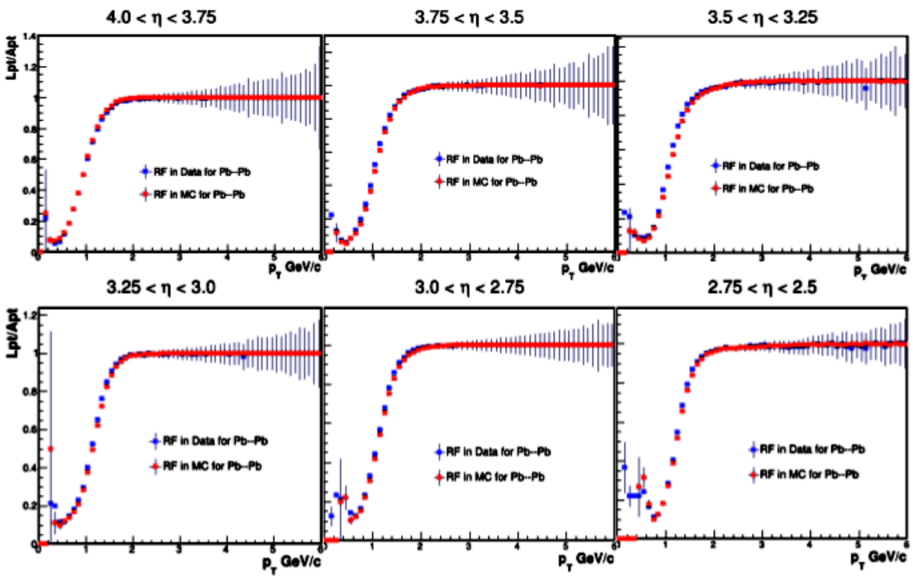

Figure 6.4: Response function distributions in MC (red) and in data (blue) obtained for several pseudo-rapidity ranges.

and 40-90 %.

Results on Single and Double-differential R_{AA}

The nuclear modification factor R_{AA} has been calculated through the following:

$$R_{\mathrm{AA}}^{\mathrm{J}/\psi} = \frac{N_{\mathrm{J}/\psi}}{\langle T_{\mathrm{AA}} \rangle \ . \ N_{\mathrm{MB}} \ . \ (A \times \varepsilon)_{\mathrm{J}/\psi} \ . \ \mathrm{BR}_{\mathrm{J}/\psi \to \mu^+\mu^-} \ . \ \sigma^{\mathrm{pp}}_{\mathrm{J}/\psi}} \tag{6.3}$$

where $N_{\mathrm{J}/\psi}$ is the number of J/ψ obtained from the signal extraction in a kinematic region, $\mathrm{BR}_{\mathrm{J}/\psi \to \mu^+\mu^-}$ is the branching ratio of J/ψ in dimuon decay channel = (5.96±0.03)%, N_{MB} is Number of minimum bias events in the kinematic region, $\langle T_{\mathrm{AA}} \rangle$ is the average of the nuclear overlap function in the corresponding centrality bin, $\sigma^{\mathrm{pp}}_{\mathrm{J}/\psi}$ is the inclusive J/ψ cross section for pp collisions at the same energy.

The Fig. 6.5 shows the rapidity dependence of R_{AA} for integrated centrality range 0-90%. The result is also compared with the observation found at the centre of mass energy 2.76 TeV. At both the energies, there is no rapidity dependence in R_{AA}. The transport model gives a flat prediction for the R_{AA} values in those bins.

The Fig. 6.6 shows the rapidity dependence of R_{AA} for differential centrality bins 0-20%, 20-40% and 40-90%. The slope of the R_{AA} does not change even in differential centrality bins. This can also be confirmed by the transport model.

Discussion

Looking at the double-differential R_{AA}, it is seen that the rapidity dependence of R_{AA} in central collision is same as in peripheral collision and also over centrality 0-90% range. Thus, the effect of regeneration/recombination probably gets washed out if we integrate over the full centrality range. Thus, a triple-differential R_{AA} study is needed to investigate this aspect further.

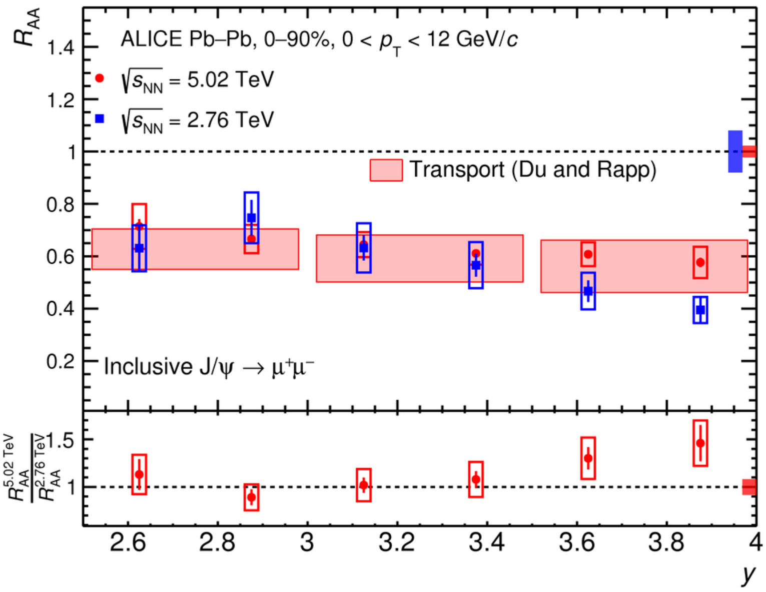

Figure 6.5: R_{AA} as a function of y for integrated p_{T} and centrality. The error bar and the box represent to statistical and systematic uncertainties. The model predictions are depicted by shaded boxes. The correlated global syatematic uncertainties are represented by the filled boxes around 1.

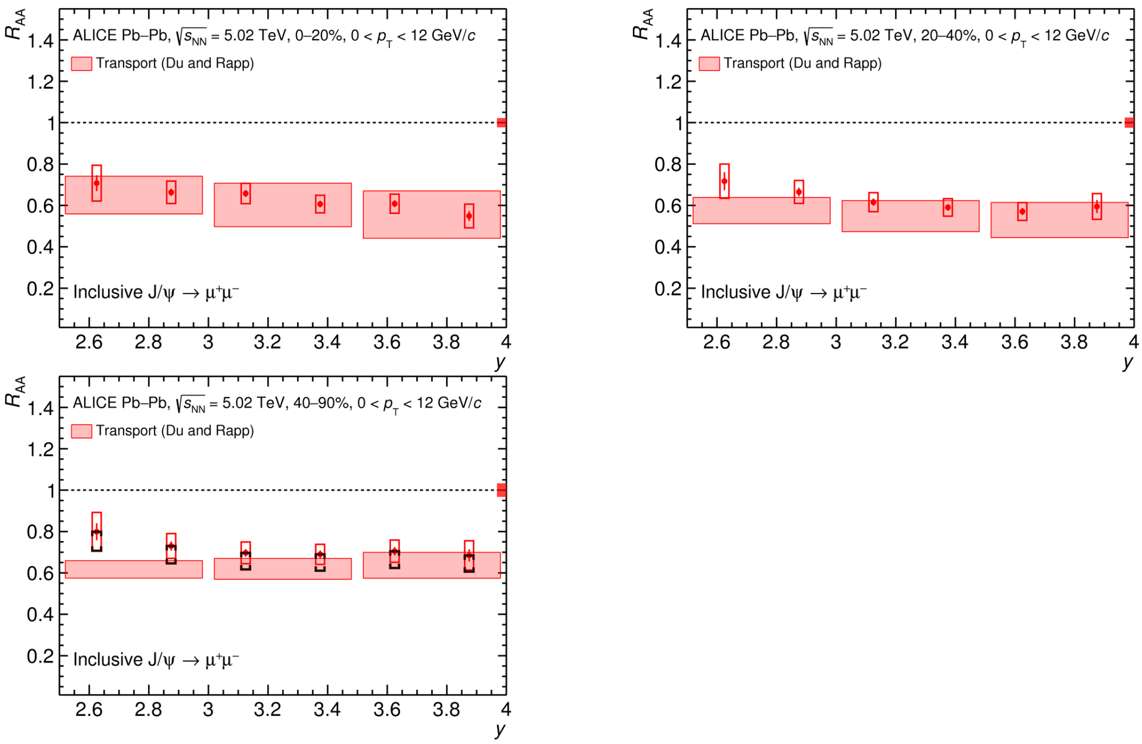

Figure 6.6: The R_{AA} as a function of y for different centrality ranges.

Triple-differential $R_{\rm AA}$ of J/ψ studies

Need for triple-differential analysis

In the last section we observed that, the rapidity dependence of $R_{\rm AA}$ in central collision is same as in the peripheral collision and over centrality 0-90% range. However, the regeneration contribution should favor low-$p_{\rm T}$ J/ψ, as the bulk of the thermalized charm quarks present in the medium, have small momenta.

As the number of partons produced at mid-y is more than at forward-y, the in-medium effect due to this, should induce a slope in $R_{\rm AA}$ vs y plot, for low-$p_{\rm T}$ and central collisions. Thus, the triple differential $R_{\rm AA}$ estimation is necessary.

The J/ψ nuclear modification factor $R_{\rm AA}$ has been measured as a function of rapidity in different $p_{\rm T}$ (0-2 GeV/c, 2-4 GeV/c, 4-6 GeV/c and 6-12 GeV/c) and centrality bins (0-20 %, 20-40 % and 40-90 %).

Data samples, event and track selection

The present analysis is carried out using Run-2 Pb–Pb data at a center of mass energy $\sqrt{s_{\rm NN}}$ = 5.02 TeV which was recorded in November 2015 and 2018 for an integrated luminosity of 250 and 530 pb^{-1}, respectively. We have used both pass3 of AOD files for LHC18q and LHC18r periods.

The data samples is further filtered to obtain the events within the centrality limit of 0-90 % by using the VZERO detector.

The Fig.6.7 shows the comparison plot for the two periods 2015 and 2018. In this figure each dimuon invariant mass spectra is normalized by the number of CMUL trigger. It is observed that the dimuon invariant mass distribution in the J/ψ mass

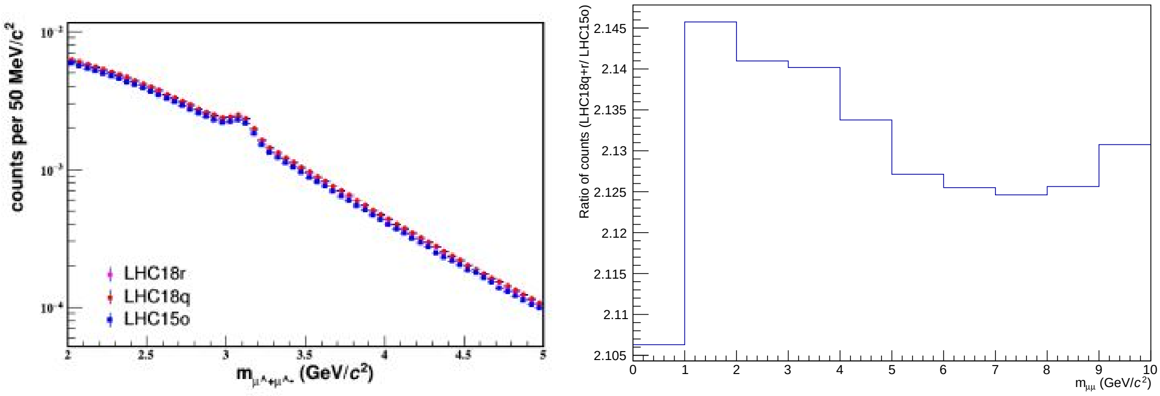

Figure 6.7: The dimuon invariant mass spectra for 2015 and 2018 datasets, normalized by the CMUL trigger (left) and their ratio (right).

region is similar for both 2015 (LHC15o) and 2018 (LHC18q and LHC18r). It has been observed that the mass, width and the significance is almost stable. The ratio of the invariant mass spectra of the two periods are almost constant. This helps to understand the similarity in datasets between the two periods. Therefore, the two data samples can be merged together. The results in this analysis is based on this merged sample of 2015+2018. This was necessary to carry out the triple differential study.

Signal extraction and Event Mixing

The procedures of signal extraction and event mixing are the same as described in the previous section.

Acceptance-efficiency correction

In order to calculate the J/ψ acceptance efficiency ($A \times \epsilon$) correction, the embedded Monte-Carlo data sample for 2015 and 2018 are merged at the histogram level and then the analysis has been performed. The run-by-run $A \times \epsilon$ of the merged dataset is shown in Fig. 6.8.

The same weightages have been applied as stated before.

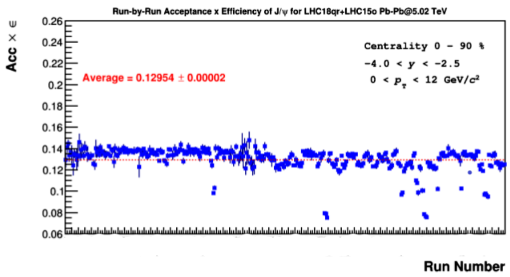

Figure 6.8: The $A \times \epsilon$ of J/ψ for the 2015+2018 datasets.

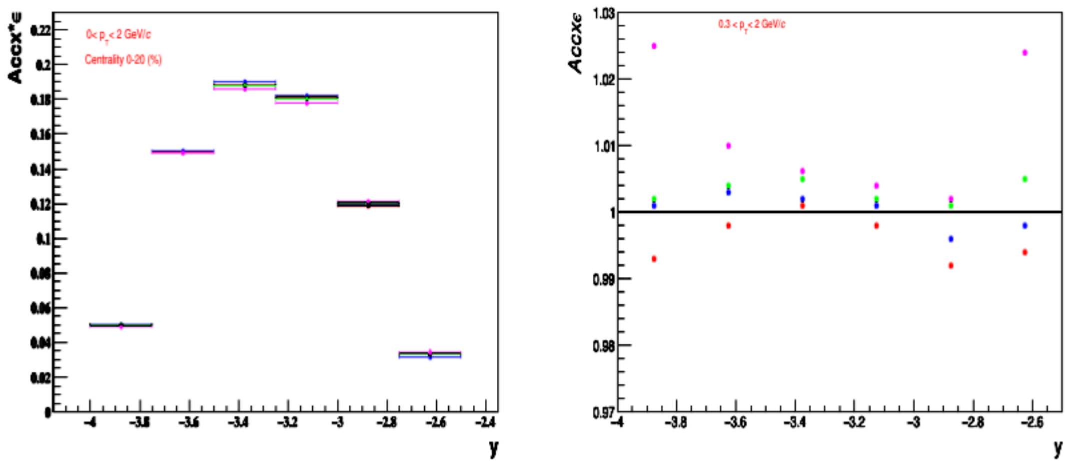

Figure 6.9: The $A \times \epsilon$ of J/ψ as a function of y after re-weighting for $0.3 < p_{\mathrm{T}} < 2$ GeV/c is shown in left panel and their ratio over the central values on the right panel.

Examples of the $A \times \epsilon$ after the re-weighting, are shown in Fig. 6.9 for the centrality and rapidity differential bins in $0.3 < p_{\mathrm{T}} < 2$ GeV/c range. Their ratios with the central values are also plotted in the same figure.

Systematics uncertainties

The systematic uncertainties for the triple differential analysis have been estimated following the method used for double differential analysis discussed in the previous section. The values of systematic uncertainties for the present analysis are listed below.

$T_{\rm AA}$ systematics

The $T_{\rm AA}$ systematic uncertainties in the 3 centrality bins vary from 3.2% to 4.5%.

Trigger systematics

This systematics vary from 0-4% in various bins.

Sytematic on centrality limits

The systematics show a variation of 0.2 to 1.4% for three centrality bins of 0-20%, 20-40% and 40-90%.

Results

The $R_{\rm AA}$ has been measured as a function of rapidity in four $p_{\rm T}$ bins, 0.3-2 Gev/c, 2-4 GeV/c, 4-6 GeV/c and 6-12 GeV/c. These results are evaluated in 3 centrality bins, 0-20 %, 20-40 % and 40-90 %. These results are shown in Fig 6.10, 6.11, 6.12. If there is no in-medium effect on J/ψ, then there will be no change in slope in Pb–Pb. But if there is in-medium production of J/ψ, then it will induce a slope in $R_{\rm AA}$ vs y plot. This effect is visible in Fig. 6.10 for $0.3 < p_{\rm T} < 2$ GeV/c.

Discussion

The slope of $R_{\rm AA}$ as a function of rapidity diminishes from the low $p_{\rm T}$ to high $p_{\rm T}$ bins in the most central collision, which is a clear indication of recombination in the medium. This is because the recombination effect is prominent only at low-$p_{\rm T}$. It is interesting to note that the slope is negligible for non-central collisions. This is also consistent as these collisions produce less number of $c\bar{c}$ pairs and thus

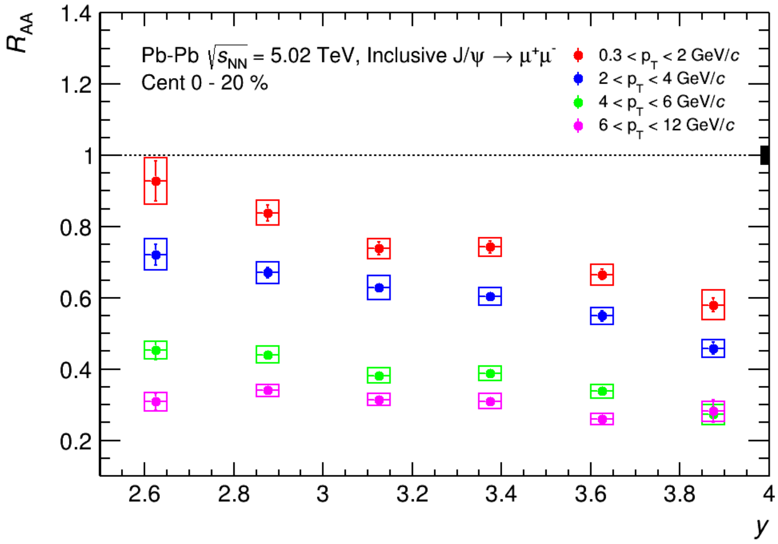

Figure 6.10: $R_{\rm AA}$ as a function of rapidity measured at $\sqrt{s_{\rm NN}}$ = 5.02 TeV for centrality 0 - 20% in $p_{\rm T}$ ranges 0.3-2 GeV/c, 2-4, 4-6 and 6-12 GeV/c. The statistical uncertainties are represented by the error bar whereas box represents the uncorrelated systematic uncertainties around the data points. The correlated global systematic uncertainties are represented by the filled boxes around 1.

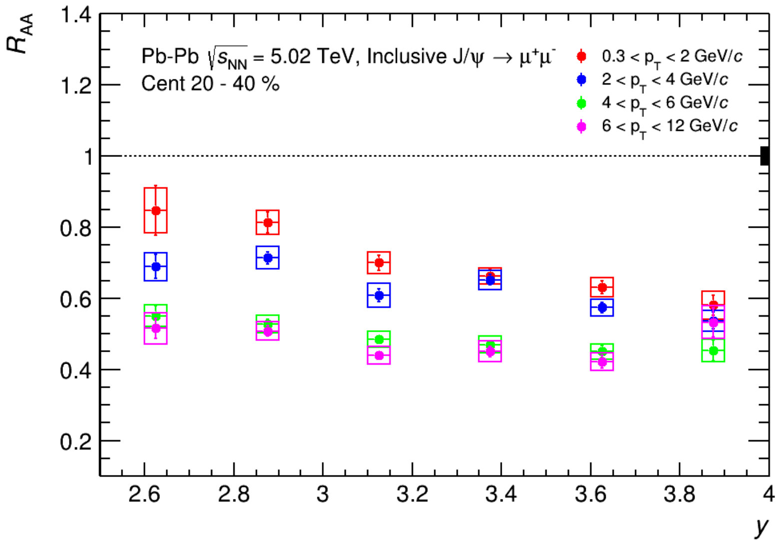

Figure 6.11: $R_{\rm AA}$ as a function of rapidity measured at $\sqrt{s_{\rm NN}}$ = 5.02 TeV for centrality 20-40% in $p_{\rm T}$ ranges 0.3-2 GeV/c, 2-4, 4-6 and 6-12 GeV/c. The statistical uncertainties are represented by the error bar whereas box represents the uncorrelated systematic uncertainties around the data points. The correlated global systematic uncertainties are represented by the filled boxes around 1.

the recombination effect is small and for the peripheral collisions the $R_{\rm AA}$ becomes independent of y. This effect was hidden in the double-differential results. The higher statistics in the 2018 datasets made it possible to establish the recombination

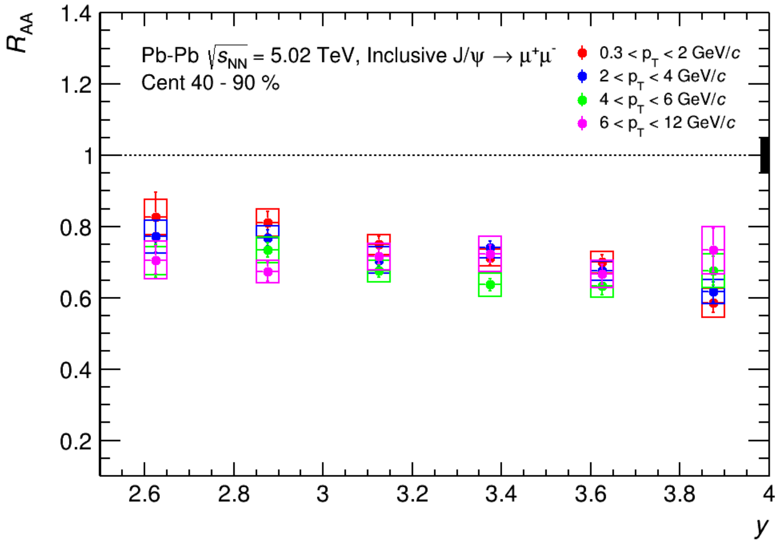

Figure 6.12: $R_{\rm AA}$ as a function of rapidity measured at $\sqrt{s_{\rm NN}}$ = 5.02 TeV for centrality 40-90% in $p_{\rm T}$ ranges 0.3-2 GeV/c, 2-4, 4-6 and 6-12 GeV/c. The statistical uncertainties are represented by the error bar whereas box represents the uncorrelated systematic uncertainties around the data points. The correlated global systematic uncertainties are represented by the filled boxes around 1.

effect in Pb–Pb collisions, through the triple differential cross-section studies.

Single differential ψ(2S) studies

Motivation

At LHC energies, due to the large increase of the $\rm Q\overline{Q}$ production cross-section with the collision energy, there is a possibility of quarkonium production enhancement via recombination of Q and $\overline{\rm Q}$ [3,4]. Thus, this observation of quarkonium enhancement in Pb–Pb collisions via recombination also constitutes an evidence of QGP formation. In addition, since the binding energy of ψ(2S) is very less than the ground state J/ψ, ψ(2S) is expected to be more suppressed than J/ψ.

ALICE-MS has attempted to measure the suppression of ψ(2S) in Pb–Pb collisions at $\sqrt{s_{\rm NN}}$ = 2.76 TeV (Fig.6.13). But the low statistics did not allow a firm conclusion

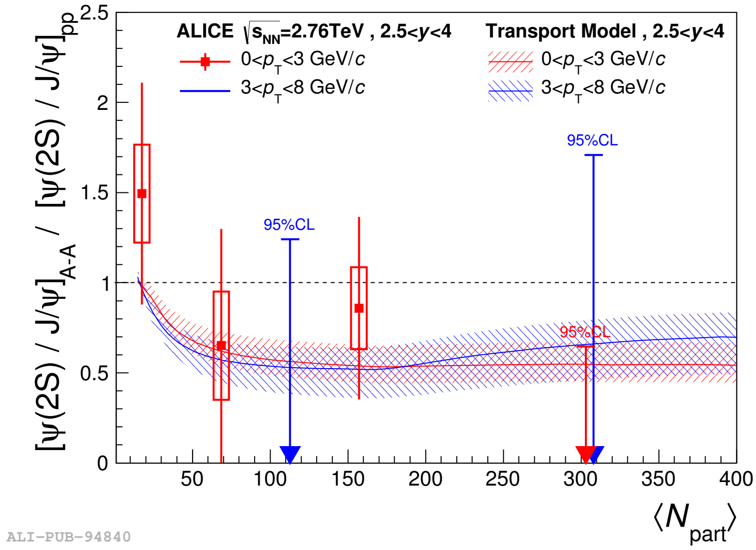

Figure 6.13: The double ratio ψ(2S) over J/ψ cross-sections in Pb–Pb collisions at $\sqrt{s_{\rm NN}}$ = 2.76 TeV.

since the statistical fluctuations inside one standard deviation allow data points to range between very low double ratios (strong ψ(2S) suppression with respect to J/ψ) to values higher than unity (less ψ(2S) suppression with respect to J/ψ).

Thus, the ALICE experiment at LHC has studied the inclusive ψ(2S) production at forward rapidity ($2.5 < y < 4.0$) in Pb-Pb collisions at $\sqrt{s_{\rm NN}}$ = 5.02 TeV with higher statistics using the Muon Spectrometer in the $\mu^+\mu^-$ decay channel. We will present the measurements of the nuclear modification factor ($R_{\rm AA}$) of inclusive ψ(2S) in the centrality and transverse momentum ($p_{\rm T}$) bins at forward rapidity. We will also present $R_{\rm AA}(\psi(2{\rm S}))/R_{\rm AA}({\rm J}/\psi)$ and yield ratio $\left[\frac{\psi(2{\rm S})}{{\rm J}/\psi}\right] = \frac{N_{\psi(2{\rm S})}}{N_{{\rm J}/\psi}} \times \frac{(A\times\varepsilon)_{{\rm J}/\psi}}{(A\times\varepsilon)_{\psi(2{\rm S})}}$ as a function of centrality and $p_{\rm T}$.

Normalization factor

We have collected data in the dimuon trigger (CMUL7-NOPF-B-MUFAST), so we need a normalization factor ($F_{\rm norm}$) to evaluate the number of equivalent minimum bias (MB) events, which is used in the calculation of the nuclear modification factor.

$$N_{MB}^{eq} = \sum_{runno} F_{norm}^{i} \times N_{MUL}^{i} \tag{6.4}$$

We have followed two different methods to calculate the F_{norm} and the calculations are done with pileup rejection cuts.

- Offline method: The F_{norm} for run number i is obtained from,

$$F_{norm}^{off,i} = PU^{i} \times \frac{MB^{i}}{MB\&0MUL^{i}}, \tag{6.5}$$

where MB is the number of physics selected (PS) minimum bias (MB) events, MB&0MUL is the sample of MB event containing also a 0MUL (Muon UnLike) input and PU is the pile-up correction factor associated to the MB trigger calculated as, $PU^{i} = \frac{\mu^{i}}{1-e^{-\mu^{i}}}$ with $\mu^{i} = -ln(1 - \frac{N_{MB}(PS,CENT) \times L0b_{MB}^{rate,i}}{N_{MB}(ALL,ALL) \times N_{colliding}^{i} \times f_{LHC}})$, where $L0b_{MB}^{rate,i}$ is the level 0 MB trigger scaler input, $N_{colliding}^{i}$ is the number of colliding bunches and f_{LHC} is the LHC frequency.

- Online method: In this method F_{norm} is obtained as,

$$F_{norm}^{scal,i} = PU^{i} \times \frac{F_{purity}^{MB} L0b_{MB}^{i}}{F_{purity}^{MUL} L0b_{MUL}^{i}}, \tag{6.6}$$

where F_{purity}^{MUL} is the purity factor associated to the unlike-sign dimuon trigger (CMUL7).

The average F_{norm} value for 0-90% is 13.06 $\pm$ 0.0073. The systematic uncertainty on F_{norm} calculation is 0.5%.

The number of equivalent MB events is obtained as $N_{\mathrm{MB}} = F_{\mathrm{norm}} \times N_{\mathrm{CMUL7}}$.

The proton-proton reference

To evaluate the J/ψ and ψ(2S) nuclear modification factor, the p-p reference, at the same energy and in the same kinematic domain as the Pb-Pb collisions, must be computed. The measurement of those cross-sections have been discussed in details in the chapter 4.

Signal extraction

The J/ψ and ψ(2S) yields have been obtained by fitting the unlike-sign (OS) dimuon mass spectrum, either before or after an event mixing procedure to remove the combinatorial background, with a combination of signal and background functions. For the J/ψ and ψ(2S) signals, two Extended Crystal Ball (CB2) functions or two so-called "NA60" functions have been used, while for the background a Variable Width Gaussian (VWG) function or a combination of a second to third order polynomial ratio (Pol2/Pol3) or a double exponential function (DE) have been adopted.

During the fit of the experimental invariant mass spectrum the amplitude, position and width of J/ψ for CB2 or NA60 were considered as free parameters. On the other hand, the position and the width of ψ(2S) were fixed by the following prescriptions:

- The mass position of ψ(2S) is fixed to the J/ψ one by the following relation:

$$m_{\psi(2S)} = m^{\mathrm{fit}}_{J/\psi} + \left(m^{PDG}_{J/\psi} - m^{PDG}_{\psi(2S)}\right). \tag{6.7}$$

  where, $m^{PDG}_{J/\psi}$ and $m^{PDG}_{\psi(2S)}$ are the masses of J/ψ and ψ(2S) from PDG.

- The width of ψ(2S) is fixed to the J/ψ one:

$$\sigma_{\psi(2S)} = \sigma^{\rm fit}_{J/\psi} . \frac{\sigma^{MC}_{\psi(2S)}}{\sigma^{MC}_{J/\psi}}. \tag{6.8}$$

where, $\sigma^{MC}_{J/\psi}$ and $\sigma^{MC}_{\psi(2S)}$ are the widths of J/ψ and ψ(2S) obtained from embedding Monte Carlo simulations.

The tail parameters for J/ψ were fixed to tail parameters obtained by fitting the shape of the resonance obtained from MC simulation. Other sets of tail parameters used are pp 13 TeV tails (tails extracted directly from the data in pp collisions at $\sqrt{s} = 13$ TeV) for CB2 only. The same tail parameters have been assumed for ψ(2S) as the resonances are separated by only 590 MeV/c^2. This implies that the energy straggling and multiple coulomb scattering effects of the front absorber on the decay muons are assumed to be similar. All the parameters of the VWG or Pol2/Pol3 or DE used for the fitting of the continuum background have been kept free.

The signals have been extracted in seven centrality bins: 0-90%, 0-10%, 10-20%, 20-30%, 30-40%, 40-60% and 60-90% integrated over $p_{\rm T}$ and y ($0 < p_{\rm T} < 12$ GeV/c and $2.5 < y < 4$) and in six $p_{\rm T}$ bins: 0-2, 2-3, 3-4, 4-5, 5-6, 6-12 GeV/c integrated over centrality and y (0-90% and $2.5 < y < 4$, respectively).

Direct fit

Fig. 6.14 shows the signal extraction in the seven centrality bins integrated over $p_{\rm T}$ and y while Fig. 6.15 shows the signal extraction in six $p_{\rm T}$ bins integrated over centrality and y.

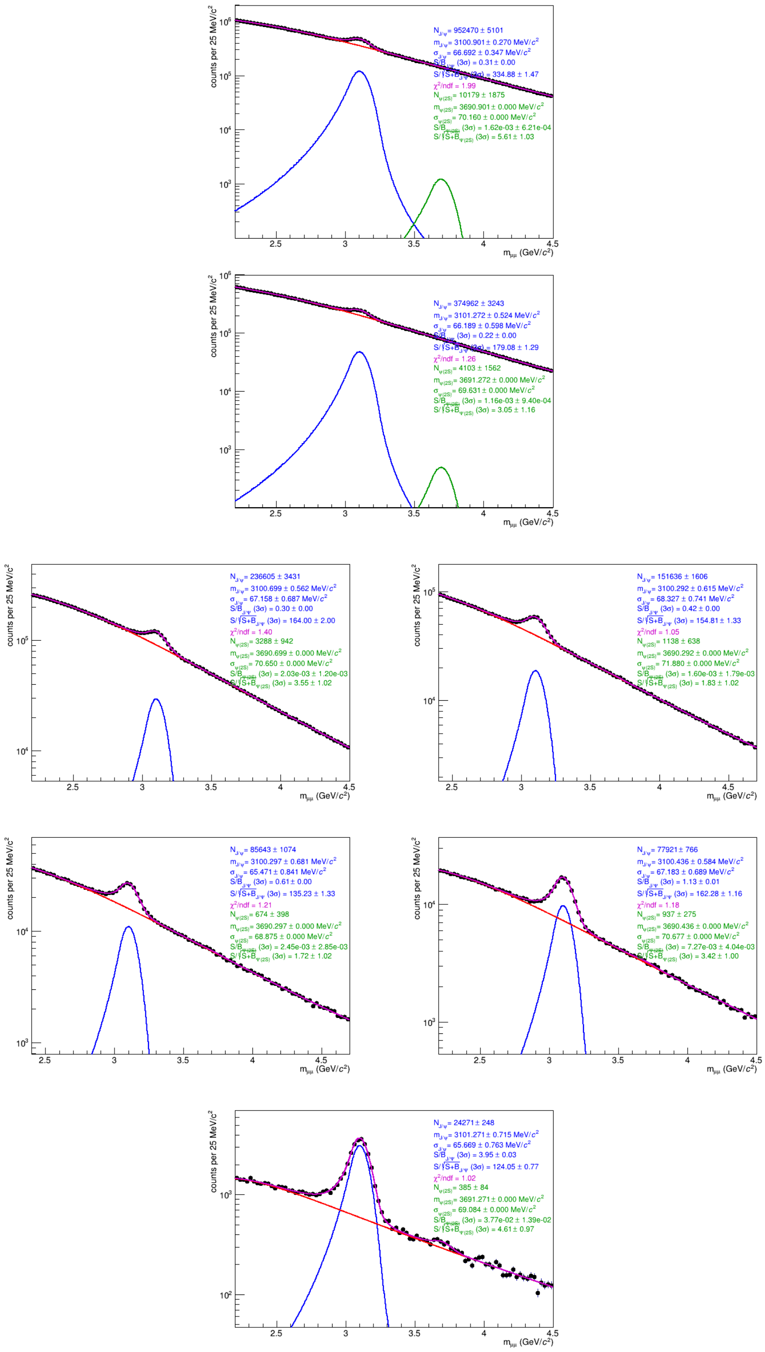

Figure 6.14: Typical fits of the invariant mass spectra in Pb–Pb collisions in seven centrality bins for $0 < p_{\rm T} < 12$ GeV/c and $2.5 < y < 4$

Event mixing

Since the CMLL trigger is downscaled, the OS and LS raw data dimuon pairs from CMLL&!CMUL triggered events are weighted by the inverse of the downscaling

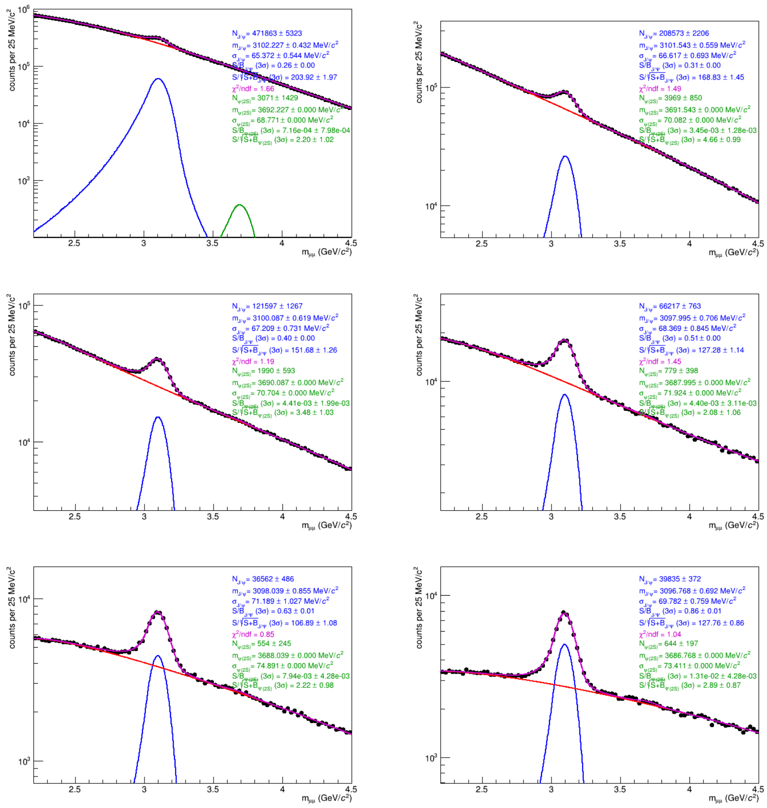

Figure 6.15: Typical fits of the invariant mass spectra in Pb–Pb collisions in six p_{T} bins for 0-90% and $2.5 < y < 4$.

factor. After subtraction of the uncorrelated background by the event-mixing technique, the residual mass spectra are fitted with a sum of two functions, a signal shape and a background shape.

Dimuon mass distributions for Raw and Mixed events for 0-10% centrality is shown in Fig. 6.16.

Systematic uncertainties in signal extraction

For each of the signal extraction techniques (direct fit or event mixing), several tests are done using different functions for the signal and background descriptions on different mass ranges and tail parameter sets.

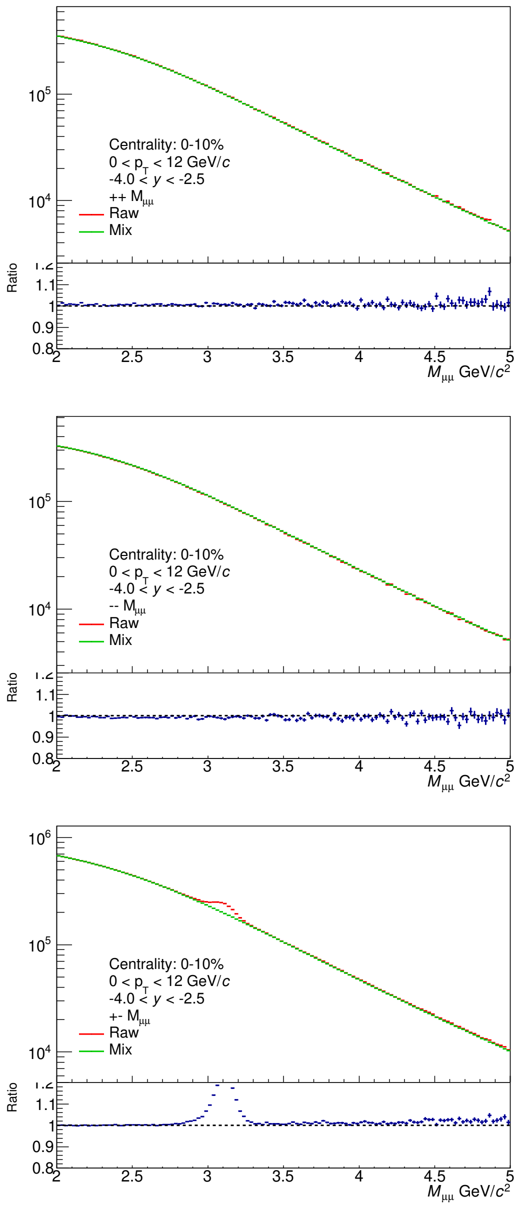

Figure 6.16: Like (++ and $--$, top and middle plots) and unlike (+-, bottom plot) sign dimuon mass distributions for Raw and Mixed events for 0-10% centrality.

For the direct fit, tests are built by combining:

- Two functions for the signal description : a CB2 and a NA60 functions
- Two functions for the background description : a VWG2 and a Pol2/Pol3 functions.
- Two invariant match ranges : $M_{\mu^+\mu^-} \in [2.2, 4.5]$ GeV/c^2 and $M_{\mu^+\mu^-} \in$

$[2.4, 4.7]$ GeV/c^2.

- Two ψ(2S) /J/ψ width ratios: 1.05 from embedding MC and 1.01 from pp at $\sqrt{s}$ = 13 TeV analysis.

Again, two sets of tails have been used for the signal functions:

- from the embedding MC simulation with embedding using GEANT3 transport code.
- from pp at $\sqrt{s}$ = 13 TeV J/ψ analysis for the CB2, where fits are performed by letting the tail parameters free.

leading to a total of 24 tests. Concerning the fits after event-mixing, the tests are built using :

- Two functions for the signal description : a CB2 or a NA60 functions.
- A double exponential function for the background description.
- Two invariant mass ranges : $M_{\mu^+\mu^-} \in [2.2, 4.5]$ GeV/c^2 and $M_{\mu^+\mu^-} \in [2.4, 4.7]$ GeV/c^2.
- Two ψ(2S) /J/ψ width ratios: 1.05 from embedding MC and 1.01 from pp at $\sqrt{s}$ = 13 TeV analysis.

The same sets of tails are used, leading to a total of 12 tests to be added to the 24 tests of the direct fit procedure. The results have been weighted such that fits with pp data tail parameters have the same weight as tests with MC tail parameters. The final extracted yield is the average of this 36 values, while the RMS of the distribution gives the systematic uncertainty on the signal.

Table 6.1 and 6.2 show the results on signal extraction of J/ψ and ψ(2S) in different centrality and $p_{\rm T}$ bins, respectively. The systematic varies from $\sim$ 2.4-9.2%.

Table 6.1: The number of J/ψ and ψ(2S) in different centrality bins

Centrality	$N_{\rm J/\psi}$	$N_{\psi(\rm 2S)}$
0–90%	929778 ± 4767 ± 22318	9538 ± 1738 ± 919
0–10%	364898 ± 3561 ± 10393	3709 ± 1309 ± 522
10–20%	229864 ± 2556 ± 5527	3258 ± 892 ± 250
20–30%	148223 ± 1695 ± 3452	1212 ± 592 ± 116
30–40%	83823 ± 988 ± 2183	661 ± 364 ± 44
40–60%	76081 ± 721 ± 1754	966 ± 262 ± 65
60–90%	23639 ± 228 ± 483	368 ± 77 ± 22

Table 6.2: The number of J/ψ and ψ(2S) in different $p_{\rm T}$ bins.

$p_{\rm T}$ GeV/c	$N_{\rm J/\psi}$	$N_{\psi(\rm 2S)}$
0–2	458874 ± 3654 ± 11779	2973 ± 1353 ± 512
2–3	198781 ± 1829 ± 7781	3804 ± 781 ± 374
3–4	118570 ± 1128 ± 3019	1906 ± 520 ± 119
4–5	65643 ± 741 ± 292	780 ± 354 ± 120
5–6	36603 ± 530 ± 482	613 ± 240 ± 54
6–12	39349 ± 400 ± 623	677 ± 203 ± 50

Acceptance × efficiency

A×ϵ has been calculated from the official embedding MC. We use embedding technique since the background is very important in Pb-Pb collisions. We embedded a MC charmonium in each minimum bias event in order to properly reproduce the occupancy of the detector. When averaging over run number and centrality a weight proportional to CMUL7 in each run has been added, in order to properly account for the run-by-run evolution of the Acceptance × efficiency.

The J/ψ input shapes have been tuned directly on the Pb-Pb at $\sqrt{s_{\rm NN}}$ = 5.02 TeV, through an iterative procedure. Same input shapes have been used for ψ(2S). As an example, the $A \times \varepsilon$ of ψ(2S) for each run using CMUL7 weightage are shown in Fig. 6.17, for the bin 0 < centrality < 10%.

Fig. 6.18, 6.19, 6.20 show the plots of the A×ϵ vs centrality, y and $p_{\rm T}$, respectively.

Table 6.3 summarizes the sources of various systematic uncertainties for ψ(2S) $R_{\rm AA}$. Asterisk correspond to correlated uncertainties as a function centrality or $p_{\rm T}$.

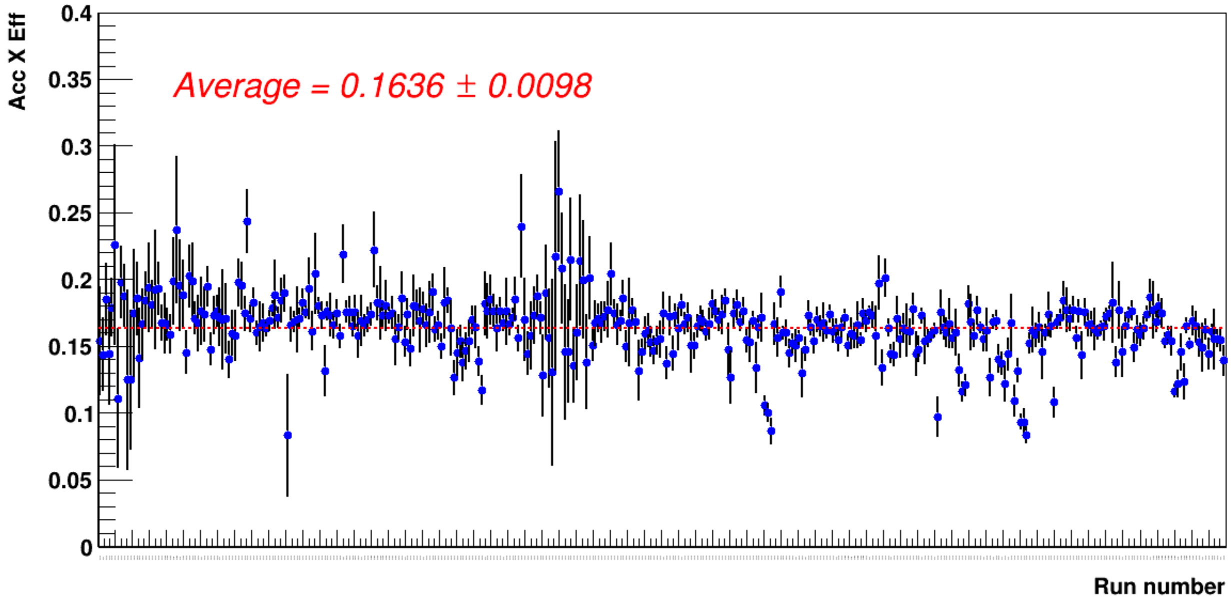

Figure 6.17: The $A \times \varepsilon$ of ψ(2S) (CMUL7 weighted) for each run for $0 <$ centrality $<$ 10%.

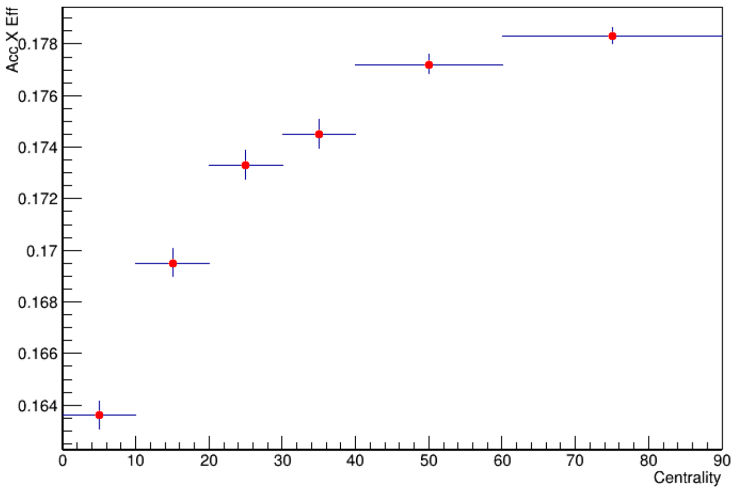

Figure 6.18: The A$\times\epsilon$ of ψ(2S) as function of centrality.

Results:

The nuclear effects affecting the production of ψ(2S) are studied using the nuclear modification factor R_{AA}, which is defined as the ratio of the production yields in Pb-Pb collisions to the production cross section in pp collisions scaled by the nuclear overlap function. R_{AA} is defined as:

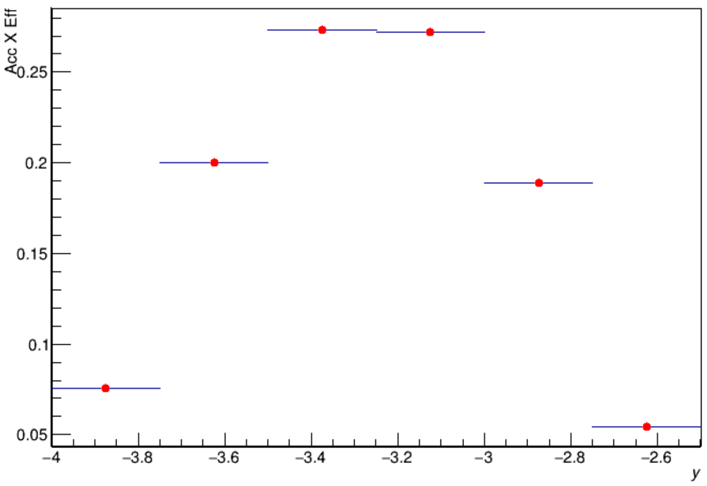

Figure 6.19: The A$\times\epsilon$ of ψ(2S) as function of y.

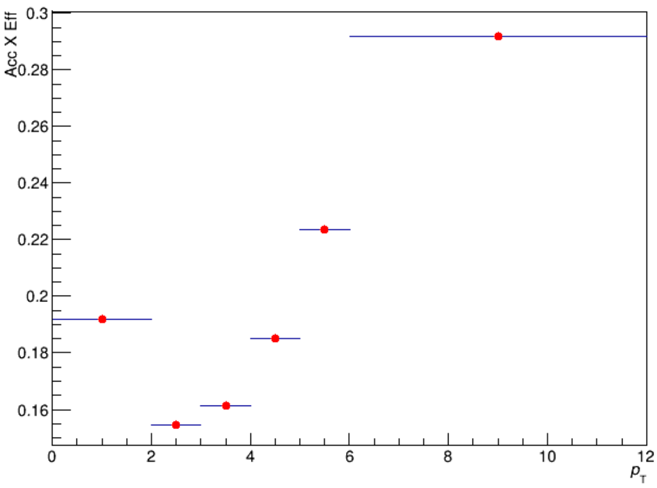

Figure 6.20: The A$\times\epsilon$ of ψ(2S) as function of $p_{\rm T}$.

$$R_{\rm AA}^{\psi(2S)} = \frac{N_{\psi(2S)}}{\langle T_{\rm AA}\rangle \ . \ N_{\rm MB} \ . \ (A\times\varepsilon)_{\psi(2S)} \ . \ {\rm BR}_{\psi(2S)\to\mu^+\mu^-} \ . \ \sigma^{\rm pp}_{\psi(2S)}} \tag{6.9}$$

where:

- $N_{\psi(2S)}$ is the number of ψ(2S) obtained from the signal extraction in the same kinematic region;
- $(A\times\varepsilon)_{\psi(2S)}$ is the product of the detector acceptance times the reconstruction

Table 6.3: Systematic uncertainties (in percentage) on the quantities associated to ψ(2S) R_{AA} measurement. Asterisk correspond to correlated uncertainties as a function of centrality or p_{T}.

Source	Integrated	vs centrality	vs p_{T}
Signal extraction	2.7-7.0	2.4-8.9	2.6-9.2
Trigger efficiency	3	3*	3
Tracking efficiency	3	3*	3
Matching efficiency	1	1*	1
MC input	3	3*	3
F_{norm}	0.5	0.5*	0.5*
$\langle T_{\mathrm{AA}} \rangle$	1	0.7-5.4	1*
Centrality	0.32	0.14-5.7	0.32*
pp reference (stat.+syst.)	13.2	13.2*	(18.6-36.5)+7.7*

efficiency for ψ(2S);

- $\mathrm{BR}_{\psi(2S)\to\mu^+\mu^-}$ is the branching ratio of ψ(2S) in dimuon decay channel = (0.8±0.06)%;
- N_{MB} is Number of minimum bias events in a kinematic region;
- $\langle T_{\mathrm{AA}} \rangle$ is the average of the nuclear overlap function in a centrality bin;
- $\sigma^{\mathrm{pp}}_{\psi(2S)}$ is the inclusive ψ(2S) cross section for pp collisions at the same energy.

With combined statistics of 2015 and 2018 Pb-Pb data at $\sqrt{s_{\mathrm{NN}}} = 5.02$ TeV it has been possible to calculate the R_{AA} of inclusive ψ(2S) as a function of centrality and p_{T}.

Centrality dependence of inclusive ψ(2S) R_{AA}

Fig. 6.21 shows inclusive ψ(2S) R_{AA} as a function centrality at $\sqrt{s_{\mathrm{NN}}} = 5.02$ TeV compared to the published J/ψ R_{AA} at the same energy. ψ(2S) shows a stronger suppression, in semi-central and central collisions, than the J/ψ one. Table 6.4 show the values of the R_{AA} for ψ(2S).

Table 6.5 shows the ratio of R_{AA} for ψ(2S) over that for J/ψ as a function of p_{T}.

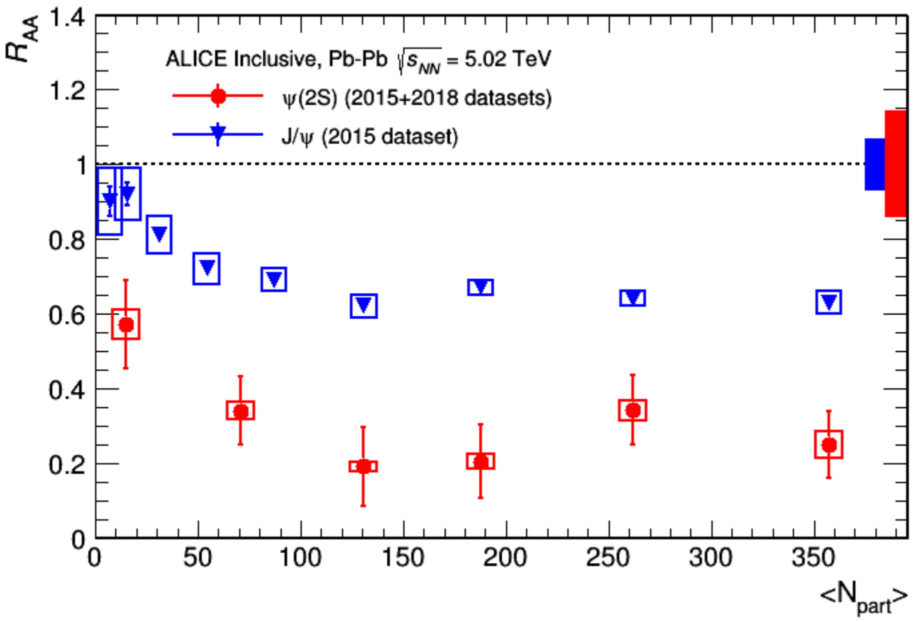

Figure 6.21: The inclusive ψ(2S) $R_{\rm AA}$ as a function centrality at $\sqrt{s_{\rm NN}} = 5.02$ TeV compared to the published J/ψ $R_{\rm AA}$ at the same energy. The boxes centered at $R_{\rm AA}$ = 1 represent the global uncertainties correlated over centrality.

Table 6.4: $R_{\rm AA}$ of ψ(2S) as a function of centrality in Pb–Pb collisions at $\sqrt{s_{\rm NN}}$ = 5.02 TeV.

Centrality	$R_{\rm AA}^{\psi(2S)}$
0-10%	0.249 ± 0.088 (stat 35.3%) ± 0.035 (syst 14.1%) + 0.035 (global 14.3%)
10-20%	0.340 ± 0.093 (stat 27.4%) ± 0.026 (syst 7.7%) + 0.048 (global 14.3%)
20-30%	0.203 ± 0.099 (stat 48.8%) ± 0.020 (syst 9.6%) + 0.029 (global 14.3%)
30-40%	0.190 ± 0.105 (stat 55.1%) ± 0.013 (syst 6.8%) + 0.027 (global 14.3%)
40-60%	0.339 ± 0.092 (stat 27.1%) ± 0.024 (syst 7.0%) + 0.048 (global 14.3%)
60-90%	0.571 ± 0.119 (stat 20.9%) ± 0.039 (syst 6.9%) + 0.082 (global 14.3%)

$p_{\rm T}$ dependence of inclusive ψ(2S) $R_{\rm AA}$

Fig. 6.22 shows inclusive ψ(2S) $R_{\rm AA}$ as a function $p_{\rm T}$ at $\sqrt{s_{\rm NN}}$ = 5.02 TeV. Table 6.6 show the values of ψ(2S) $R_{\rm AA}$ as a function of $p_{\rm T}$.

Table 6.7 lists the values of the ratio of $R_{\rm AA}$ of ψ(2S) over that of J/ψ as a function of $p_{\rm T}$.

Table 6.5: The values of $R_{\mathrm{AA}}^{\psi(2\mathrm{S})}/R_{\mathrm{AA}}^{\mathrm{J}/\psi}$ in different centrality bins in Pb-Pb collisions at $\sqrt{s_{\mathrm{NN}}} = 5.02$ TeV.

Centrality	$R_{\mathrm{AA}}^{\psi(2\mathrm{S})}/R_{\mathrm{AA}}^{\mathrm{J}/\psi}$
0-10%	0.417 ± 0.139 (stat 33.36%) ± 0.034 (syst 8.09%) + 0.059 (global 14.2%)
10-20%	0.590 ± 0.144 (stat 24.44%) ± 0.051 (syst 8.71%) + 0.084 (global 14.2%)
20-40%	0.314 ± 0.110 (stat 35.09%) ± 0.027 (syst 8.61%) + 0.045 (global 14.2%)
40-60%	0.459 ± 0.126 (stat 27.42%) ± 0.034 (syst 7.50%) + 0.065 (global 14.2%)
60-90%	0.596 ± 0.124 (stat 20.84%) ± 0.046 (syst 7.68%) + 0.085 (global 14.2%)

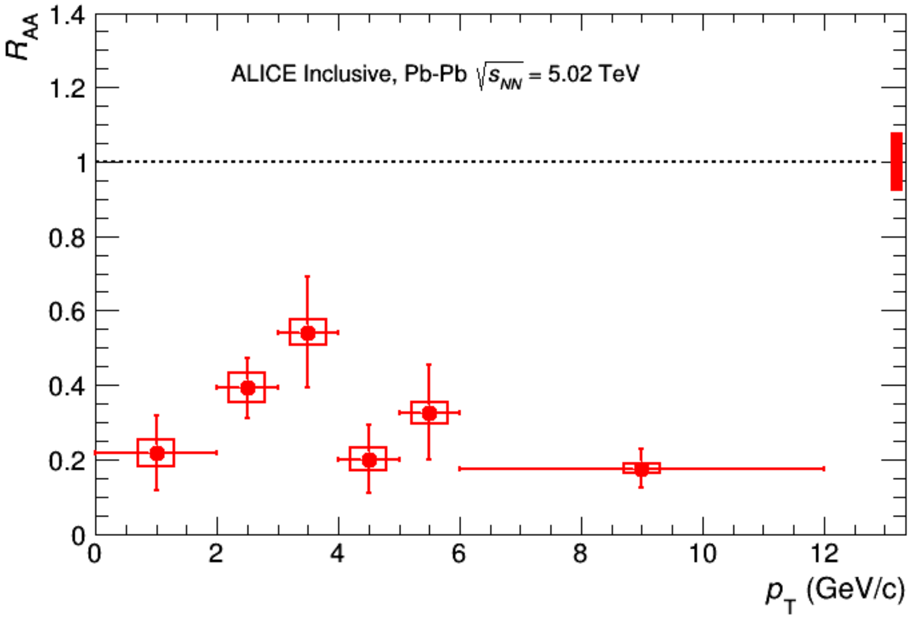

Figure 6.22: The inclusive ψ(2S) R_{AA} as a function p_{T} at $\sqrt{s_{\mathrm{NN}}} = 5.02$ TeV. The boxes centered at $R_{\mathrm{AA}} = 1$ represent the global uncertainties correlated over p_{T}.

Table 6.6: R_{AA} of ψ(2S) as a function of p_{T} in Pb-Pb collisions at $\sqrt{s_{\mathrm{NN}}} = 5.02$ TeV.

p_{T} GeV/c	$R_{\mathrm{AA}}^{\psi(2\mathrm{S})}$
0-2	0.217 ± 0.099 (stat 45.5%) ± 0.038 (syst 17.3%) + 0.017 (global 7.8%)
2-3	0.392 ± 0.080 (stat 20.5%) ± 0.039 (syst 10.0%) + 0.030 (global 7.8%)
3-4	0.541 ± 0.148 (stat 27.3%) ± 0.035 (syst 6.4%) + 0.042 (global 7.8%)
4-5	0.200 ± 0.091 (stat 45.4%) ± 0.031 (syst 15.4%) + 0.016 (global 7.8%)
5-6	0.326 ± 0.128 (stat 39.2%) ± 0.029 (syst 8.8%) + 0.025 (global 7.8%)
6-12	0.175 ± 0.052 (stat 30.0%) ± 0.012 (syst 7.1%) + 0.014 (global 7.8%)

Table 6.7: The values of $R_{\mathrm{AA}}^{\psi(2\mathrm{S})}/R_{\mathrm{AA}}^{\mathrm{J}/\psi}$ in different p_{T} bins in Pb-Pb collisions at $\sqrt{s_{\mathrm{NN}}} = 5.02$ TeV.

p_{T} GeV/c	$R_{\mathrm{AA}}^{\psi(2\mathrm{S})}/R_{\mathrm{AA}}^{\mathrm{J}/\psi}$
0-2	0.326 ± 0.138 (stat 42.40%) ± 0.091 (syst 27.95%) + 0.026 (global 7.9%)
2-4	0.700 ± 0.107 (stat 15.31%) ± 0.149 (syst 21.25%) + 0.055 (global 7.9%)
4-6	0.500 ± 0.160 (stat 31.96%) ± 0.130 (syst 25.96%) + 0.040 (global 7.9%)
6-12	0.531 ± 0.182 (stat 34.26%) ± 0.202 (syst 38.10%) + 0.042 (global 7.9%)

ψ(2S)/J/ψ yield ratio

The $\frac{\psi(2\mathrm{S})}{\mathrm{J}/\psi}$ is defined as:

$$\left[\frac{\psi(2\mathrm{S})}{\mathrm{J}/\psi}\right] = \frac{N_{\psi(2\mathrm{S})}}{N_{\mathrm{J}/\psi}} \times \frac{(A\times\varepsilon)_{\mathrm{J}/\psi}}{(A\times\varepsilon)_{\psi(2\mathrm{S})}} \tag{6.10}$$

As it is the ratio of invariant yields, the branching ratio of the dimuon decay channel does not enter the calculation and all the systematic uncertainties except the signal systematic and $A\times\varepsilon$ cancel out. The systematic uncertainties on the ratios were obtained by quadratically combining the systematic uncertainties entering in each element of Eq. (6.10). The ratio of the invariant yields of ψ(2S) to J/ψ integrated over centrality, p_{T} and y in Pb-Pb collisions at $\sqrt{s_{\mathrm{NN}}} = 5.02$ TeV is:

$$\left[\frac{\psi(2\mathrm{S})}{\mathrm{J}/\psi}\right] = 0.0088 \pm 0.0015 \text{ (stat 16.5\%)} \pm 0.0007 \text{ (syst 8.1\%)}$$

In Fig. 6.23, the $\left[\frac{\psi(2\mathrm{S})}{\mathrm{J}/\psi}\right]$ as a function centrality and p_{T} are shown.

Discussion

The R_{AA} of inclusive ψ(2S) as a function of centrality and transverse momentum at forward rapidity has been measured along with the $R_{\mathrm{AA}}(\psi(2\mathrm{S}))/R_{\mathrm{AA}}(\mathrm{J}/\psi)$ and yield ratio $\left[\frac{\psi(2\mathrm{S})}{\mathrm{J}/\psi}\right]$ as a function of centrality and p_{T}. The analysis has been carried out using the combined data of 2015 and 2018, which leads to improved precision

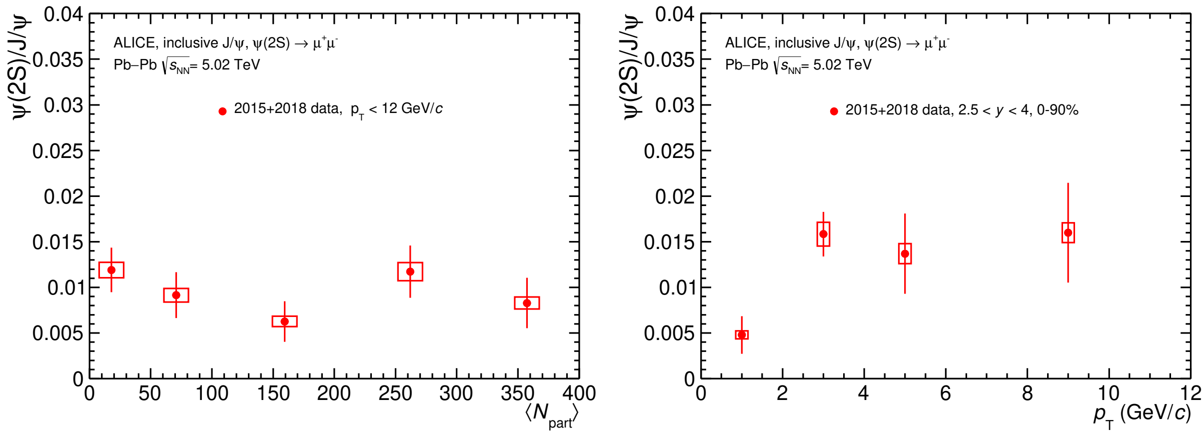

Figure 6.23: The inclusive ψ(2S) to J/ψ yield ratio as a function centrality (left) and $p_{\rm T}$ (right) at $\sqrt{s_{\rm NN}} = 5.02$ TeV.

in multiple kinematic variables.

Bibliography

[1] T. Matsui and H. Satz, Phys. Lett. **B178**, 416 (1986).

[2] F. Karsch and H. Satz, Z.Phys. **C51**, 209 (1991).

[3] T. Matsui, **LBL-24604**, 251 (1987).

[4] B. Svetitsky, Phys.Rev. **D37**, 2484 (1988).

[5] ALICE Collaboration, "Centrality determination in heavy ion collisions", ALICE-PUBLIC-2018-011. http://cds.cern.ch/record/2636623

[6] ALICE Collaboration, "J/ψ production in Pb-Pb collisions at $\sqrt{s_{\mathrm{NN}}} = 5.02$ TeV", Phys. Lett. B 766 (2017)

[7] ALICE Collaboration, "Differential study of inclusive J/ψ production at forward rapidity in Pb-Pb collisions at $\sqrt{s_{\mathrm{NN}}} = 5.02$ TeV", JHEP 02 (2020) 041

CHAPTER 7

Summary and Outlook

Summary

This chapter briefly summarizes the results presented in this thesis. The data, collected by the ALICE Muon spectrometer, in pp, p–Pb and Pb–Pb collisions have been analyzed and studied. The pp results have been used to normalize the p–Pb and Pb–Pb results. The results from p–Pb and Pb–Pb data presented in the thesis, help to extend our understanding of the cold and hot nuclear matter effects on the charmonia.

$\psi(2S)$ production in pp collisions

The results have been presented in two parts. Firstly, the cross section of $\psi(2S)$ production as a function of p_{T} and rapidity in pp collisions at 5.02 TeV have been reported. These results are crucial for understanding the QCD processes and production of the charmonia. The first measurement of p_{T} and y differential cross sections at 5.02 TeV, are shown. Secondly the production cross section ratio of $\psi(2S)$ and J/ψ, has been studied to explore the energy dependence. Comparing

with the published ALICE results at 7, 8 and 13 TeV, it is established that this ratio does not show any significant energy dependence.

The inclusive ψ(2S) production cross section, integrated over $0 < p_{\mathrm{T}} < 12$ GeV/c and for $2.5 < y < 4$, has been found to be $\sigma_{\psi(2S)} = 0.86 \pm 0.06$ (stat.) $\pm$ 0.10 (syst.) μb. The cross section of ψ(2S) is described well by the NRQCD calculations except for higher p_{T} bins. The NLO calculation based ICEM model, on the other hand overestimates the data at high p_{T}.

The ratio of inclusive ψ(2S)-to-J/ψ production cross sections integrated over p_{T} and y is found to be 0.15 ± 0.01 (stat.) ± 0.02 (syst.). The calculations based on NRQCD+CGC well reproduce the ratio as a function of p_{T} and y for $p_{\mathrm{T}} < 8$ GeV/c. The trend of the ψ(2S) over J/ψ cross-section ratio as a function of p_{T} and y is overestimated by the CEM model in the low p_{T} region.

ψ(2S) production in p–Pb collisions

The results on the inclusive ψ(2S) production at the forward (p-going direction, $2.03 < y_{cms} < 3.53$) and backward (Pb-going direction, $-4.46 < y_{cms} < -2.96$) rapidities in p–Pb collisions at 8.16 TeV, have been presented in chapter 5 of the thesis in the form of production cross sections, the double cross-section ratios with respect to the J/ψ in p–Pb and pp, and the nuclear modification factors R_{pPb}. The analysis has been segmented in two parts: 1) p_{T} and y differential cross-section measurement and 2) centrality dependence measurement.

The main conclusion which has been drawn from the above observables is that the initial state effects, which are sufficient to explain J/ψ suppression behavior, cannot describe the ψ(2S) suppression at the backward rapidity where it is found to be significantly suppressed. The final state effects are needed to describe ψ(2S) suppression.

Apart from that, no significant energy dependence or p_T dependence is observed in R_{pPb}.

J/ψ and ψ(2S) production in Pb–Pb collisions

The multi-differential J/ψ and single-differential ψ(2S) cross-section measurements are described in chapter 6.

The analysis of J/ψ in Pb–Pb collisions at 5.02 TeV at forward rapidity has been performed to investigate the recombination scenario in heavy-ion collisions. The high statistics of 2015+2018 datasets made it possible to precisely show the effect of recombination which are visible only at low p_T in the most central collisions. This effect induces a slope in the R_{AA} vs y plot in that particular bins, confirming the role of in-medium recombination of c$\bar{c}$ pairs.

In the next section, the measurement of R_{AA} of ψ(2S) as a function of p_T and centrality, has been presented. The ψ(2S) has been found to be more suppressed compared to J/ψ in semi-central and central collisions.

Outlook

ALICE is preparing for a major upgrade for Run 3 and Run 4 to operate in high luminosity beams.

The introduction of Muon Forward Tracker (MFT) will give the opportunity to study the prompt J/ψ production by separating the contribution to J/ψ cross-section coming from B decay. This has not been possible till date because of the presence of the absorber, which does not allow the displaced vertex analysis. It will be interesting to look at the J/ψ results in different collision systems in the upcoming days and estimate the B-meson production cross-sections at forward rapidities through J/ψ

tagging.

The charged particle multiplicity dependence of J/ψ cross-section in pp collisions, has gained a lot of attentions in the past due to the direct evidence of MultiPartonic Interactions (MPI). A similar study on ψ(2S) will shed light on the role of MPI in ψ(2S) production in pp collisions.

The search for deconfinement in small systems is currently a hot and most debated topic. A reasonable study of charmonium and in particular bottomonium suppression in small systems will require much higher statistics than the present pp data at 13 TeV. Such high statistics is likely to be possible during the high luminosity periods of Run 3 and 4. If such suppression is observed, then present understanding of QGP will be challenged.

The ψ(2S) production as a function of rapidity in p–Pb collisions at $\sqrt{s_{\rm NN}} = 8.16$ TeV exhibits a slope towards the forward rapidity in contrary to the model predictions and J/ψ observation of flat dependence. The large uncertainties however does not allow any firm conclusion. This regions should be explored in future with higher precision and in more rapidity bins. It may reveal some unknown features of the ψ(2S) production in p–Pb collisions.

The J/ψ flow coefficient v_2 measurement at 20-40% centrality in Pb–Pb collisions at $\sqrt{s_{\rm NN}} = 5.02$ TeV is still not explained by the theory. The installation of MFT will help to improve the results in the high $p_{\rm T}$ bins for prompt J/ψ. Not only v_2, but higher harmonics like v_3, v_4 will also be interesting observables the Run 3 and 4.

The measurement of ψ(2S) production is more challenging than that of J/ψ, because of a smaller production cross section and even larger suppression in PbPb, giving rise to a very low signal-to-background ratio. Therefore, we expect improvement in the uncertainties in ψ(2S) results in Run 3.

At present, all the states of upsilon(nS) cannot be resolved fully. Better mass reso-

lution of all the resonance states will ensure precision in the results.

We look forward towards Pb–Pb run at the highest achievable energy $\sqrt{s_{\rm NN}} = 5.5$ TeV. For all those interesting results from ALICE in the upcoming days, we need to wait till 2022.

Appendices

Name of the Student: Jhuma Ghosh
Name of the CI/OCC: Saha Institute of Nuclear Physics **Enrolment No.:** PHYS05201504005
Thesis Title: Charmonium studies at forward rapidity with ALICE Muon Spectrometer at the LHC
Discipline: Physical Science **Sub-Area of Discipline:** High Energy Experimental Particle Physics
Date of viva voce: 15/03/2021

The cross section of ψ(2S) production as a function of $p_{\rm t}$ and rapidity in pp collisions at 5.02 TeV have been reported in the thesis. These results are crucial for understanding the QCD processes and production of the charmonia. The first measurement of $p_{\rm t}$ and y differential cross sections at 5.02 TeV, are also shown. The production cross section ratio of ψ(2S) and J/ψ, has been studied to explore the energy dependence. Comparing with the published ALICE results at 7, 8 and 13 TeV, it is established that this ratio does not show any significant energy dependence. The cross section of ψ(2S) is described well by the NRQCD calculations except for higher $p_{\rm t}$ bins. The NLO calculation based ICEM model, on the other hand overestimates the data at high $p_{\rm t}$. The ratio of inclusive ψ(2S)-to-J/ψ production cross sections integrated over $p_{\rm t}$ and y is found to be 0.15 ± 0.01 (stat.) ± 0.02 (syst.). The calculations based on NRQCD+CGC well reproduce the ratio as a function of $p_{\rm t}$ and y for < 8 GeV/c. The trend of the over cross-section ratio as a function of $p_{\rm t}$ and y is overestimated by the CEM model in the low $p_{\rm t}$ region.

The results on the inclusive production at the forward (p-going direction, $2.03 < y_{cms} < 3.53$) and backward (Pb-going direction, $-4.46 < y_{cms} < -2.96$) rapidities in p–Pb collisions at 8.16 TeV, have been presented in the thesis in the form of production cross sections, the double cross-section ratios with respect to the J/ψ in p–Pb and pp, and the nuclear modification factors $R_{\rm pPb}$. The analysis has been segmented in two parts: 1) $p_{\rm t}$ and y differential cross-section measurement and 2) centrality dependence measurement. The main conclusion which has been drawn from the above observable is that the initial state effects, which are sufficient to explain suppression behavior, but cannot describe the suppression at the backward rapidity where it is found to be significantly suppressed. The final state effects are needed to describe ψ(2S) suppression. Apart from that, no significant energy dependence or $p_{\rm t}$ dependence is observed in $R_{\rm pPb}$. The multi-differential and single-differential ψ(2S) cross-section measurements are described in the thesis. The analysis of J/ψ in Pb–Pb collisions at 5.02 TeV at forward rapidity has been performed to investigate the recombination scenario in heavy-ion collisions. The high statistics of 2015+2018 datasets made it possible to precisely show the effect of recombination which are visible only at low $p_{\rm t}$ in the most central collisions. This effect induces a slope in the $R_{\rm AA}$ vs y plot in that particular bins, confirming the role of in-medium recombination of $c\bar{c}$ pairs.

The measurement of $R_{\rm AA}$ of ψ(2S) as a function of $p_{\rm t}$ and centrality, has been presented. The ψ(2S) has been found to be more suppressed compared to J/ψ in semi-central and central collisions. It also shows a decreasing trend with increase of $p_{\rm t}$.